

# High Energy Resummation and Electroweak Corrections in Dijet Production at Hadronic Colliders



*Jack J. Medley*

A thesis submitted in fulfilment of the requirements  
for the degree of Doctor of Philosophy  
to the  
University of Edinburgh

March 2016

# Lay Summary

At experiments like the Large Hadron Collider (LHC) we seek to explore new areas of particle physics by accelerating hadrons (such as protons) into one another. Because hadrons are comprised of more fundamental particles, namely; quarks, anti-quarks and gluons, what we see after these collisions is the result of two (or more) of these particles scattering off each other. We use a Relativistic Quantum Field Theory called Quantum Chromodynamics (QCD) to describe these encounters. When using QCD to investigate an interaction between any two of these fundamental particles we quickly find that there are an infinite number of possible ways in which the collision could have happened (each possible way being symbolised by a Feynman Diagram); since we cannot hope to calculate all of these we must chose the most important subset of this infinity and calculate those.

Traditional approaches focussed on selection the subset with the fewest factors of the strong coupling constant, known as  $\alpha_s$ , because  $\alpha_s$  is small and therefore any diagrams with extra factors will contribute less to the overall sum. Here we use a more subtle technique known broadly as ‘resummation’. In this approach we focus not only on the number of  $\alpha_s$  factors present but also the number of ‘large logarithms’ at play. In this way we find a different subset of this infinity of diagrams which we consider to be the most important and instead focus on calculating those.

Here we present a new calculation for the final state where we have a  $Z^0$  boson or a high energy photon,  $\gamma^*$ , decaying to an electron-positron pair in association with at least two high energy QCD fundamental particles (which we observes experimentally as ‘jets’). Our resummation captures the ‘leading’ (i.e. the largest) logarithms in this process and is further improved by matching our result to the ‘Leading Order’ result (the result obtained by the aforementioned traditional techniques).

We present comparisons of our new theoretical prediction to data gathered at the ATLAS and CMS experiments at the LHC and see that it gives good agreement across a wide range of observables. Further we also present two new experimental

---

studies. Firstly, we show a comparison of our prediction matched to an extra ‘parton shower’ resummation to an ATLAS study of QCD radiation patterns. We see that our description agrees well with the data throughout. Secondly, we present a study of  $Z/\gamma^*$  plus dijets at 100 TeV (a collision energy roughly ten times higher than that used at the LHC). We compare the behaviour of the high energy logarithmic enhancements at 7 TeV and 100 TeV and see that at any high energy hadronic Future Circular Collider (FCC) the effects described by our resummation become significantly more important.

# Abstract

QCD final states are ubiquitous at hadron colliders such as the Large Hadron Collider (LHC). Therefore understanding high energy perturbative quantum chromodynamics at these experiments is essential not only as a test of the Standard Model, but also because many of the dominant background to many new physics searches is QCD in nature. One such ‘standard candle’ is the production of a dilepton pair in association with dijets. Here we present a new description of this final state (through  $Z^0$  boson and virtual photon). This calculation adds to the fixed-order accuracy the dominant logarithms in the limit of large partonic centre-of-mass energy to all orders in the strong coupling  $\alpha_s$ . This is achieved within the framework of High Energy Jets.

This calculation is made possible by extending the high energy treatment to take into account the multiple  $t$ -channel exchanges arising from  $Z$  and  $\gamma^*$ -emissions off several quark lines. The correct description of the interference effects from the various  $t$ -channel exchanges requires an extension of the subtraction terms in the all-order calculation. We describe this construction and compare the resulting predictions to a number of recent analyses of LHC data. The description of a wide range of observables is good, and, as expected, stands out from other approaches in particular in the regions of large dijet invariant mass and large dijet rapidity spans.

In addition we also present two new experimental studies. Firstly, we show a comparison of High Energy Jets matched to the **ARIADNE** parton shower to an ATLAS study of gap activity in dijet events, this is also compared to several other state-of-the-art next-to-leading order (in  $\alpha_s$ ) Monte Carlo generators matched with both with **PYTHIA** and **HERWIG** parton shower codes. We see that our description agrees well with the data throughout. Secondly, we present a study of  $Z/\gamma^*$  plus dijets at 100 TeV. We compare the behaviour of the high energy logarithmic enhancements to the QCD perturbative series at 7 TeV and 100 TeV and see that at any high energy hadronic Future Circular Collider (FCC) the effects described by our resummation become significantly more important.



# Declaration

Except where otherwise stated, the research undertaken in this thesis was the unaided work of the author. Where the work was done in collaboration with others, a significant contribution was made by the author.

In particular the work and results in chapter 4 was done in collaboration and appears in the following publication:

[51] J. Andersen, J. Medley, J. Smillie,  $Z/\gamma^*$  plus Multiple Hard Jets in High Energy Collisions [arXiv:1603.05460]

*J. Medley*

March 2016



# Acknowledgements

Cheers guys!



# Contents

<b>Abstract</b>	i
<b>Declaration</b>	iv
<b>Acknowledgements</b>	vi
<b>Contents</b>	viii
<b>List of figures</b>	xii
<b>List of tables</b>	xvii
<b>1 Introduction</b>	1
1.1 A Little History . . . . .	1
1.2 Thesis Outline . . . . .	2
<b>2 Quantum Chromodynamics at Hadronic Colliders</b>	5
2.1 The QCD Lagrangian . . . . .	5
2.2 The Partonic Cross-Section . . . . .	7
2.3 Divergences and Regularisation . . . . .	12
2.3.1 Ultraviolet divergences . . . . .	12
2.3.2 Infrared and collinear divergences . . . . .	13
2.3.3 Regularising divergences . . . . .	14
2.4 The QCD Beta Function . . . . .	16
2.5 QCD Factorisation at Hadronic Colliders . . . . .	18
2.6 From Partons to Jets . . . . .	19
2.7 Perturbative QCD and Resummation . . . . .	21
2.7.1 Fixed-order Perturbation . . . . .	21
2.7.2 An Example Fixed-Order Calculation . . . . .	22
2.7.3 Resumming Higher-Order Corrections . . . . .	34
2.8 Spinor-Helicity Notation . . . . .	36
2.8.1 Spinor-Helicity Calculations with Massive Partons . . . . .	40
2.9 Monte Carlo Techniques . . . . .	44
2.9.1 One Dimensional Integration . . . . .	44
2.9.2 Higher Dimensional Integration . . . . .	46
2.9.3 Variation Reduction Techniques . . . . .	47

<b>3 High Energy QCD</b>	<b>53</b>
3.1 The ‘High Energy’ limit . . . . .	53
3.2 Mandelstam Variables in the High Energy Limit . . . . .	54
3.3 $qQ$ -scattering at High Energy (at LO) . . . . .	55
3.4 $qg$ scattering at High Energy . . . . .	57
3.4.1 $s$ -channel . . . . .	58
3.4.2 $t$ -channel . . . . .	60
3.4.3 $u$ -channel . . . . .	60
3.5 $qQ$ -scattering at High Energy (at NLO) . . . . .	62
3.6 $t$ -channel Dominance . . . . .	65
3.7 Effective Vertices For Real Emissions . . . . .	67
3.8 Virtual Corrections To All Orders . . . . .	71
3.9 High Energy Jets . . . . .	72
3.9.1 The High Energy Jets Framework . . . . .	72
3.9.2 Factorisation Into Currents . . . . .	73
3.9.3 The High Energy Jets Monte Carlo . . . . .	74
3.9.4 Matching to HEJ+ARIADNE . . . . .	76
3.9.5 Comparisons to data . . . . .	77
<b>4 <math>Z/\gamma^*+Jets</math> at the LHC</b>	<b>79</b>
4.1 Introducing $Z/\gamma^*+Jets$ at the LHC . . . . .	79
4.2 Constructing $Z/\gamma^*+jets$ . . . . .	81
4.2.1 A Current for $Z^0+Jets$ . . . . .	81
4.2.2 $Z^0$ Emission Interference . . . . .	84
4.2.3 Photonic Interference . . . . .	85
4.2.4 The $2 \rightarrow n$ Matrix Element . . . . .	88
4.3 Regularising the $Z/\gamma^*+Jets$ Matrix Element . . . . .	89
4.3.1 Real Soft Emissions . . . . .	89
4.3.2 Virtual Emissions . . . . .	93
4.3.3 Cancellation of Infrared Divergences . . . . .	94
4.3.4 Example: $2 \rightarrow 3$ Scattering . . . . .	97
4.4 Subtractions and the $\lambda_{cut}$ scale . . . . .	100
4.5 The Differential $Z/\gamma$ Cross-Section . . . . .	101
4.6 $Z/\gamma^*+Jets$ : Computational Aspects . . . . .	105
4.7 $Z/\gamma^*+Jets$ at the LHC . . . . .	106
4.7.1 $Z/\gamma^*+Jets$ at the ATLAS Experiment . . . . .	106
4.7.2 $Z/\gamma^*+Jets$ at the CMS Experiment . . . . .	110
4.8 Conclusions . . . . .	111
<b>5 Dijets and Gap Jets at ATLAS</b>	<b>115</b>
<b>6 <math>Z/\gamma^*+Jets</math> at 100TeV</b>	<b>123</b>
<b>7 Conclusions and Outlook</b>	<b>133</b>
<b>Bibliography</b>	<b>134</b>

**Publications**

**138**

*CONTENTS*

---

# List of Figures

2.1	The evolution of $\alpha_s$ over several orders of magnitude in the scale of the process $Q^2$ . The data points fitted are of varying degrees of formal accuracy ranging from next-to-leading order in $\alpha_s$ (NLO) to next-to-next-to-next-to-leading order in $\alpha_s$ ( $N^3LO$ ). Fig. from [23]. . . . .	18
2.2	Simulations of the average number of jets as a function of the sum of the transverse momenta in the event, $H_T$ , for inclusive dijets at a 7TeV LHC. . . . .	23
2.3	Feynman diagrams for calculating the $O(\alpha_s)$ correction to $\gamma^* \rightarrow q\bar{q}$ . Fig. (2.3a) is the leading order contribution. Figs. (2.3b) - 2.3d are the virtual corrections and lastly figs. (2.3e) - (2.3f) are the real emission contributions. . . . .	24
2.4	The ratio of the inclusive Higgs plus three jet cross-section to inclusive Higgs plus two jet cross-section shown for centre-of-mass energies of 14TeV (similar to the current LHC), 33TeV and 100TeV (possible energy scales for a hadronic future circular collider). . . . .	37
2.5	The probability of a third jet emission in $W^\pm$ plus inclusive dijets as a function of the rapidity gap between the two leading jets in rapidity at the D $\emptyset$ experiment at the Tevatron experiment. The data are compared to a number of generators including the leading logarithmic accurate HEJ and the NLO accurate <b>Blackhat+Sherpa</b> . . . . .	38
2.6	A simple importance sampling example (see equation (2.130)). The integrand, $f(x)$ , is shown in blue, the importance sampling distribution is shown in green and, for comparison, the uniform probability density function used in the naïve case of no importance sampling is also shown (in red). . . . .	49
2.7	The absolute value squared of the $Z^0$ propagator for a range of values of the invariant mass squared of the $Z^0$ , $p_Z^2$ . We see that, as expected, it is strongly peaked at the $Z^0$ mass and, as such, is an ideal candidate for using importance sampling. . . . .	51
2.8	Recent parton distribution function fits from the HERA experiment. The observed variation in $f(x_{a/b}, Q^2)$ , especially at high $x_{a/b}$ , can be used to reduce the variance of a Monte Carlo approach to computing eqn (2.42) by using an importance sampling approach . . . . .	51
3.1	The only diagram which contributes to $qQ \rightarrow qQ$ at leading order in $\alpha_s$ . . . . .	57

3.2	The $s$ , $t$ and $u$ channel diagrams contributing to $q^-g^+ \rightarrow q^-g^+$ at leading order in $\alpha_s$ in figures (3.2a), (3.2b) and (3.2c) respectively. . . . .	58
3.3	The leading logarithmic contributions to $qg \rightarrow qg$ at NLO. The uncrossed diagram, $\mathcal{M}_{qQ \rightarrow qQ}^{\text{NLO},II}$ , shown in (a) exchanges two gluons in the $t$ channel and the crossed diagram, $\mathcal{M}_{qQ \rightarrow qQ}^{\text{NLO},X}$ , case (b) exchanges two gluons in the $u$ channel and is related to (a) (up to a colour factor) via a crossing symmetry . . . . .	63
3.4	Three processes contributing to exclusive quad-jet production. (a) has the maximum number of gluons exchanged in the $t$ -channel (three) and will dominate in the High Energy limit, (b) and (c) only have two and one gluon which can reggeise. As such as we move from left to right we will lose powers of large logarithms but maintain the same power of $\alpha_s$ and therefore we can reasonably approximate quad-jet production by neglecting (b) and (c). . . . .	66
3.5	The limiting behaviour of $qg \rightarrow qg$ in the regions of phase space where either $y_g \gg y_q$ or $y_q \gg y_g$ . The intermediate diagrams indicate the flow of colour through the process. . . . .	67
3.6	The 5 possible emission sites of extra QCD radiation in $qQ \rightarrow qQ$ . Fig. from [15]. . . . .	68
4.1	The possible emission sites for a neutral weak boson. . . . .	81
4.2	$\overline{ \mathcal{M}_{qg \rightarrow Zqg}^t ^2}$ shown for a slice through the final state phase-space defined by eqn. (4.5). We compare to the leading order result obtained from <b>MadGraph</b> . . . . .	83
4.3	The matrix-element squared divided by the square of the partonic centre-of-mass energy for $qQ \rightarrow ZqQ$ with the $Z$ decaying to an electron-positron pair for the phase space slice described in eqn. (4.5). Increasing values of $\Delta$ represent increasing rapidity separation between the jets. The different lines show the contributions from different terms in the calculation: only emission from the forward or the backward quark line (black, dashed and green, dotted), their sum without the interference term (magenta, dotted) and their sum including interference (red, solid) which is seen to agree exactly with the LO result (blue, thick solid). . . . .	86
4.4	The matrix-element squared divided by the square of the partonic centre-of-mass energy for $qQ \rightarrow Z/\gamma^* qQ$ with the $Z/\gamma^*$ decaying to an electron-positron pair. The $\mathcal{O}(\alpha_s^2 \alpha_W)$ tree-level contribution as described in HEJ (red, dashed) exactly matches that of <b>MadGraph5</b> (blue, solid). The terms corresponding to the production of a $Z$ boson only (green, dotted) significantly undershoots the full result. The virtual photon terms are, therefore, clearly an important contribution to the matrix element away from the $Z$ Breit-Wigner peak. . . . .	87

---

4.5 Examples of both real and virtual diagrams contributing to $2 \rightarrow 3$ scattering. In fig. (4.5a) the $p_2$ has been drawn with a dashed line to denote it is not resolvable. In fig. (4.5b) the final state momenta have been labelled in a seemingly strange way - this was done to make clear the cancellation when working through the algebra. . . . .	98
4.6 The effect of varying $\lambda_{cut}$ on the differential distribution in the rapidity gap between the two leading jets in $p_\perp$ , $\Delta y_{j1,j2}$ , with the $N_{jet} = 2, 3, 4$ exclusive selections shown from left to right. $\lambda_{cut} = 0.2$ (red), 0.5 (blue), 1.0 (green), 2.0 (purple). The bands represent the scale variation described in the text. . . . .	102
4.7 The effect of varying $\lambda_{cut}$ on the differential distribution in the rapidity gap between the two extremal jets in rapidity, $\Delta y_{jf,jb}$ , with the $N_{jet} = 2, 3, 4$ exclusive selections shown from left to right. $\lambda_{cut} = 0.2$ (red), 0.5 (blue), 1.0 (green), 2.0 (purple). The bands represent the scale variation described in the text. . . . .	103
4.8 These plots show the inclusive jet rates from (a) HEJ and (b) other theory descriptions and data [1]. HEJ events all contain at least two jets and do not contain matching for 5 jets and above, so these bins are not shown. . . . .	109
4.9 These plots show the invariant mass between the leading and second-leading jet in $p_T$ . As in Fig. (4.8), predictions are shown from (a) HEJ and (b) other theory descriptions and data [1]. These studies will inform Higgs plus dijets analyses, where cuts are usually applied to select events with large $m_{12}$ . . . . .	109
4.14 The transverse momentum distribution of the third hardest jet in inclusive dijet events in [52], compared to (a) the predictions from HEJ and (b) the predictions from other theory descriptions. . . . .	111
4.10 The comparison of (a) HEJ and (b) other theoretical descriptions and data [1] to the distribution of the absolute rapidity difference between the two leading jets. HEJ and Blackhat+Sherpa give the best description. . . . .	112
4.11 These plots show the differential cross section in the ratio of the leading and second leading jet in $p_T$ from (a) HEJ and (b) other theory descriptions and data [1]. . . . .	112
4.12 The inclusive jet rates as given by (a) the HEJ description and (b) by other theoretical descriptions, both plots compared to the CMS data in [52]. . . . .	113
4.13 The transverse momentum distribution of the second hardest jet in inclusive dijet events in [52], compared to (a) the predictions from HEJ and (b) the predictions from other theory descriptions. . . . .	113
5.1 The gap fraction, $f(Q_0)$ , as a function of (a) the rapidity gap, $\Delta y$ , and (b) the average $p_T$ , $\bar{p}_T$ , of the dijet system. . . . .	118
5.2 The average number of jets, $\langle N_{\text{jets}} \text{ in the rapidity interval} \rangle$ , in the rapidity gap bounded by the dijet system, as a function of (a) the rapidity gap, $\Delta y$ , and (b) the average $p_T$ , $\bar{p}_T$ , of the dijet system. . . . .	119

5.3	The first azimuthal angular moment, $\langle \cos(\pi - \Delta\phi) \rangle$ , as a function of (a) the rapidity gap, $\Delta y$ and (b) the average $p_T$ , $\bar{p}_T$ , of the dijet system. . . . .	120
5.4	The ratio of the second azimuthal angular moment, $\langle \cos(2\Delta\phi) \rangle$ , to the first azimuthal angular moment, $\langle \cos(\pi - \Delta\phi) \rangle$ , as a function of (a) the rapidity gap, $\Delta y$ , and (b) the average $p_T$ , $\bar{p}_T$ , of the dijet system. . . . .	121
5.5	The first azimuthal angular moment, $\langle \cos(\pi - \Delta\phi) \rangle$ , for events passing the veto on gap activity above $Q_0 = 20\text{GeV}$ as a function of (a) the rapidity gap, $\Delta y$ , and (b) the average $p_T$ , $\bar{p}_T$ , of the dijet system. . . . .	121
5.6	The ratio of the second azimuthal angular moment, $\langle \cos(2\Delta\phi) \rangle$ , to the first azimuthal angular moment, $\langle \cos(\pi - \Delta\phi) \rangle$ , as a function of (a) the rapidity gap, $\Delta y$ , and (b) the average $p_T$ , $\bar{p}_T$ , of the dijet system. A veto of $Q_0 = 20\text{GeV}$ , for (a), and $Q_0 = 30\text{GeV}$ , for (b), is applied on activity in the rapidity gap is applied. . . . .	122
6.1	The differential cross-section for $Z/\gamma^*$ plus inclusive dijets as a function of the azimuthal separation of the dijet system shown for centre-of-mass energies of 7TeV (blue) and 100TeV (pink). . . . .	125
6.2	The cross-section for $Z/\gamma^*$ plus inclusive dijets as a function of the number of jets, $N_{\text{jet}}$ , shown for centre-of-mass energies of 7TeV (blue) and 100TeV (pink). . . . .	126
6.3	The differential cross-section for $Z/\gamma^*$ plus inclusive dijets as a function of the absolute value of the rapidity gap between the dijets, $\Delta y^{j1,j2}$ shown for centre-of-mass energies of 7TeV (blue) and 100TeV (pink). . . . .	128
6.4	The differential cross-section for $Z/\gamma^*$ plus inclusive dijets as a function of the invariant mass of the dijets, $m^{jj}$ , shown for centre-of-mass energies of 7TeV (blue) and 100TeV (pink). . . . .	129
6.5	The differential cross-section for $Z/\gamma^*$ plus inclusive dijets as a function of the transverse momentum of the first, second and third leading jets in $p_T$ shown in fig. (6.5a), (6.5b) and (6.5c) respectively and for centre-of-mass energies of 7TeV (blue) and 100TeV (pink). . . . .	130
6.6	The differential cross-section for $Z/\gamma^*$ plus inclusive dijets as a function of the absolute value of the rapidity of the first, second and third leading jets in rapidity shown in fig. (6.6a), (6.6b) and (6.6c) respectively and for centre-of-mass energies of 7TeV (blue) and 100TeV (pink). . . . .	131

# List of Tables

1.1	The fermion content of the standard model. . . . .	2
2.1	A graphical summary of the Feynman rules. The solid lines indicate a fermion (anti-fermion) propagator with momentum flowing parallel (anti-parallel) to the direction of the arrow. Similarly for the dashed lines which represent the ghost (anti-ghost) propagating and lastly the twisted lines depict a propagating gluon. As in the preceding equations $i$ and $j$ represent fundamental colour indices, $a$ and $b$ represent adjoint colour indices and, where present, $f$ and $f'$ represent fermion flavour. All Greek indices are Lorentz indices. . . . .	10
2.2	The Monte-Carlo approximation to equation (2.130) as we vary the number of sampled points, $N$ , shown in the naïve sampling case and in the importance sampled case. . . . .	48
3.1	Some examples of $2 \rightarrow 2$ leading order matrix elements which contribute to the two jet exclusive cross-section. . . . .	68
4.1	The FKL-only cross sections for the 2-, 3- and 4-jet exclusive rates with associated statistical errors shown for different values of the regularisation parameter $\lambda_{cut}$ . The scale choice was half the sum over all transverse scales in the event, $H_T/2$ . . . . .	100
4.2	Cuts applied to theory simulations in the ATLAS $Z$ -plus-jets analysis results shown in Figs. (4.8)–(4.11). . . . .	106
4.3	Cuts applied to theory simulations in the CMS $Z$ -plus-jets analysis results shown in Figs. (4.12)–(4.14) . . . . .	110
5.1	Cuts applied to theory simulations in the ATLAS dijets analyses. $Q_0$ is the gap jet veto scale. The results are shown in figs. (5.1)–(5.6). . . . .	115
6.1	Cuts applied to theory simulations for the 100 TeV $Z$ -plus-jets analysis results shown in Figs. (6.1)–(6.6c). . . . .	124

# Chapter 1

## Introduction

### 1.1 A Little History

The Standard Model is a gauge quantum field theory describing three of the four observed fundamental forces - with the inclusion of gravity remaining elusive. Its local gauge structure is given by:

$$SU(3)_c \times SU(2)_L \times U(1)_Y. \quad (1.1)$$

The subscripts on the groups are simply a convenient notation. The ‘c’ on  $SU(3)$  indicates that it is the strong ‘colour’ coupling being described. The ‘L’ on  $SU(2)$  indicates that all right-handed states are in the trivial representation of the group and the ‘Y’ on the  $U(1)$  indicates that this is the hypercharge group and not the electromagnetic group. The  $SU(3)_c$  group describes the strong nuclear force (Quantum Chromodynamics or QCD) and its 8 gauge generators give us the massless spin-1 gluons,  $G_a^\mu(x)$ ,  $a = 1, \dots, 8$ , present in the standard model. There are three weak boson states,  $W_a^\mu(s)$ ,  $a = 1, \dots, 3$ , associated with the  $SU(2)_L$  group and a further one,  $B^\mu(x)$ , which comes from the  $U(1)_Y$  group.

The only remaining boson to complete the standard model arises from the complex scalar Higgs field whose ground state is not invariant under the action of  $SU(2)_L \times U(1)_Y$ . This field breaks the standard model gauge symmetry to

$$SU(3)_c \times U(1)_{em}, \quad (1.2)$$

where the  $U(1)_{em}$  refers to the electromagnetic charge. After this ‘Spontaneous Symmetry Breaking’ occurs three of the four aforementioned bosons,  $W_a^\mu(s)$  and  $B^\mu(x)$  acquire mass and combinations of them are physically realised as the experimentally observer electroweak boson; The massive states  $W^\pm, Z^0$  and the massless photon,  $\gamma$ . The photon and the  $Z^0$  bosons are of particular importance in the work that follows.

The fundamental particle content of the Standard Model also includes fermions. These are spin-1/2 particles which obey the spin-statistics theorem (and hence the Pauli exclusion principle) and comprise, along with the gluons which binds the nucleus together, all known visible matter in the universe. The fermions are structured in three so-called ‘generations’, shown in tab. 1.1 and can be further subdivided into quarks and leptons. Quarks are colour triplets under QCD but are also charged under the electroweak group. The up ( $u$ ), charm ( $c$ ) and top ( $t$ ) quarks have electric charge  $+\frac{2}{3}$  while the down ( $d$ ), strange ( $s$ ) and bottom ( $b$ ) quarks have  $-\frac{1}{3}$ . Leptons are singlets under  $SU(3)$  and so do not couple to the strong sector. The charged leptons  $e, \mu$  and  $\tau$  have electric charge  $-1$  and the neutrinos are neutral.

	First Generation	Second Generation	Third Generation
Quarks	$u, d$	$c, s$	$t,$
Leptons	$e, \nu_e$	$\mu, \nu_\mu$	$\tau, \nu_\tau$

Table 1.1: The fermion content of the standard model.

## 1.2 Thesis Outline

The aim of this thesis is to detail the importance of a certain class of perurbatively higher-order terms in events with QCD radiation in the final state. In particular we will consider corrections to parton-parton collisions with a  $Z^0$  or  $\gamma$  in association with high energy QCD radiation in the final state.

In chapter 2 I will begin by introducing quantum chromodynamics, the theory of the strong sector in the standard model, and detail how we might use this to calculate physical observables (such as cross-sections and differential distributions) at hadron colliders such as the Large Hadron Collider. I will discuss how these observables fall prey to divergences in QCD-like quantum field theories with massless states and mention briefly how such divergences can be handled. I will then describe how the computationally expensive integrals derived in subsequent chapters may be efficiently evaluated using Monte-Carlo techniques.

In chapter 3 the details of QCD in the ‘High Energy’ limit are discussed. After

completing a few instructive calculations we will see how, in this limit, the traditional fixed-order perturbation theory view of calculating cross-sections fades as another subset of terms, namely the ‘Leading Logarithmic’ terms in  $\frac{s}{t}$ , become more important. I will discuss previous work in the High Energy limit of QCD and how this can be used to factorise complex parton-parton scattering amplitudes into combinations of ‘currents’ which, when combined with gauge-invariant effective gluon emission terms can be used to construct approximate high-multiplicity matrix elements.

In chapter 4 the work of the previous chapter is extended to the case where there is a massive  $Z^0$  boson or an off-shell photon,  $\gamma^*$ , in the final state. A ‘current’ for this process is derived and the complexities arising from two separate sources of interference are explored. This new result for the matrix element is compared to the results obtained from a Leading Order (in the strong coupling,  $\alpha_s$ ) generator **MadGraph** at the level of the matrix element squared in wide regions of phase space is seen to be in exact agreement. This result must then be regularised to treat the divergences discussed in chapter 2 and this process is presented. The procedure for matching this regularised result to Leading Order results is shown and the importance of the inclusion of these non-resummation terms is discussed. Lastly three comparisons of the High Energy Jets Z+Jets Monte-Carlo generator to recent experimental studies **ATLAS** and **CMS** at the LHC are shown.

From here we use the results of chapter 4, and the resulting publicly available Monte Carlo package, to compare our description to a recent experimental prediction of the ratio of the  $W^\pm + \text{jets}$  rate to the  $Z/\gamma^* + \text{jets}$  rate. Our predictions are compared against next-to-leading order (in  $\alpha_s$ ) results from **NJet** and leading order results from **MadGraph**.

In chapter ?? we apply the massive spinor-helicity to the production of a  $t\bar{t}$  pair in hadronic collisions. Using the **PySpinor** package we calculate values for the full-mass matrix element and compare them to leading-order (in  $\alpha_s$ ) results from **MadGraph**. This is a process in which the leading logarithmic contribution starts at one order higher than in previous work and so the effects of the resummation are not as expected to be as crucial as in the case of chapter 4 - however at large values for the centre-of-mass energy (such as that a future high energy circular collider) these ‘next-to-leading’ logarithms will once again lead to the breakdown of fixed-order perturbation theory.

In chapter 5 we discuss the results of a lengthy study of jet production from the **ATLAS** collaboration. This analysis was a thorough look at BFKL-like dynamics in proton-proton colliders and the HEJ predictions are seen to describe the data well in the regions of phase-space where we know the effects of our resummation become relevant. We compare the predictions from both standalone HEJ and HEJ interfaced with **ARIADNE**, a parton shower based on a dipole-cascade model. Although the interface to

ARIADNE increases the computational complexity significantly; we see that the Sudakov logarithms added by significantly improve the description of data.

In chapter 6, with a study of  $Z/\gamma^* + \text{Jets}$  at a centre-of-mass energy of 100TeV relevant for the discussion of the next wave of high energy particle physics experiments (such as any Future Circular Collider) which are of great interest to the community at large. We see that the higher-order perturbative terms are much larger at 100TeV relative to 7TeV data and predictions. Moreover, the regions of phase-space relevant for this thesis; that of high energy wide-angle QCD radiation is especially enhanced and, therefore resumming these contributions will be essential for precision physics at any ‘Future Circular Collider’.

Finally, in chapter 7 I summarise the results of the above chapters and provide a short outlook for future work.

## Chapter 2

# Quantum Chromodynamics at Hadronic Colliders

### 2.1 The QCD Lagrangian

We obtain the QCD Lagrangian by considering the spin- $\frac{1}{2}$  Dirac Lagrangian for the case of a fermionic fields  $\psi$  each with mass  $m$ :

$$\mathcal{L}_D = \bar{\psi}_i (i\cancel{D} - m)_{ij} \psi_j, \quad (2.1)$$

where  $\psi_i$  is itself a vector of 3 fermion fields in the fundamental representation of  $SU(3)$  with  $i = 1, \dots, 3^1$ . This is manifestly invariant under the *global*  $SU(3)$  transformation

$$\psi_i \rightarrow e^{i\alpha^a T_{ij}^a} \psi_j \quad (2.2)$$

where  $a = 1, \dots, 8$ ,  $\alpha^a$  are constant and  $T^a$  are the generators of the  $SU(3)$  group. We choose to promote this *global* symmetry to a *local* one by relaxing the constraint that  $\alpha^a$  are constant and instead allow them to depend on a space-time coordinate i.e.

$$\alpha^a = \alpha^a(x^\mu). \quad (2.3)$$

---

<sup>1</sup>The choice of 3 here is, again, well experimentally verified. Here we will work explicitly with the gauge group  $SU(3)$  although many of the results which follow can be derived with a more general special unitary group  $SU(N_c)$ .

This breaks the  $SU(3)$  symmetry but we can recover the required invariance by replacing the usual partial derivative term with a ‘covariant derivative’ defined by:

$$\mathcal{D}_{ij}^\mu = \partial_{ij}^\mu - ig_s A^{\mu a} T_{ij}^a, \quad (2.4)$$

where  $g_s$  is the QCD coupling constant and  $A_\mu^a$  is the QCD gauge field associated with the gluon. With this replacement the local  $SU(3)$  invariance of eqn. (2.1) is recovered. We must also include the effect of the kinetic term for the gluon field in our theory. We do this by considering the field-strength tensor for  $A_\mu^a$ ,  $F_{\mu\nu}^a$  which is given by:

$$F_{\mu\nu}^a = \partial_\mu A_\nu^a - \partial_\nu A_\mu^a + g_s f^{abc} A_\mu^b A_\nu^c \quad (2.5)$$

where  $f^{abc}$  are constants which define the algebra of the  $SU(3)$  group and are given by

$$T^a T^b - T^b T^a = i f^{abc} T^c. \quad (2.6)$$

eqn. (2.6) is what makes QCD fundamentally different from Quantum Electrodynamics (QED): the simple fact that the generators of the underlying group *do not* commute makes performing calculations in QCD significantly more complicated than it’s Abelian cousin QED.

In summary then, the QCD Lagrangian is given by

$$\mathcal{L}_{\text{QCD (classical)}} = -\frac{1}{4} F_{\mu\nu}^a F^{a\mu\nu} + \sum_{f=1}^6 \bar{\psi}_i^{(f)} (i \not{D} - m_f)_{ij} \psi_j^{(f)}, \quad (2.7)$$

where we have now generalised to the experimentally proven case of 6 ‘flavours’ of quark in our model (outlined previously in tab. (1.1)). This is referred to as the ‘classical’ QCD Lagrangian since we have not included quantum effects such as loop corrections. The full ‘quantum’ Lagrangian is as follows [57]:

$$\mathcal{L}_{\text{QCD}} = \sum_{f=1}^6 \bar{\psi}_i^{(f)} \left( i \not{D}^{ij} - m_f \right)_{ij} \psi_j^{(f)} - \frac{1}{4} F_{\mu\nu}^a F^{a\mu\nu} - \frac{(\partial^\mu A_\mu^a)^2}{2\xi} + (\partial^\mu \bar{c}^a) \mathcal{D}_\mu^{ab} c^b, \quad (2.8)$$

where  $\mathcal{D}_\mu$  is the covariant derivative in the adjoint representation given by

$$\mathcal{D}_\mu^{ab} = \delta^{ab}\partial_\mu - g_s f^{abc} A_\mu^c. \quad (2.9)$$

The final two terms arise from the treatment of a degeneracy in the QCD path integral which is caused by the gauge symmetry we enforced earlier - as a result we are only able to define a gluon propagator once we have “fixed the gauge” which is achieved by the penultimate term in eqn. (2.8).  $\xi$  is a free parameter in this process and, as we will see when we come to define the gluon propagator, it’s choice *defines* a specific gauge (see Appendix A). The final term is a mathematical quirk of this process and  $c$  and  $\bar{c}$  represent the resulting QCD “ghost” and “anti-ghost” fields respectively. They are unphysical since they are spin-1 anti-commuting fields.

## 2.2 The Partonic Cross-Section

Now we have a complete Lagrangian for QCD we can begin to move towards physical observables. The first step towards this is the Lehman-Symanzik-Zimmerman (LSZ) reduction formula. This gives us a relation between the scattering amplitude from some initial state into some final state,  $\langle f|i\rangle \equiv \langle f|S|i\rangle$  where  $S$  is the scattering matrix, and a time-ordered vacuum expectation operator of a product of fields. Here we briefly present the argument behind the LSZ formula for the case of  $2 \rightarrow 2$  scattering using scalar phi-cubed theory for simplicity (but this generalises to more complex theories). The Lagrangian for this theory is given by:

$$\mathcal{L}_{\text{phi-cubed}} = \frac{1}{2}\partial^\mu\phi\partial_\mu\phi + \frac{m^2}{2}\phi^2 - \frac{g}{6}\phi^3. \quad (2.10)$$

We can Fourier expand the field,  $\phi(x)$ , in terms of its annihilation and creating operators as follows:

$$\phi(x) = \int \frac{d^4k}{2E(2\pi)^3} \left( a(\vec{k})e^{ik\cdot x} + a^\dagger(\vec{k})e^{-ik\cdot x} \right), \quad (2.11)$$

and inverting this we find the following form for the creation operator  $a^\dagger(\vec{k})$ :

$$a^\dagger(\vec{k}) = i \int d^3x e^{-ix\cdot k} (\partial_0 - E) \phi(x), \quad (2.12)$$

We expect that as time flows forward to  $+\infty$  (or backwards to  $-\infty$ ) the field,  $\phi(x)$ ,

become asymptotically free and therefore we can neglect any interaction effects in these extremes. From eqn. (2.12) it is straightforward to show that:

$$a^\dagger(\vec{k}, t = \infty) - a^\dagger(\vec{k}, t = -\infty) = i \int d^4x e^{-ix \cdot k} (\partial^2 + m^2) \phi(x). \quad (2.13)$$

Clearly this would be zero if we only consider the free theory where  $g = 0$  in eqn. (2.10) - intuitively this is correct since once we remove any interaction terms a state we create at  $t = -\infty$  should flow to  $t = \infty$  unaltered. However, more generally for an interacting theory it will be non-zero and eqn. (2.13) gives us a relationship between asymptotically free initial and final states. Using eqn. (2.13) (and its hermitian conjugate) we can begin to look at the scattering from a 2 particle initial state  $|i\rangle$  to some 2 particle final state  $|f\rangle$ ,  $k_1 + k_2 \rightarrow k'_1 + k'_2$ , this is given by:

$$\langle i|j\rangle \equiv \langle 0|T \left( a(k'_1, \infty) a(k'_2, \infty) a^\dagger(k'_1, -\infty) a^\dagger(k'_2, -\infty) \right) |0\rangle, \quad (2.14)$$

where  $T$  denotes the time-ordered product of operators. After substituting for the  $a$  and  $a^\dagger$  operators and seeing that the time-ordering means that all of the remaining annihilation/creation operators end up acting on a vacuum state which they annihilate we are left with:

$$\begin{aligned} \langle i|j\rangle = i^4 \int d^4x'_1 d^4x'_2 d^4x_1 d^4x_2 & e^{ik'_1 \cdot x'_1} (\partial_{x'_1}^2 + m^2) e^{ik'_2 \cdot x'_2} (\partial_{x'_2}^2 + m^2) \times \\ & e^{ik_1 \cdot x_1} (\partial_{x_1}^2 + m^2) e^{ik_2 \cdot x_2} (\partial_{x_2}^2 + m^2) \times \\ & \langle 0|T (\phi(x'_1)\phi(x'_2)\phi(x_1)\phi(x_2)) |0\rangle. \end{aligned}$$

This is the LSZ reduction formula for  $2 \rightarrow 2$  scattering in a phi-cubed theory. It reduces the problem of finding scattering amplitudes to the calculation of time-ordered problem of fields under the assumption that we may treat the fields at  $t = \pm\infty$  as free.

The next step is to see how we can calculate these time-ordered products. This is most conveniently done by taking functional derivatives of the QCD path integral given by:

$$\mathcal{Z}[J, \eta, \bar{\eta}, \chi, \bar{\chi}] = \int \mathcal{D}A \mathcal{D}\psi \mathcal{D}\bar{\psi} \mathcal{D}c \mathcal{D}\bar{c} e^{i \int d^4x (\mathcal{L}_{QCD} + A^{\mu\nu} J_\mu^\nu + \bar{\psi}^\alpha \eta^\alpha + \bar{\eta}^\alpha \psi^\alpha + \bar{c}^\alpha \chi^\alpha + \bar{\chi}^\alpha c^\alpha)}, \quad (2.15)$$

where  $J^{\mu\nu}$ ,  $\eta^\alpha$ ,  $\bar{\eta}^\alpha$ ,  $\chi^\alpha$  and  $\bar{\chi}^\alpha$  are ‘source’ terms which we target with functional

derivatives and we have left the sum over quark flavours implicit. In order to proceed we break down eqn. (2.1) into a free Lagrangian,  $\mathcal{L}_{\text{QCD},0}$ , and an interacting Lagrangian,  $\mathcal{L}_{\text{QCD},I}$  as follows:

$$\begin{aligned}\mathcal{L}_{\text{QCD}} &= \mathcal{L}_{\text{QCD},0} + \mathcal{L}_{\text{QCD},I}, \\ \mathcal{L}_{\text{QCD},0} &= \bar{\psi}_i (i\cancel{\partial} - m)_{ij} \psi_j - \frac{1}{4} (\partial_\mu A_\nu^a - \partial_\nu A_\mu^a) (\partial^\mu A^\nu{}^a - \partial^\nu A^\mu{}^a) \\ &\quad - \frac{(\partial^\mu A_\mu^a)^2}{2\xi} + (\partial^\mu \bar{c}^a) (\partial_\mu c^a), \\ \mathcal{L}_{\text{QCD},I} &= g_s \bar{\psi}^i T_{ij}^a \gamma^\mu \psi^j - \frac{g_s}{2} f^{abc} (\partial_\mu A_\nu^a - \partial_\nu A_\mu^a) A^{b\mu} A^{c\nu} \\ &\quad - \frac{g_s^2}{4} f^{abe} f^{cde} A_\mu^a A_\nu^b A^{c\mu} A^{d\nu} - g_s f^{abc} \partial^\mu \bar{c}^a c^b A_\mu^c.\end{aligned}$$

We can then rewrite eqn. (2.15) as a combination of functional derivatives acting on the free QCD path integral,  $\mathcal{Z}_0$  as:

$$\begin{aligned}\mathcal{Z}[J, \eta, \bar{\eta}, \chi, \bar{\chi}] &= \exp \left[ i \int d^4x \mathcal{L}_{\text{QCD},I} \left( \frac{\delta}{i\delta J^{\mu a}}, \frac{\delta}{i\delta \eta^a}, \frac{\delta}{i\delta \bar{\eta}^a}, \frac{\delta}{i\delta \xi^a}, \frac{\delta}{i\delta \bar{\xi}^a} \right) \right] \\ &\quad \times \mathcal{Z}_0[J, \eta, \bar{\eta}, \chi, \bar{\chi}],\end{aligned}\tag{2.16}$$

where  $\mathcal{Z}_0$  is identical to eqn. (2.15) but with the free Lagrangian, in place of the full Lagrangian. We can solve  $\mathcal{Z}_0$  exactly which yields us the propagators for the gluons, quarks and ghosts. Respectively:

$$\langle 0 | A_a^\mu(x) A_b^\nu(y) | 0 \rangle = \int \frac{d^4k}{(2\pi)^4} e^{-ik \cdot (x-y)} \delta_{ab} \frac{i}{k^2} \left( g^{\mu\nu} - (1-\xi) \frac{k^\mu k^\nu}{k^2} \right),\tag{2.17a}$$

$$\langle 0 | \bar{\psi}_i^{(f)}(x) \psi_j^{(f')}(y) | 0 \rangle = \int \frac{d^4k}{(2\pi)^4} e^{-ik \cdot (x-y)} \delta_{ij} \delta_{ff'} \frac{i(\not{k} + m)}{k^2 - m^2},\tag{2.17b}$$

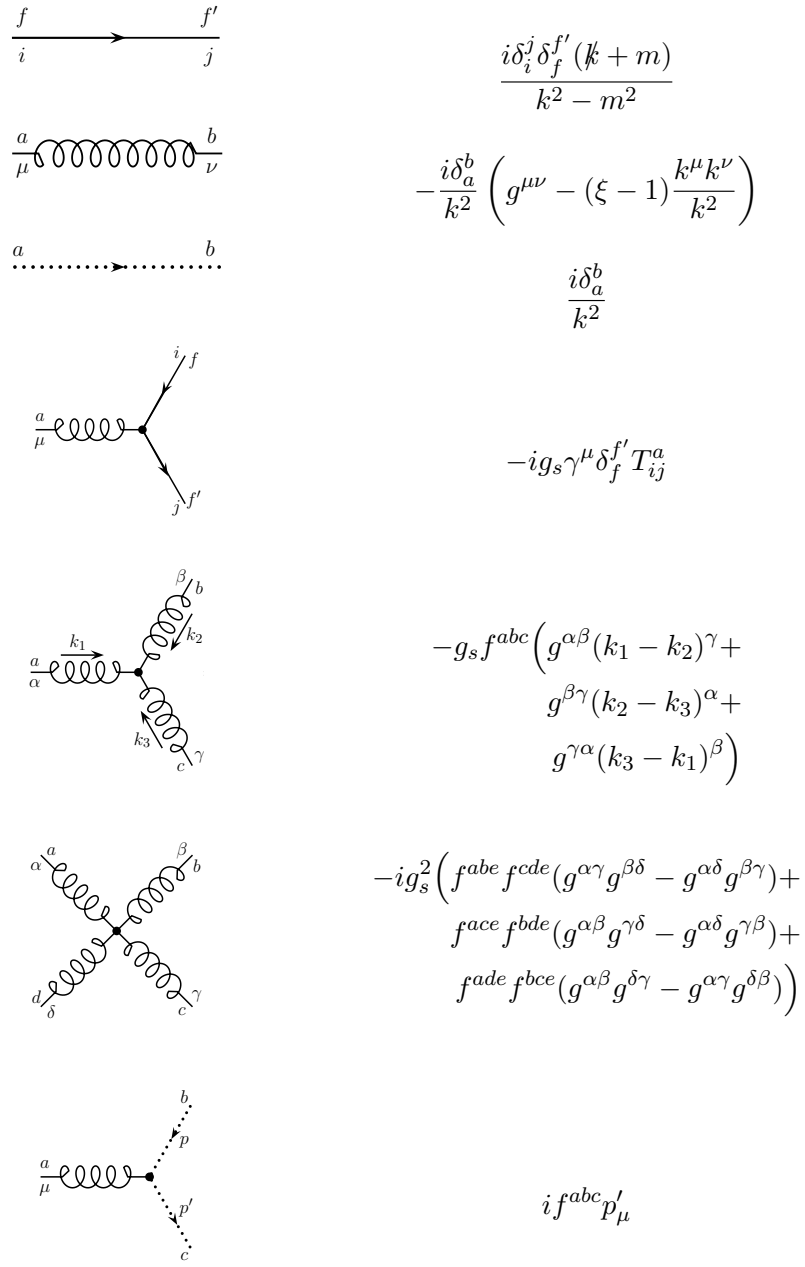
$$\langle 0 | \bar{c}_a(x) c_b(y) | 0 \rangle = \int \frac{d^4k}{(2\pi)^4} e^{-ik \cdot (x-y)} \delta_{ab} \frac{i}{k^2}.\tag{2.17c}$$

We can read off the remaining QCD vertex factors directly from the interaction Lagrangian (or - more rigorously derive them by Taylor expanding eqn. (2.16) and disregarding any irrelevant diagrams such as those where no scattering occurs or those with bubble contributions).

The full set of rules for the vertices and propagators are summarised in tab. (2.1). The

remaining *Feynman rules* may be summarised as:

Table 2.1: A graphical summary of the Feynman rules. The solid lines indicate a fermion (anti-fermion) propagator with momentum flowing parallel (anti-parallel) to the direction of the arrow. Similarly for the dashed lines which represent the ghost (anti-ghost) propagating and lastly the twisted lines depict a propagating gluon. As in the preceding equations  $i$  and  $j$  represent fundamental colour indices,  $a$  and  $b$  represent adjoint colour indices and, where present,  $f$  and  $f'$  represent fermion flavour. All Greek indices are Lorentz indices.



1. Incoming external lines with spin  $s$  and momentum  $p$  are given a factor of  $u_i^{(s)}(p)$  or  $\bar{v}_i^{(s)}(p)$  for quarks or anti-quarks. Similarly outgoing external quark or anti-quark lines get a factor  $\bar{u}_i^{(s)}(p)$  or  $v_i^{(s)}(p)$ . If the external particles are not coloured the procedure is the same but of course the spinors will no longer be  $SU(3)$  fundamental vectors. External gluons with momentum  $p$ , polarisation  $\epsilon$  and colour  $a$  are replaced by  $\epsilon^a(p)$  or  $\epsilon^{a*}(p)$  depending on whether they are incoming or outgoing.
2. For each vertex or propagator in the Feynman diagram insert the corresponding mathematical expression (see tab. (2.1)). The order of the Lorentz indices must be the same as that found by tracing the fermion lines in the diagram backwards,
3. A factor of  $-1$  must be included for each anti-fermion line flowing from the initial state to the final state,
4. A factor of  $-1$  must be included for each fermion, anti-fermion or ghost loop in the diagram
5. An integration over any unconstrained momenta in the diagram must be included with measure:

$$\int \frac{d^4k}{(2\pi)^4}, \quad (2.18)$$

where  $k$  is the momenta in question and the integral is understood to run over all four momentum components from zero up to infinity,

6. A diagram dependent symmetry factor must be included,
7. Lastly, for an unpolarised calculation we must sum over initial spin and colour and average over all possible final spins and colours.

The  $u(p)$  and  $v(p)$  are Dirac spinors which solve the free Dirac eq. for a plane-wave:

$$(i\gamma^\mu - m)u(p) = 0 \quad (i\gamma^\mu + m)v(p) = 0. \quad (2.19)$$

The result of following these Feynman rules is what we refer to as the matrix element,  $\mathcal{M}$ . We will now detail how we go from the matrix element of some scattering process to a useful physical observable: the *partonic cross-section*,  $\hat{\sigma}$ . The matrix element is related to the fully-differential cross-section by ‘Fermi’s golden rule’ which, for a scattering process  $p_a + p_b \rightarrow p_1 + \dots + p_m$  is given by

$$d\hat{\sigma} = \frac{|\mathcal{M}(p_a + p_b \rightarrow p_1^{(f)}, \dots, p_m^{(f)})|^2}{F} \times (2\pi)^4 \delta^{(4)}(p_a + p_b - p_1 - \dots - p_m) \times \frac{d^3 \vec{p}_1}{2E_1(2\pi)^3} \cdots \frac{d^3 \vec{p}_m}{2E_m(2\pi)^3}, \quad (2.20)$$

where  $F = 4\sqrt{(p_a p_b)^2 - m_a^2 m_b^2}$  is the flux of the incoming particles and the delta function acts to enforce momentum conservation for the process.

We now have a procedure for going from a scattering process we wish to calculate to the differential cross-section for that process.

## 2.3 Divergences and Regularisation

In the preceding section we saw that any unconstrained momenta in a Feynman diagram must be integrated over to account for all possible ways the momenta in the process may flow. We refer to these contributions as loop-level or higher-order corrections. When calculating these corrections we encounter divergences of various kinds which can be divided up into three classes based on how they arise.

### 2.3.1 Ultraviolet divergences

Ultraviolet divergences (UV) occur when all the components of a loop momenta grow large,  $k^\alpha \rightarrow \infty$ , such that  $k^2$  becomes the dominant term in propagator. Since these extremely high momentum modes correspond to physics at very short distance scales we choose to interpret these divergences as an indication that our theory is only a naive theory and we shouldn't attempt to apply it to all scales. We can quickly spot diagrams with these pathologies with a power counting argument. For example, given a diagram which results in a term such as the following:

$$\int \frac{d^4 k}{k^2(k^2 - m^2)}, \quad (2.21)$$

where  $m$  is some finite mass. In the UV region where  $k \rightarrow \infty$  this is asymptotically equal to:

$$\sim \int \frac{d^4k}{k^4}, \quad (2.22)$$

which is clearly logarithmically divergent.

### 2.3.2 Infrared and collinear divergences

Infrared and collinear divergences (IRC) occur in theories with massless gauge bosons, such as QED and QCD, since a particle may emit any number of arbitrarily such bosons with infinitesimal energy and we would never be able to detect their emission. In contrast to the UV divergences the IR becomes important in the region of phase space where  $k^2 \rightarrow 0$ . A similar power counting analysis to that above can be applied here. For example if we consider the one-loop correction to the vertex diagram in massless phi-cubed from section (2.2) we would find an integral of the form [64]:

$$I = \int \frac{d^4k}{(2\pi)^4} \frac{1}{k^2(p_1 - k)^2(p_2 + k)^2}, \quad (2.23)$$

where  $k$  is the loop momentum,  $q = p_1 + p_2$  is the incoming momentum and  $p_i$  the outgoing momenta. Writing each momentum in light-cone coordinates with  $p_1$  in the plus-direction,  $p_2$  in the minus-direction, such that:

$$p_1 \sim (p_1^+, 0, \vec{0}) \quad p_2 \sim (0, p_2^-, \vec{0}). \quad (2.24)$$

and then taking the Eikonal approximation, we have:

$$I = \int \frac{dk^+ k^- k_T^2}{(2\pi)^4} \frac{1}{(2k^+ k^- - k_T^2)(-2p_1^+ k^-)(2p_2^- k^+)}, \quad (2.25)$$

$$= \frac{1}{2q^2} \int \frac{dk^+ k^- k_T^2}{(2\pi)^4} \frac{1}{(2k^+ k^- - k_T^2)(-k^-)(k^+)}, \quad (2.26)$$

where  $q^2 = 2p_1 \cdot p_2$  since  $p_i$  are massless. Here we can further subdivide the divergences into a ‘soft’ sector and a collinear one.

Considering first the soft regime if we let all the components of our integration variable,  $k_\mu$  become small at the same rate, that is,  $k^\mu \sim \lambda \sqrt{q^2}$  where  $\lambda \rightarrow 0$  then after a change of variables equation (2.26) becomes:

$$I \sim \int \frac{d^4\lambda}{\lambda^4}, \quad (2.27)$$

which diverges logarithmically for small lambda. The collinear sector follows similarly if we now look at the following scaling:

$$k^\pm \sim \sqrt{q^2} \quad k^\mp \sim \lambda^2 \sqrt{q^2} \quad k_T^2 \sim \lambda \sqrt{q^2}. \quad (2.28)$$

As we decrease  $\lambda$  we make  $k_\mu$  increasingly collinear to either  $p_1$  or  $p_2$ . Using this scaling exactly reproduces eqn. (2.27) and therefore is also divergent.

### 2.3.3 Regularising divergences

If we are to extract any useful information from diagrams contributing above leading-order we must find ways to control these divergences. These methods are called ‘regularisation schemes’. The general plan with all regularisation schemes is to introduce a new parameter to the calculation which is used to get a handle on exactly *how* the integral diverges. Once we have performed the integration we take the limiting case where the effect of the regulator vanishes and we will see that the divergence now presents itself as some singular function of the regulator. There are many ways to regularise divergences each with their own advantages and disadvantages. Here we briefly describe three common approaches.

Given that the integrands seen so far only diverge in certain regions (very large or very small momenta) perhaps the most obvious thing to do is to manually introduced alter the limits of our integration. This is the momentum cut-off scheme. we simply replace the upper (lower) bound with some finite large (small) value,  $\Lambda^2$ . This will regulate any UV (soft) divergences and allow us to complete the calculation provided there are no collinear singularities which this approach cannot hope to regulate. While this method has the advantage of being very conceptually simple it also has the serious disadvantages of breaking translational and gauge invariance. Worse still is that simply limiting the integration to avoid the extremities has no effect on the collinear sector.

An alternative which *does* keep both gauge and translational invariance is the Pauli-Villars regularisation scheme [59]. In this picture we introduce an extra field (or many extra fields [43]) which has the opposite spin-statistics and therefore has the effect of suppressing the very high mass region in the integrand as follows

$$\int \frac{d^4k}{(2\pi)^4} \frac{1}{p^2 - m^2} \rightarrow \int \frac{d^4k}{(2\pi)^4} \left( \frac{1}{p^2 - m^2} - \frac{1}{p^2 - M^2} \right), \quad (2.29)$$

where  $M$  is the mass of the Pauli-Villars field with  $m \ll M$ . However, once again this does not treat any problems in the IRC sectors.

Lastly we have dimensional regularisation. Here we analytically continue the number of dimensions in our integral away from  $d = 4$ . We still want to be able to return to our physical four dimensional theory and so we choose

$$d = 4 - 2\epsilon \quad (2.30)$$

where  $\epsilon$  is the regulator by which we control the divergence. Clearly then the limit  $\epsilon \rightarrow 0$  would recover our original theory. It is worth noting that there are many conventions for defining epsilon but up to signs and factors of 2 they are equivalent. Dimensional regularisation treats both the UV and the IRC divergences and translational and gauge invariance are preserved. The disadvantage is that this modification changes the Dirac algebra relations which typically makes computing the integrals more involved.

When working in  $d$  dimensions the QCD coupling is no longer dimensionless. We can see this since the action is dimensionless and therefore we have

$$[\mathcal{L}] = d. \quad (2.31)$$

By considering the kinetic terms of the gluon and quark fields we can see that we must have

$$[g] + 2[\psi] + [A_\mu] = d, \quad (2.32)$$

and therefore

$$[g] = \frac{4-d}{2}. \quad (2.33)$$

In order to artificially fix this and restore the coupling to its dimensionless state we introduce a scale parameter,  $\mu_r$ , as follows:

$$g = g_0 \mu_r^{\frac{4-d}{2}}. \quad (2.34)$$

The introduction of this scale has important consequences for our theory. Here we follow the instructive example from [60]. If we have some dimensionless observable,  $R$ , which depends on one large scale,  $Q$ , which is much larger than all other scales in the problem (e.g. the quark masses). One would assume that  $R$  is approximately independent of this large scale but when we come to regulate and renormalise the divergences we have seen in this section the problem becomes one involving two scales and  $R$  develops a dependence on the ratio of these scales,  $\frac{Q^2}{\mu_r^2}$ . Since  $\mu_r$  is completely arbitrary  $R$  must be independent of it i.e if we now consider  $R$  as a function of both the QCD coupling strength,  $\alpha_s$ , and the ratio of the scales we must have that

$$\mu_r^2 \frac{\partial R}{\partial \mu_r^2} + \mu_r^2 \frac{\partial \alpha_s}{\partial \mu_r^2} \frac{\partial R}{\partial \alpha_s} = 0, \quad (2.35)$$

for convenience we define  $t = \ln \frac{Q^2}{\mu_r^2}$  and  $\beta(\alpha_s) = \mu_r^2 \frac{\partial \alpha_s}{\partial \mu_r^2}$  and so we can write(2.35) as

$$\frac{\partial R(e^t, \alpha_s)}{\partial t} - \beta(\alpha_s) \frac{\partial R(e^t, \alpha_s)}{\partial \alpha_s} = 0. \quad (2.36)$$

This can be solved by defining the ‘running QCD coupling’,  $\alpha = \alpha(Q^2)$

$$t = \int_{\alpha_s}^{\alpha(Q^2)} \frac{dx}{\beta(x)}, \quad (2.37)$$

where  $\alpha = \alpha(Q^2)$  admits the boundary condition  $\alpha(\mu_r^2) = \alpha_s$ . Therefore the scale dependence of our observable  $R$  comes about through its dependence on  $\alpha_s$  only.

## 2.4 The QCD Beta Function

QCD has two striking features which are not apparent from the Lagrangian derived above. The first is asymptotic freedom. This is the fact that at *high* energies the QCD coupling strength becomes increasingly weak and it is this which allows us to perform a perturbative expansion of physical observables such as cross-sections. The second feature is confinement. Confinement is the reason we do not observe bare quarks and gluons in nature, instead we only see bound states of these fundamental QCD partons. This is because at very *low* energies the coupling strength becomes increasingly strong. As we saw in section 2.3 when we renormalise QCD to remove the ultraviolet singularities we introduce a scale dependence in the coupling strength,  $\alpha_s = \alpha_s(\mu_r)$ . It can be interpreted as a measure of our ignorance of the true high-scale theory which

governs nature, that is to say, we believe QCD is the right theory *only up to* some scale  $\mu_r$ . The evolution of  $\alpha_s$  with  $\mu_r$  is given by the renormalisation group equation:

$$\mu_r^2 \frac{\partial \alpha_s}{\partial \mu_r^2} = \beta(\alpha_s(\mu_r^2)), \quad (2.38)$$

where  $\beta(\alpha_s)$  is the beta function. It can be expanded perturbatively as a series in  $\alpha_s$  as follows:

$$\beta(\alpha_s) = -\beta_0 \alpha_s (1 + \beta_1 \alpha_s + \beta_2 \alpha_s^2 + \dots), \quad (2.39)$$

where the perturbative coefficients,  $\beta_i$ , can be calculated using the methods of section ((2.2)). For example the leading order contribution,  $\beta_0$ , is given by:

$$\beta_0 = 11 - \frac{2n_f}{3}. \quad (2.40)$$

If we truncate eq. (2.39) at leading-order in  $\alpha_s$  then we can solve eq. (2.38) and we see that the coupling,  $\alpha_s(\mu_r)$ , ‘runs’ with the following form:

$$\alpha_s(Q^2) = \frac{\alpha_s(\mu_r^2)}{1 + \alpha(\mu_r^2) \frac{\beta_0}{4\pi} \ln \frac{Q^2}{\mu_r^2}}. \quad (2.41)$$

It is clear from this (since in the standard model we have  $n_f \leq 6$  and therefore  $\beta_0 > 0^2$ ) that as  $Q^2$  tends to zero the coupling strength becomes very large and at high values for  $Q^2$  we see that  $\alpha_s(Q^2) \rightarrow 0$ . This later limit is exactly the asymptotic freedom property of QCD and it holds even when we include the higher order terms we neglected in the leading-order approximation used to arrive at eq. (2.41) [23]. It is an essential result in that it allows us to perform perturbative expansions of observables and without this none of the following work would be possible. The evolution of the strong coupling with  $Q^2$  is shown in fig. (2.1), it shows several extracted values of  $\alpha_s$  based on six various types of experiment. For example, the hadronic collider predictions include studies of the ratio of the 3-jet inclusive cross-section to the 2-jet inclusive cross-section as a means of finding the strong coupling [31].

---

<sup>2</sup>The number of fermions we consider depends on the energy scale we are at. Clearly we must be at an energy larger than the mass of any given quark for it to be produced. This was experimentally observed in the famous  $R$ -ratio where the ratio of the  $e^+e^- \rightarrow$  hadrons cross-section to the  $e^+e^- \rightarrow \mu^+\mu^-$  cross-section was investigated

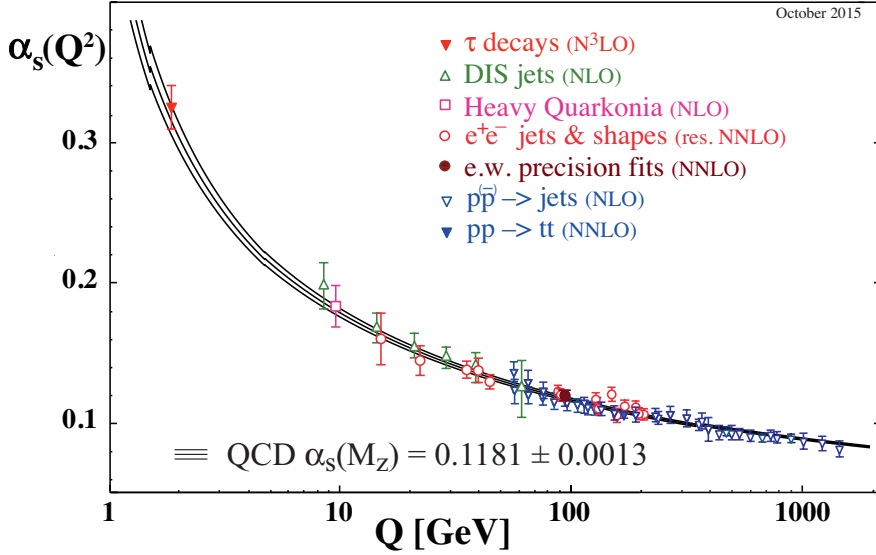


Figure 2.1: The evolution of  $\alpha_s$  over several orders of magnitude in the scale of the process  $Q^2$ . The data points fitted are of varying degrees of formal accuracy ranging from next-to-leading order in  $\alpha_s$  (NLO) to next-to-next-to-next-to-leading order in  $\alpha_s$  ( $N^3LO$ ). Fig. from [23].

## 2.5 QCD Factorisation at Hadronic Colliders

So far we have only talked about the very general idea of two particles interacting and scattering off one another into some final state which we are interested in. This is too simple a picture when we are considering hadronic colliders such as the Large Hadron Collider (proton-proton), the Tevatron (proton-antiproton), HERA (proton-lepton) and, potentially, a Future Circular Collider (FCC) with a hadronic initial state. At experiments we collide QCD bound states with one another but in practice when calculating cross-sections we perform a sum over the possible combinations of initial states we may encounter in the two incoming hadrons. In order to do this we must have a good understanding of the dynamics of the partons inside the onrushing hadrons; this understanding is encoded in the Parton Distribution Functions (PDFs). A PDF,  $f_{i/H}(x, Q^2)$  is a function which tells us how likely we are to find a parton of type  $i$  carrying a fraction  $x$  of the total hadron's momentum in a hadron, of type  $H$ , during a collision occurring at an energy scale  $Q$ . Because the PDFs contain non-perturbative information we cannot compute their properties in the same way as we calculate cross-sections, instead they are determined by fitting to data from a range of experiments (such as those mentioned above). Once we have the PDFs we can compute the physical hadronic cross-sections,  $\sigma$ , by convoluting two of them (one for each hadron) with the partonic cross-section for the scattering of partons of type  $i$  and  $j$ ,  $\hat{\sigma}_{ij}$ , discussed in

section (2.2) and summing over the possible initial partons as follows:

$$\sigma(Q^2) = \sum_{f_a, f_b} \int_0^1 dx_a dx_b f_{a/H_a}(x_a, Q^2) f_{b/H_b}(x_b, Q^2) \hat{\sigma}_{ij}(\alpha_s(\mu_r), \mu_r^2, \mu_f^2). \quad (2.42)$$

Eq. (2.42) can be intuitively understood as a separation of scales; the long distance physics of the PDFs is manifestly distinct from the short distance hard scatter contained in the partonic cross-section. The scale at which we separate the long and short range physics is called the *factorisation scale*,  $\mu_f$ . As with the renormalisation scale it is not *a priori* clear what is the correct factorisation scale and results of perturbative calculations are often quoted with a ‘scale uncertainty’ band.

## 2.6 From Partons to Jets

As alluded to in section (2.4) the computation of scattering amplitudes can only take us so far when comparing simulations to experiments. In particular, the final state quarks and gluons in our perturbative picture of QCD differ from the confined hadrons observed at hadronic colliders: It is well known that final state QCD partons fragment and emit showers of additional radiation before finally they becomes colourless bound states in a process known as ‘hadronisation’. This process is not perturbatively well-understood since it occurs at scale, often called  $\Lambda_{\text{QCD}}$ , at which QCD becomes non-perturbative, *i.e.* the coupling constant of the theory has become too large for us to legitimately truncate a perturbative expansion. There are models for both the ‘parton shower’ behaviour of the energetic final state partons, such as **Pythia** [63], **Herwig** [32] and **Sherpa** [49] as well as models for the hadronisation such as the ‘Lund string model’ [19] implemented in various physics software packages but most relevantly (for the remainder of this thesis) - in the **Ariadne** code [14, 55].

All high energy collider experiments see a great deal of QCD radiation in the final state. This radiation, produced through the mechanisms outlined above, appears in columnated structures called ‘jets’ and so it is at the jet level that we may compare our simulated results to actual measurements. The question of how we best map from the two or more parton level to the jet level is not a trivial one: a single high-energy (or ‘hard’) parton may split and form two final state jets but equally two low energy (or ‘soft’) partons may combine into a single jet.

There are several approaches to this problem include the **SISCone** algorithm [61] and Pythia’s own implementation **CellJet** [62]. However the most commonly user family of jet reconstruction algorithm are know as the ‘sequential recombination algorithms’.

This group of approaches include the Cambridge-Aachen,  $k_T$  and anti- $k_T$  algorithms. The general algorithm, as given in [29], is:

1. Given a list of final state partons calculate some generalised distance,  $d_{ij}$ , between all possible combinations of jets  $i$  and  $j$  as well as  $d_{iB}$  where  $B$  is the beam-line,
2. We identify the smallest value of these. If, say  $d_{ab}$  is the smallest, we combine partons  $a$  and  $b$ . If however  $d_{aB}$  is the smallest then we call  $a$  a jet and remove it from the list of partons,
3. We then recompute all the generalised distances and repeat steps 1 and 2 until no further partons remain,

where the generalised distances are defined as

$$d_{ij} = \min(k_{Ti}^{2p}, k_{Tj}^{2p}) \frac{\Delta R^2}{R^2}, \quad (2.43)$$

$$d_{iB} = k_{Ti}^{2p},$$

where  $k_{Ti}$  is the transverse momentum of the  $i^{th}$  parton,  $R$  is a free parameter in the clustering which relates to the size of the jets and  $\Delta R^2$  is the distance in the detector metric between the two partons given by  $\Delta R^2 = \Delta\phi^2 + \Delta y^2$  where  $\Delta\phi$  and  $\Delta y$  are the angular distance (about the beam line) between the partons and the rapidity gap between the partons respectively. The parameter is  $p$  and it is this which specifies precisely which clustering algorithm we are using;  $p = 0$  reduces to the Cambridge-Aachen scheme while  $p = \pm 1$  give the  $k_T$  and anti- $k_T$  respectively. The question of which to use is outlined in detail in [29] but we give a brief summary here.

The choice of jet algorithm boils down to a handful of key properties the algorithm must exhibit. Given a set of hard QCD final states we require that the result of the clustering algorithm, i.e. the jets and jet shapes, are not unduly sensitive to additional soft and collinear radiation. This is intuitively clear since, for example, a final state with a single high energy quark with momentum,  $k_{Ti}$ , may radiate infinitely a multitude of infinitely soft gluons,  $k_{Ts_i}$ , which may (or may not) be collinear to the original parton - but since  $k_{Ts_i} \ll k_{Ti}$  the result must be a single jet,  $j_{Ti}$ , which has  $j_{Ti} \sim k_{Ti}$ . Any algorithm which satisfies this is said to be infra-red and collinear (IRC) safe. We also want an algorithm which is insensitive to the hadronisation model used, or any possible extra multiple-parton or experimental pile-up emissions since these things are, at present, poorly understood. It is also worth mentioning that since jet clustering algorithms are used in experimental triggers to quickly categorise events they should

be as computationally cheap as possible.

Although the Cambridge-Aachen algorithm has advantages in some experimental searches such as studies where the substructure of jets is of particular interest [4,27], the most widely used sequential recombination algorithm is the anti- $k_t$  algorithm ( $p = -1$ ) and so all of the work which follows and all of the experimental comparisons made will use this as the method for mapping simulated parton level results to a more useful set of jet level results. The jet size parameter  $R$  varies between experiments but is typically either 0.4 for ATLAS analyses or 0.5 for CMS analyses.

## 2.7 Perturbative QCD and Resummation

In section 2.2 we saw that we could separate out the QCD Lagrangian into free and interacting components and that vacuum expectations of time ordered fields could be found by taking functional derivatives of the free partition function (eqn. (2.16)). Since terms which give rise to interactions in the Lagrangian come with a factor of the coupling strength,  $g$ , Taylor expanding the exponential in eqn. (2.16) will yield an infinite series of terms and, in principle, in order to compute any physical observable we must calculate we must evaluate all of these. Of course in practice this is not possible. We must choose a subset of terms from this infinite array which we reason will give the *best possible approximation to the full series*.

### 2.7.1 Fixed-order Perturbation

The fixed-order perturbative approach operates on the assumption that since, as we saw in section 2.4, the coupling strength  $\alpha_s$  in the expansion becomes small at large energy scales we may truncate the series at some power of  $\alpha_s$ . For example given a cross-section of a scattering  $X \rightarrow Y$  we wish to calculate, the fixed order picture of the expansion would be:

$$\sigma_{X \rightarrow Y} = \alpha_s^{i_0}(Q^2) \sum_{i=1}^N \alpha_s^i(Q^2) \mathcal{C}_{X \rightarrow Y}^{(i)} \quad (2.44)$$

where  $i_0$  accounts for processes which start above tree level and  $\mathcal{C}_{X \rightarrow Y}^{(i)}$  are the coefficient terms which encode the kinematics of the diagrams contributing at each ‘order’ in the series. Since we expect that the more terms we can calculate the better our truncated series will approximate the full result we should choose  $N$  as large as possible though in

principal it is determined by the complexity and the computational cost of the relevant calculation of the coefficient functions. Recent progress has allowed the automation of next-to-leading order QCD calculations ( $N = 2$ ) in packages such in `aMC@NLO_MadGraph` (v5) [10], `BlackHat` [24], `MC@NLO` [41] and `Powheg` [40]. In general it is not known how to compute multi-loop (i.e.  $N \geq 3$ ) calculations and while process specific calculations have been completed [28, 44, 46], it is still very much a hot topic in theoretical physics. It is important to note the limitations of this fixed-order scheme. For example, if we were to consider NLO corrections to dijet production we would only be able to produce final states with two or three jets (since we can only have one extra real emission). Clearly this is a limitation since the external fermion lines can radiate arbitrarily many extra gluons. It is precisely this phenomenon which is shown in fig. 9, the NLO calculations (shown in green and black) are limited to  $\langle \text{jets} \rangle \leq 3$  which the predictions from `POWHEJ+PYTHIA` and `HEJ` which include higher-order corrections predict a higher average number of jets. Note that the higher-order corrections here are *not* the same in the case of `POWHEJ+PYTHIA` and `HEJ`. Also note that although the scale uncertainty band of the NLO calculation *does* exceed  $\langle \text{jets} \rangle = 3$  this is not a result of the formalism but instead comes about as the result of an attempt to quantify the residual dependence of the calculation on the factorisation and renormalisation scales. This scale dependence of observables will be discussed in more detail in chapter 4.

There are frameworks to allow the ‘merging’ of NLO calculations of different multiplicity. A comprehensive review of such methods may be found in [8].

We now present an instructive fixed-order calculation of the next-to-leading corrections to quark-antiquark pair production via an off-shell photon [37].

### 2.7.2 An Example Fixed-Order Calculation

The Feynman diagrams which need to be included for the  $\mathcal{O}(1)$  and  $\mathcal{O}(\alpha_s)$  corrections to the  $\gamma^* \rightarrow q\bar{q}$  process are shown in fig. (2.3). We refer to fig. (2.3a) as the tree level diagram, fig. (2.3b) as the vertex correction and figs. (2.3c) and (2.3d) as the self-energy corrections. Figs. (2.3e) and (2.3f) are the ‘real corrections’. Since the virtual corrections all have the same final state they must be summed and squared together. To make the order of each term in the perturbative expansion clear we extract the  $\alpha_s$  factors from the  $\mathcal{A}_i$  here. Therefore:

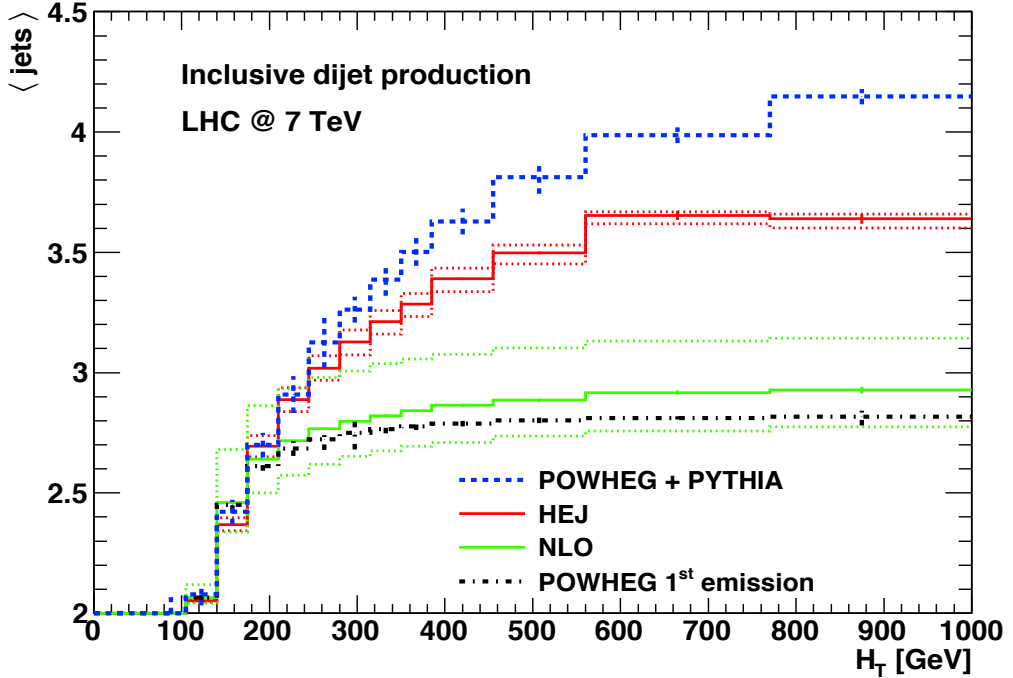


Figure 2.2: Simulations of the average number of jets as a function of the sum of the transverse momenta in the event,  $H_T$ , for inclusive dijets at a 7TeV LHC.

$$\begin{aligned}
|\mathcal{M}|^2 = & |\mathcal{A}_0 + \alpha_s \mathcal{A}_v + \alpha_s \mathcal{A}_{se1} + \alpha_s \mathcal{A}_{se2}|^2 + \mathcal{O}(\alpha_s^2) \\
= & |\mathcal{A}_0|^2 + 2\alpha_s \Re\{\mathcal{A}_0^* \mathcal{A}_v\} + 2\alpha_s \Re\{\mathcal{A}_0^* \mathcal{A}_{se1}\} \\
& + 2\alpha_s \Re\{\mathcal{A}_0^* \mathcal{A}_{se2}\} + \mathcal{O}(\alpha_s^2),
\end{aligned} \tag{2.45}$$

We can see then that to  $\mathcal{O}(\alpha_s)$  we have four contributions to consider, but the two self-energy contributions will have the same functional form so it would seem that in practice we only need to perform three calculations - it turns out this is not the case; we will find that the divergence associated with exchanging a soft gluon in fig. (2.3b) can only be cancelled if we also include the soft divergences that arise from figs. (2.3e) to (2.3f). At first glance this seems very peculiar since these diagrams have different final states and therefore should have no business contributing to this calculation. However, since the gluon can be emitted with vanishingly small momentum it would be experimentally impossible to detect and therefore the final states would look the same to an imperfect observer.

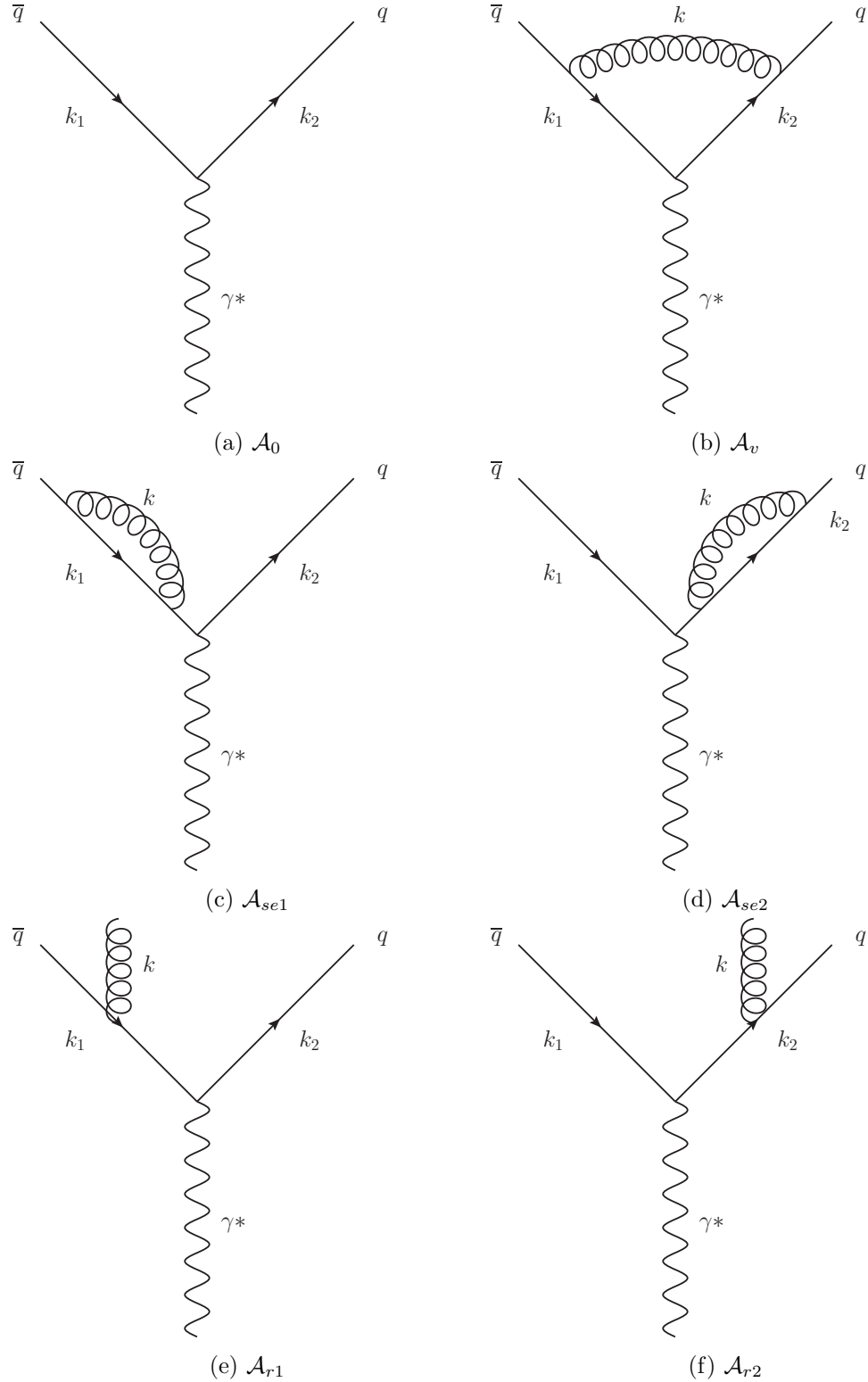


Figure 2.3: Feynman diagrams for calculating the  $O(\alpha_s)$  correction to  $\gamma^* \rightarrow q\bar{q}$ . Fig. (2.3a) is the leading order contribution. Figs. (2.3b) - 2.3d are the virtual corrections and lastly figs. (2.3e) - (2.3f) are the real emission contributions.

It is the cancellation of these divergences that will be shown in detail in the next two sections. Figs. (2.3a), (2.3b) and (2.3e) will be calculated in detail while the result for the self energy expressions will be omitted since it can be cancelled by choosing to work in the Landau gauge [37]. Since we expect both UV and IR divergences we choose to work in the dimensional regularisation scheme.

### The Leading Order Process

If we let the pair-produced quarks have charge  $\pm Qe$  then the Feynman rules outlined in section 2.2 give:

$$\mathcal{A}_0 = -ieQ\bar{u}^{\lambda_2}(k_2)\gamma^\mu v^{\lambda_1}(k_1)\epsilon_\mu^r(p), \quad (2.46)$$

where we have used the QED Feynman rule for a quark-antiquark-photon vertex:  $iQe\gamma^\mu$ , the  $\lambda_i$ 's are the spins of the quarks,  $r$  is the polarisation of the incoming photon and  $p = k_1 + k_2$  is the momentum carried by the incoming photon. To calculate we can square and since we are typically interested in unpolarised calculations we perform a sum over all polarisations and spins (we also choose this point to include the sum over the possible colour states of the outgoing quarks):

$$|\overline{\mathcal{A}_0}|^2 = 3 \sum_{\forall \lambda, r} e^2 Q^2 [\bar{u}^{\lambda_2}(k_2)\gamma^\mu v^{\lambda_1}(k_1)][\bar{v}^{\lambda_1}(k_1)\gamma^\nu v^{\lambda_2}(k_1)]\epsilon_\mu^r(p)\epsilon_{*\mu}^r(p). \quad (2.47)$$

We can now use Casimir's trick [47] to convert this spinor string into a trace, using the replacements  $\sum_r \epsilon_\mu^r \epsilon_{*\nu}^r = -g_{\mu\nu}$  and the completeness conditions for spinors:

$$|\overline{\mathcal{A}_0}|^2 = -e^2 Q^2 \text{Tr}[\not{k}_2 \gamma^\mu \not{k}_1 \gamma_\mu], \quad (2.48)$$

where we have used the high energy limit to discard the quark mass terms. This trace can be evaluated in arbitrary dimensions to give, in the high energy limit:

$$|\overline{\mathcal{A}_0}|^2 = 6e_d^2 Q^2 s(d-2), \quad (2.49)$$

where we have defined the usual Mandelstam variable  $s = (k_1+k_2)^2 = 2k_1 \cdot k_2$  and define  $e_d^2 = e^2 \mu^{4-d}$  where  $\mu$  has units of mass in order to make the coupling  $e$  dimensionless. To find the leading order cross-section we divide by the particle flux and multiply by the two particle phase space which is given by:

$$\int d^{2d-2}R_2 = 2^{1-d}\pi^{\frac{d}{2}-1} \frac{\Gamma(\frac{d}{2}-1)}{\Gamma(d-2)} s^{\frac{d-4}{2}}, \quad (2.50)$$

where  $R_2$  is the two particle phase space in  $d$  dimensions. Combining these factors and defining  $\alpha_e = \frac{e^2}{4\pi}$ :

$$\begin{aligned} \sigma_0 &= 3 \cdot 2^{2-d} \pi^{1-\frac{d}{2}} \frac{\Gamma(\frac{d}{2}-1)}{\Gamma(d-2)} s^{\frac{d-4}{2}} 4\pi\alpha\mu^{d-4} Q^2 s(d-2) \frac{1}{2s} \\ &= 3\alpha Q^2 \left( \frac{s}{4\pi\mu^2} \right)^{\frac{d}{2}-2} \left( \frac{d}{2}-1 \right) \frac{\Gamma(\frac{d}{2}-1)}{\Gamma(d-2)}. \end{aligned} \quad (2.51)$$

and finally using  $x\Gamma(x) = \Gamma(x+1)$  we get:

$$\sigma_0 = 3\alpha Q^2 \frac{\Gamma(\frac{d}{2})}{\Gamma(d-2)} \left( \frac{s}{4\pi\mu^2} \right)^{\frac{d}{2}-2}. \quad (2.52)$$

It is important to note that in the limit  $\epsilon \rightarrow 0$  the Born cross-section remains finite.

### The Virtual $\mathcal{O}(\alpha_s)$ Corrections

The virtual correction graphs are shown in figs. (2.3b), (2.3c) and (2.3d). We will begin by calculating the second term in eqn. (2.45). Using the Feynman rules we have:

$$\begin{aligned} \mathcal{A}_v &= \int \frac{d^d k}{(2\pi)^d} \bar{u}^{\lambda_2}(k_2) (-ig_s \mu^\epsilon \gamma^\alpha T_{ij}^a) \frac{i(\not{k}_1 + \not{k})}{(k_1 + k)^2} (-ieQ \gamma^\mu) \frac{i(\not{k}_2 - \not{k})}{(k_2 - k)^2} \\ &\quad (-g_s \mu^\epsilon \gamma^\beta T_{ij}^a) \epsilon_\mu^r(p) \frac{-i}{k^2} \left( g_{\alpha\beta} + (1 - \xi) \frac{k^\alpha k^\beta}{k^2} \right) v^{\lambda_1}(k_1). \end{aligned}$$

$$\mathcal{A}_v = -ig_s^2 e Q \mu^{2\epsilon} \text{Tr}(T^a T^a) \bar{u}^{\lambda_2}(k_2) \int \frac{d^d k}{(2\pi)^d} \frac{\mathcal{N}_1(k_1, k_2, k)}{k^2 (k_1 + k)^2 (k_2 - k)^2} v^{\lambda_2}(k_2),$$

where the numerator of the fraction is given by:

$$\mathcal{N}_1(k_1, k_2, k) = \gamma^\alpha (\not{k}_1 + \not{k}) \gamma^\mu (\not{k}_2 - \not{k}) \gamma_\beta \left( g^{\alpha\beta} + (1 - \xi) \frac{k^\alpha k^\beta}{k^2} \right). \quad (2.54)$$

From eqn. (2.45) we see we need  $\mathcal{A}_0^* \mathcal{A}_v$ :

$$\mathcal{A}_0^* \mathcal{A}_v = g_s^2 e^2 Q^2 \text{Tr}(T^a T^a) [\bar{v}^{\lambda_1}(k_1) \gamma^\nu u(k_2)] \quad (2.55)$$

$$\left[ \bar{u}^{\lambda_2}(k_2) \int \frac{d^d k}{(2\pi)^d} \frac{\mathcal{N}_1(k_1, k_2, k)}{k^2(k_1 + k)^2(k_2 - k)^2} v^{\lambda_1}(k_1) \right] \epsilon_\mu^r(p) \epsilon_{*\nu}^r(p). \quad (2.56)$$

Now performing the spin/polarisation/colour sum and average gives:

$$\overline{\mathcal{A}_0^* \mathcal{A}_v} = -\frac{g_s^2 e^2 Q^2}{2} \int \frac{d^d k}{(2\pi)^d} \frac{\mathcal{N}_2(k_1, k_2, k)}{k^2(k_1 + k)^2(k_2 - k)^2}, \quad (2.57)$$

where:

$$\mathcal{N}_2(k_1, k_2, k) = \text{Tr}[\not{k}_1 \gamma_\alpha (\not{k}_1 + \not{k}) \gamma_\mu (\not{k}_2 - \not{k}) \gamma_\beta \not{k}_2 \gamma^\mu] \left( g^{\alpha\beta} + (1 - \xi) \frac{k^\alpha k^\beta}{k^2} \right). \quad (2.58)$$

Before we can proceed any further we must evaluate the trace term in the integral. As mentioned briefly in section 2.3.3 this is not as easy as it seems because, although the Dirac matrices still satisfy the Clifford algebra, the various identities for their contractions and traces change when we are in  $d$  dimensions. Two useful examples are shown below:

$$g_{\mu\nu} g^{\mu\nu} = d \quad (2.59a)$$

$$\gamma^\mu \gamma_\nu \gamma_\mu = (d - 2) \gamma_n u \quad (2.59b)$$

Using the FORM package [53] to perform the two trace terms present gives:

$$\begin{aligned} \text{Tr}[\not{k}_1 \gamma_\alpha (\not{k}_1 + \not{k}) \gamma_\mu (\not{k}_2 - \not{k}) \gamma^\alpha \not{k}_2 \gamma^\mu] &= s[s(8 - 4d) + \frac{(k_1 \cdot k)(k_2 \cdot k)}{s}(32 - 16d) \\ &\quad - (16 - 8d)(k_1 \cdot k - k_2 \cdot k) + k^2(16 - 12d + 2d^2)], \end{aligned} \quad (2.60)$$

and,

$$\begin{aligned} \text{Tr}[\not{k}_1 \gamma_\alpha (\not{k}_1 + \not{k}) \gamma_\mu (\not{k}_2 - \not{k}) \gamma_\beta \not{k}_2 \gamma^\mu] k^\alpha k^\beta &= s[(k_1 \cdot k)(k_2 \cdot k)(16 - 8d) \\ &\quad + k^2(8 - 4d)(k_2 \cdot k - k_1 \cdot k) - k^4(4 - 2d)], \end{aligned} \quad (2.61)$$

where  $s = 2k_1 \cdot k_2$  and we have used the on-shell relations. After factorising the terms quadratic in  $d$  and combining the two trace terms we arrive at:

$$\overline{\mathcal{A}_0^* \mathcal{A}_v} = -4s \left( \frac{d}{2} - 1 \right) \frac{g_s^2 e^2 Q^2}{2} \int \frac{d^d k}{(2\pi)^d} \frac{\mathcal{N}_3(k_1, k_2, k)}{k^2(k_1 + k)^2(k_2 - k)^2}, \quad (2.62)$$

where:

$$\mathcal{N}_3(k_1, k_2, k) = -2s + \frac{8k \cdot k_1 k \cdot k_2}{s} + (6 + 2\xi)(k \cdot k_1 - k \cdot k_2) + k^2(d - 4) \quad (2.63)$$

$$-4(1 - \xi) \frac{k \cdot k_1 k \cdot k_2}{k^2} - (1 - \xi)k^2. \quad (2.64)$$

Combining this with the particle flux and the two particle phase space we can write an expression for the vertex corrected cross-section. Once again we scale the couplings such that they remain dimensionless by defining  $g_d^2 = g_s^2 \mu^{2-\frac{d}{2}}$ :

$$\begin{aligned} \sigma_v &= -4s \left( \frac{d}{2} - 1 \right) \frac{g_d^2 \mu^{2-\frac{d}{2}} e^2 Q^2}{4s} 2^{1-d} \pi^{\frac{d}{2}-1} \frac{\Gamma(\frac{d}{2}-1)}{\Gamma(d-2)} s^{\frac{d-4}{2}} \int \frac{d^d k}{(2\pi)^d} \frac{\mathcal{N}_3(k_1, k_2, k)}{k^2(k_1 + k)^2(k_2 - k)^2}, \\ \Rightarrow \sigma_v &= -g_d^2 \mu^{2-\frac{d}{2}} Q^2 4\pi \alpha \mu^{4-d} 2^{1-d} \pi^{\frac{d}{2}-1} \frac{\Gamma(\frac{d}{2})}{\Gamma(d-2)} s^{\frac{d-4}{2}} \int \frac{d^d k}{(2\pi)^d} \frac{\mathcal{N}_3(k_1, k_2, k)}{k^2(k_1 + k)^2(k_2 - k)^2}, \\ \Rightarrow \sigma_v &= -\frac{4\sigma_0}{3} g_d^2 \mu^{2-\frac{d}{2}} \int \frac{d^d k}{(2\pi)^d} \frac{\mathcal{N}_3(k_1, k_2, k)}{k^2(k_1 + k)^2(k_2 - k)^2}, \end{aligned}$$

where we have expressed the virtual rate as a multiplicative correction to the Born level rate by comparing directly with eq. (35). We must now use the Feynman parametrisation to re-express the product of propagators as a sum by introducing new integration variables. Using:

$$\frac{1}{ab} = \int_0^1 dy \frac{1}{(ay + b(1-y))^2}, \quad (2.66)$$

we have:

$$\sigma_v = -\frac{4\sigma_0}{3} g_d^2 \mu^{2-\frac{d}{2}} \int \frac{d^d k}{(2\pi)^d} \int_0^1 dy \frac{\mathcal{N}_3(k_1, k_2, k)}{(k^2 - 2k \cdot k_y)^2 k^2}, \quad (2.67)$$

where  $k_y = yk_1 - (1-y)k_2$ . Examining now the integrand we see there are two different

$k$  dependences and so we partition the terms as follows:

$$\sigma_v = -\frac{4\sigma_0}{3} g_d^2 \mu^{2-\frac{d}{2}} \int \frac{d^d k}{(2\pi)^d} \int_0^1 dy \left( \frac{\mathcal{N}'_3(k_1, k_2, k)}{(k^2 - 2k \cdot k_y)^2 k^2} + \frac{\mathcal{N}''_3(k_1, k_2, k)}{(k^2 - 2k \cdot k_y)^2 k^4} \right), \quad (2.68)$$

where,

$$\mathcal{N}'_3(k_1, k_2, k) = -2s + \frac{8k \cdot k_1 k \cdot k_2}{s} + (6+2\xi)(k \cdot k_1 - k \cdot k_2) + k^2(d-4) - (1-\xi)k^2. \quad (2.69a)$$

$$\mathcal{N}''_3(k_1, k_2, k) = -4(1-\xi)k \cdot k_1 k \cdot k_2. \quad (2.69b)$$

Differentiating eqn. (2.66) with respect to  $a$  and  $b$  we get the following useful parametrisations:

$$\frac{1}{a^2 b} = \int_0^1 dx \frac{2x}{(ax + b(1-x))^3}, \quad (2.70a)$$

$$\frac{1}{a^2 b^2} = \int_0^1 dx \frac{6x(1-x)}{(ax + b(1-x))^4}. \quad (2.70b)$$

and taking  $a = k^2 - 2k \cdot k_y$  and  $b = k^2$ , simplifying the denominators and performing a change of variables  $K = k - xp_y$  yields:

$$\sigma_v = -\frac{4\sigma_0}{3} g_d^2 \mu^{2-\frac{d}{2}} \int \frac{d^d K}{(2\pi)^d} \int_0^1 dy \int_0^1 dx \left( \frac{2x\mathcal{N}'_3(k_1, k_2, K + xk_y)}{(K^2 - C)^3} + \right. \quad (2.71)$$

$$\left. \frac{6x(1-x)\mathcal{N}''_3(k_1, k_2, K + xk_y)}{(K^2 - C)^4} \right), \quad (2.72)$$

where  $C = x^2 p_y^2$ . The change of variables modifies the numerator terms to:

$$\begin{aligned} \mathcal{N}'_3(k_1, k_2, K + xk_y) &= -2s + K^2 \left( \frac{4}{d} + d - 5 + \xi \right) \\ &\quad - (3 + \xi)xs + x^2 ys(1 - y)(3 - d - \xi), \end{aligned} \quad (2.73a)$$

$$\mathcal{N}''_3(k_1, k_2, K + xk_y) = (1 - \xi) \left( x^2 ys^2(1 - y) - \frac{2s}{d} K^2 \right). \quad (2.73b)$$

We can now perform the integrations over  $K$  with the aid of the following result:

$$\int \frac{d^d K}{(2\pi)^d} \frac{(K^2)^m}{(K^2 - C)^n} = \frac{i(-1)^{m-n}}{(4\pi)^{\frac{d}{2}}} C^{m-n+\frac{d}{2}} \frac{\Gamma(m + \frac{d}{2}) \Gamma(n - m - \frac{d}{2})}{\Gamma(\frac{d}{2}) \Gamma(n)}. \quad (2.74)$$

Looking at the  $K$  structure of eqs. (2.73) we can see that there are going to be 4 forms of eqn. (2.74) needed in this calculation. I will not show the calculation for every integral but will show one as an example of how the calculations can proceed. Consider the contribution of the first term of eqn. (2.73a):

$$I = -4s \int_0^1 dy \int_0^1 dxx \int \frac{d^d K}{(2\pi)^d} \frac{1}{(K^2 - C)^3} = 4si \int_0^1 dy \int_0^1 dxx (4\pi)^{-\frac{d}{2}} C^{-3+\frac{d}{2}} \frac{\Gamma(\frac{d}{2}) \Gamma(3 - \frac{d}{2})}{\Gamma(\frac{d}{2}) \Gamma(3)}.$$

From above we see that  $C = x^2 k_y = -x^2 y(1-y)s$  and so:

$$I = 4si(4\pi)^{-\frac{d}{2}} \Gamma(3 - \frac{d}{2})(-s)^{-3+\frac{d}{2}} \int_0^1 dy \int_0^1 dxx^{-5+d} y^{(-2+\frac{d}{2})-1} (1-y)^{(-2+\frac{d}{2})-1}, \quad (2.75)$$

Therefore:

$$I = 4si(4\pi)^{-\frac{d}{2}} \Gamma\left(3 - \frac{d}{2}\right) (-s)^{-3+\frac{d}{2}} \frac{1}{d-4} \frac{\Gamma^2(\frac{d}{2}-2)}{\Gamma(d-4)}. \quad (2.76)$$

Choosing  $d = 4 + \epsilon$  (with the intention of taking the limit  $\epsilon \rightarrow 0$  once it is safe to do so), and manipulating the gamma functions to expose the pole structure gives:

$$-4 \int_0^1 dy \int_0^1 dxx \int \frac{d^d K}{(2\pi)^d} \frac{1}{(K^2 - C)^3} = 4(-s)^{\frac{\epsilon}{2}} i(4\pi)^{-2-\frac{\epsilon}{2}} \frac{4}{\epsilon^2} \frac{\Gamma(1 - \frac{\epsilon}{2}) \Gamma^2(1 + \frac{\epsilon}{2})}{\Gamma(1 + \epsilon)}, \quad (2.77)$$

which is clearly divergent in the limit  $d \rightarrow 4$ . The other integrals follow similarly and the combined result can be expressed as:

$$\sigma_v = \frac{2\alpha_s}{3\pi} \sigma_0 \left( \frac{s}{4\pi\mu^2} \right)^{\frac{\epsilon}{2}} \frac{\Gamma\left(1 - \frac{\epsilon}{2}\right) \Gamma^2\left(1 + \frac{\epsilon}{2}\right)}{\Gamma(1 + \epsilon)} \left( -\frac{8}{\epsilon^2} + \frac{6}{\epsilon} - \frac{8 + 4\epsilon}{1 + \epsilon} \right), \quad (2.78)$$

where we have defined  $\alpha_s = \frac{g_d^2}{4\pi}$ . Expanding the product of gamma matrices for  $\epsilon \rightarrow 0$  gives:

$$\frac{\Gamma\left(1 - \frac{\epsilon}{2}\right) \Gamma^2\left(1 + \frac{\epsilon}{2}\right)}{\Gamma(1 + \epsilon)} = \frac{\gamma_E}{2}\epsilon + \left( \frac{\gamma_E^2}{8} - \frac{\pi^2}{48} \right)\epsilon^2 + \mathcal{O}(\epsilon^3), \quad (2.79a)$$

$$\left( \frac{s}{4\pi\mu^2} \right)^{\frac{\epsilon}{2}} = e^{\ln\left(\frac{s}{4\pi\mu^2}\right)^{\frac{\epsilon}{2}}} = e^{\frac{\epsilon}{2}\ln\left(\frac{s}{4\pi\mu^2}\right)} = 1 + \frac{\epsilon}{2}\ln\left(\frac{s}{4\pi\mu^2}\right) + \mathcal{O}(\epsilon^2), \quad (2.79b)$$

where  $\gamma_E$  is Euler's constant. Finally then we have:

$$\sigma_v = \frac{2\alpha_s}{3\pi} \sigma_0 \left[ -\frac{8}{\epsilon^2} + \frac{1}{\epsilon}(6 - 4\gamma_E - 4L) + \gamma_E(3 - \gamma_E) \right. \quad (2.80)$$

$$\left. - 8 + \frac{\pi^2}{6} + \pi^2 - L^2 - (2\gamma_E - 3)L \right], \quad (2.81)$$

where  $L = \ln\left(\frac{s}{4\pi\mu^2}\right)$ . We can now see that regardless of our choice of gauge parameter,  $\xi$ , the result for the vertex correction is gauge independent. We also see that the parameter introduced to fix the coupling to be dimensionless appears in the final result; this is often the case when using dimensional regularisation and the modified minimal subtraction renormalisation scheme.

### The Real $\mathcal{O}(\alpha_s)$ Corrections

The real gluon emission diagrams which contribute to the  $\mathcal{O}(\alpha_s)$  corrections are figs. (2.3e) and (2.3f). These diagrams have an indistinguishable final state and so the real contribution will be of the form:

$$|\mathcal{A}_r|^2 = |\mathcal{A}_{left} + \mathcal{A}_{right}|^2 = |\mathcal{A}_{left}|^2 + |\mathcal{A}_{right}|^2 + 2\mathcal{A}_{left}\mathcal{A}_{right}^*, \quad (2.82)$$

where  $\mathcal{A}_{left}$  and  $\mathcal{A}_{right}$  refer to figs. (2.3e) and (2.3f) respectively and are given by:

$$\mathcal{A}_{left} = -Q e i g_s T_{ij}^a \bar{u}(k_2) \gamma^\mu \frac{\not{k}_1 + \not{k}}{(k_1 + k)^2} \gamma^\nu v(k_1) \epsilon_\nu \eta_\mu, \quad (2.83a)$$

$$\mathcal{A}_{right} = -Q e g_s T_{ij}^a \bar{u}(k_2) \gamma^\nu \frac{\not{k}_2 + \not{k}}{(k_2 + k)^2} \gamma^\mu v(k_1) \epsilon_\nu \eta_\mu. \quad (2.83b)$$

In the calculation of the terms of eq. (64) it will be useful to write the energy fractions for each particle as  $x_i = \frac{2E_i}{\sqrt{s}}$  (where  $i = 1$  is the external antiquark,  $i = 2$  is the antiquark and  $i = 3$  is the external gluon). In terms of these invariants the contraction of any two external particles simplifies to  $p_i \cdot p_j = \frac{1}{2}s(1 - x_k)$  which (since we are still assuming our quarks can be taken to be massless) gives a simple expression for the Mandelstam variables. Evaluating the  $|...|^2$  terms gives:

$$|\mathcal{A}_{left}|^2 = \frac{Q^2 e^2 g_s^2}{(k_1 + k)^4} \text{Tr}(T^a T^a) \text{Tr}(\not{k}_2 \gamma^\mu (\not{k}_1 + \not{k}) \gamma^\nu \not{k}_1 \gamma_\nu (\not{k}_1 + \not{k}) \gamma_\mu), \quad (2.84a)$$

$$|\mathcal{A}_{right}|^2 = \frac{Q^2 e^2 g_s^2}{(k_2 + k)^4} \text{Tr}(T^a T^a) \text{Tr}(\not{k}_2 \gamma^\nu (\not{k}_2 + \not{k}) \gamma^\mu \not{k}_2 \gamma_\mu (\not{k}_2 + \not{k}) \gamma_\nu), \quad (2.84b)$$

$$\mathcal{A}_{left} \mathcal{A}_{right}^* = \frac{Q^2 e^2 g_s^2}{(k_2 + k)^2 (k_1 + k)^2} \text{Tr}(T^a T^a) \text{Tr}(\not{k}_2 \gamma^\mu (\not{k}_1 + \not{k}) \gamma^\nu \not{k}_1 \gamma_\mu (\not{k}_2 + \not{k}) \gamma_\nu). \quad (2.84c)$$

Evaluating the trace terms in  $d$ -dimensions and rearranging in terms of the energy fractions gives:

$$|\mathcal{A}_{left}|^2 = 32 Q^2 e^2 g_s^2 \left(1 + \frac{\epsilon}{2}\right)^2 \frac{1 - x_1}{1 - x_2}, \quad (2.85a)$$

$$|\mathcal{A}_{right}|^2 = 32 Q^2 e^2 g_s^2 \left(1 + \frac{\epsilon}{2}\right)^2 \frac{1 - x_2}{1 - x_1}, \quad (2.85b)$$

$$2\mathcal{A}_{left} \mathcal{A}_{right}^* = 64 Q^2 e^2 g_s^2 \left(1 + \frac{\epsilon}{2}\right) \left(-\frac{\epsilon}{2} - 2 \frac{1 - x_3}{(1 - x_1)(1 - x_2)}\right). \quad (2.85c)$$

Summing these expressions gives:

$$|\mathcal{A}_r|^2 = 32 Q^2 e^2 g_s^2 \left[ \left(1 + \frac{\epsilon}{2}\right)^2 \frac{x_1^2 + x_2^2}{(1 - x_2)(1 - x_1)} + \epsilon \left(1 + \frac{\epsilon}{2}\right) \frac{2 - 2x_1 - 2x_2 + x_1 x_2}{(1 - x_2)(1 - x_1)} \right]. \quad (2.86)$$

As with the virtual contributions we are interested in the observable cross-section and so we must include the phase space factor for a three particle final state. Unlike the two particle phase space calculation here  $\int d^{3d-3} R_3$  cannot be integrated completely and we are left with a differential in terms of the energy fractions defined above:

$$\frac{d^2 R_3}{dx_1 dx_2} = \frac{s}{16(2\pi)^3} \left(\frac{s}{4\pi}\right)^\epsilon \frac{1}{\Gamma(2+\epsilon)} \left(\frac{1-z^2}{4}\right)^{\frac{\epsilon}{2}} x_1^\epsilon x_2^\epsilon, \quad (2.87)$$

where  $z = 1 - 2\frac{1-x_1-x_2}{x_1 x_2}$ . Combining eqs. (2.86) and (2.87) with a flux factor gives:

$$\frac{d^2 \sigma_r}{dx_1 dx_2} = \frac{2Q^2 e^2 g_s^2 F(x_1, x_2; \epsilon)}{\pi} \left(\frac{s}{4\pi}\right)^\epsilon \frac{1}{\Gamma(2+\epsilon)} \left(\frac{1-z^2}{4}\right)^{\frac{\epsilon}{2}} x_1^\epsilon x_2^\epsilon, \quad (2.88)$$

where we define  $F(x_1, x_2; \epsilon)$  as the algebraic factor in square brackets from eqn. (2.86). Switching to a dimensionless coupling and introducing  $\alpha_s$  as above:

$$\frac{d^2 \sigma_r}{dx_1 dx_2} = \frac{2Q^2 e^2 \alpha_s}{\pi} F(x_1, x_2; \epsilon) \left(\frac{s}{4\pi\mu^2}\right)^\epsilon \frac{1}{\Gamma(2+\epsilon)} \left(\frac{1-z^2}{4}\right)^{\frac{\epsilon}{2}} x_1^\epsilon x_2^\epsilon. \quad (2.89)$$

Comparing with the Born cross-section in eqn. (2.52) this can be written as:

$$\frac{d^2 \sigma_r}{dx_1 dx_2} = \frac{2\alpha_s \sigma_0}{3\pi} F(x_1, x_2; \epsilon) \left(\frac{s}{4\pi\mu^2}\right)^{\frac{\epsilon}{2}} \frac{1}{\Gamma(2+\frac{\epsilon}{2})} \left(\frac{1-z^2}{4}\right)^{\frac{\epsilon}{2}} x_1^\epsilon x_2^\epsilon. \quad (2.90)$$

Integrating over the allowed region of  $x_1$  and  $x_2$ :

$$\sigma_r = \frac{2\alpha_s \sigma_0}{3\pi} \left(\frac{s}{4\pi\mu^2}\right)^{\frac{\epsilon}{2}} \frac{1}{\Gamma(2+\frac{\epsilon}{2})} \int_0^1 dx_1 x_1^\epsilon \int_{1-x_1}^1 x_2^\epsilon \left(\frac{1-z^2}{4}\right)^{\frac{\epsilon}{2}} F(x_1, x_2; \epsilon). \quad (2.91)$$

We can define a change of variables  $x_2 = 1 - vx_1$  to decouple these integrals since:

$$\left(\frac{1-z^2}{4}\right)^{\frac{\epsilon}{2}} = \frac{x_1^2(1+v^2) - 2vx_1 + 1}{(1-x_1)x_1 v} + \epsilon \frac{x_1^2(1-v+v^2-x_1+1)}{(1-x_1)x_1 v} \quad (2.92)$$

$$+ \frac{\epsilon^2}{4} \frac{x_1^2(v^2-2v+1)+4(v-1)+1}{(1-x_1)xv}. \quad (2.93)$$

Substituting this into eqn. (2.91) and performing the  $x_1$  and  $v$  integrations gives:

$$\sigma_r = \frac{2\alpha_s \sigma_0}{3\pi} \left(\frac{s}{4\pi\mu^2}\right)^{\frac{\epsilon}{2}} \frac{\Gamma^2(1+\frac{\epsilon}{2})}{\Gamma(1+\frac{3\epsilon}{2})} \left[ \frac{8}{\epsilon^2} - \frac{6}{\epsilon} + \frac{19}{2} \right]. \quad (2.94)$$

Further expanding the Gamma functions gives:

$$\sigma_r = \frac{2\alpha_s}{3\pi} \sigma_0 \left[ \frac{8}{\epsilon^2} + \frac{1}{\epsilon} (-6 + 4\gamma_E + 4L) - \gamma_E(3 - \gamma_E) - \frac{57}{6} + \frac{7\pi^2}{6} + L^2 + (2\gamma_E - 3)L \right].$$

As in the case of the virtual corrections this is divergent in the limit  $\epsilon \rightarrow 0$  and exhibits a residual dependence on  $\mu$ .

### Cancellation of divergences

Having now found the vertex corrections and the real corrections up to  $\mathcal{O}(\epsilon^2)$  we can write the next-to-leading order cross-section by simply summing the two:

$$\sigma_{NLO} = \sigma_r + \sigma_v = \frac{\alpha_s}{\pi} \sigma_0. \quad (2.95)$$

So the total cross-section to next-to-leading order accuracy is:

$$\sigma = \sigma_0 \left( 1 + \frac{\alpha_s}{\pi} \right) + \mathcal{O}(\alpha_s^2). \quad (2.96)$$

The fact that the infrared divergences in both the real and virtual emission NLO diagrams cancel is an example of the KLN theorem which states that the Standard Model is completely free of infrared divergences on the whole and holds true at all orders.

### 2.7.3 Resumming Higher-Order Corrections

So as we have seen we can evaluate the truncated perturbative series and, provided we remember to include higher multiplicity diagrams which contribute in the soft limit, we will be left with a finite result which is invariant under gauge transformations.

It would seem then that this is the best way to proceed: we calculate as many corrections as we can and reason that all of the higher-order terms we have neglected are suppressed by powers of a small expansion parameter - the strong coupling,  $\alpha_s$ . If this is indeed the case we should see that each time we go to a higher-order in perturbation theory our series begins to converge. For example the effect of the NLO terms should be small with respect to the LO terms etc. It turns out that this is not true for all observables. To

motivate this we can give a schematic expansion of some variable we wish to calculate,  $\mathcal{O}$ :

$$\begin{aligned} \mathcal{O} = & \alpha_s (a_1 L^2 + b_1 L + c_1 1) + \\ & \alpha_s^2 (a_2 L^4 + b_2 L^3 + c_2 L^2 + d_2 L + e_2 1) + \\ & \alpha_s^3 (a_3 L^6 + b_3 L^5 + c_3 L^4 + d_3 L^3 + e_3 L^2 + f_3 L + g_3 1) + \dots, \end{aligned} \quad (2.97)$$

where  $L$  is some logarithm which may be large. A fixed-order scheme aims to exactly calculate some of the rows of equation (2.97) under the assumption that all subsequent lines are sufficiently suppressed. The problem with this picture is that the logarithms may be large enough that  $\alpha_s^n L^{2n} \sim \mathcal{O}(1)$ . In this case it would appear that it would be better for us to calculate the first column of the terms (called the ‘leading logarithmic’ or LL approximation) than to find the first *row* of terms (the LO approximation).

Fig. (2.4) shows how the ratio of the inclusive Higgs plus three jet cross-section to inclusive Higgs plus two jet cross-section varies as a function of the rapidity gap between the two leading jets in  $p_T$  [11]. The HEJ prediction is formally leading-logarithmic accurate (with leading-order matching for final states with up to three jets) while MCFM is formally next-to-leading order accurate. It is shown in chapter 3 that this rapidity gap is approximately equal to the logarithm,  $L$ , which we claim violates the key assumptions underlying fixed-order perturbation theory. Hence, as we move to large  $\Delta y(j_1, j_2)$  we increase the size of  $L$  in eqn. (2.97) and the terms neglected by the fixed-order scheme (but captured by a LL calculation) grow in size. The ratio of the inclusive  $(n+1)$ -jets to  $n$ -jet cross-sections is an interesting probe of the convergence of the QCD perturbative expansion since we are directly comparing the size of the NLO contributions to the LO terms. Fig. (2.4a) shows that at a centre-of-mass energy of 14 TeV (the energy scales soon to be achieved at the LHC) even at modest rapidity intervals of around 4.0 we see that half of all events contain extra radiation and when we pull the leading jets apart further in rapidity this increases to three quarters of all events.

Furthermore, figs. (2.4b) and (2.4c) show that as we increase the centre-of-mass energy to that of a potential hadronic future circular collider, 33 TeV and 100 TeV respectively, these enhanced higher-order terms become even more important - in the extreme case of dijets with a separation of  $\Delta y(j_1, j_2) \approx 8.0$  at a 100 TeV collider almost 90% of the cross-section is coming from the next-to-leading term in the perturbative series: this is clear evidence that is not generally sufficient to think of the expansion as being controlled by only the strong coupling constant,  $\alpha_s$ . We can also test this against existing; fig. (2.5) show the probability of extra jet activity in inclusive  $W^\pm$  plus dijets

as function of the rapidity gap between the two leading jets *in rapidity*,  $\Delta y(j_F, j_B)$ , taken from a very detailed study by the D $\emptyset$  collaboration [5] at the Tevatron experiment. This is equivalent to the ratio of the inclusive 3j and inclusive 2j cross-sections described in fig. (2.4). We observe the same behaviour that as we pull apart the dijets we see a marked rise in the probability of extra emissions but, more importantly, we see that the data show this strongly increasing trend too.

The remaining chapters of this thesis will focus on deriving a formalism for calculating these higher-order corrections in order to describe physics observed at the LHC.

## 2.8 Spinor-Helicity Notation

We now move towards the more mechanical aspects of this thesis to discuss a technique which eases calculations. In chapters 3 and 4 we choose to work in the spinor-helicity formalism [34, 36]. This is a very convenient choice of notation which allows us to quickly evaluate complicated strings of products of Dirac spinors and Dirac matrices which would otherwise be troublesome to work with.

We begin by looking at the case of massless particles; this is relevant for high energy QCD since gluons are massless and the quark masses are often negligible compared to the energy scale in a typical scattering process. The massless Dirac equation can be solved by using a plane-wave expansion with some momentum dependent coefficient functions,  $u(p)$  and  $v(p)$  where  $p$  is the momentum carried by the particle and must satisfy the on-shell condition  $p^2 = 0$ . This expansion gives the following equations:

$$\begin{aligned} (\not{p} + m)u(p) &= 0, \\ (\not{p} - m)v(p) &= 0. \end{aligned} \tag{2.98}$$

Each of these equations has two independent solutions which we identify as the helicity states,  $u^\pm(p)$  and  $v^\pm(p)$ . We use the following notation for these spinors:

$$u^\pm(p) = | p\pm \rangle, \quad \overline{u^\pm(p)} = \langle p\pm | . \tag{2.99}$$

In the massless limit we also have the following relation  $u^\pm(p) = v^\mp(p)$  which allows us to use the same notation for both quarks and anti-quarks. Often the helicity information will be suppressed in the interests in being concise. We also define the following spinor-brackets:

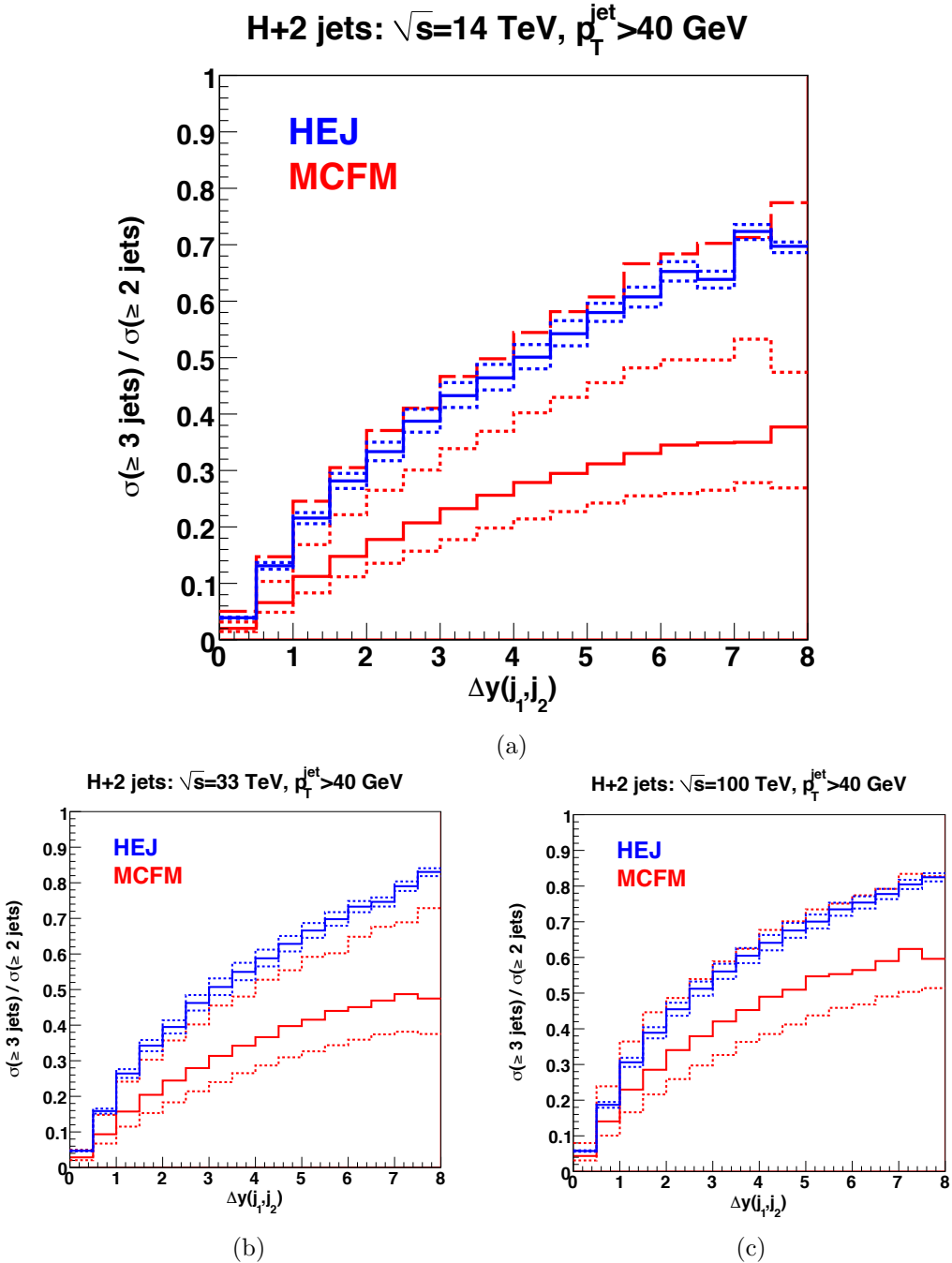


Figure 2.4: The ratio of the inclusive Higgs plus three jet cross-section to inclusive Higgs plus two jet cross-section shown for centre-of-mass energies of 14TeV (similar to the current LHC), 33TeV and 100TeV (possible energy scales for a hadronic future circular collider).

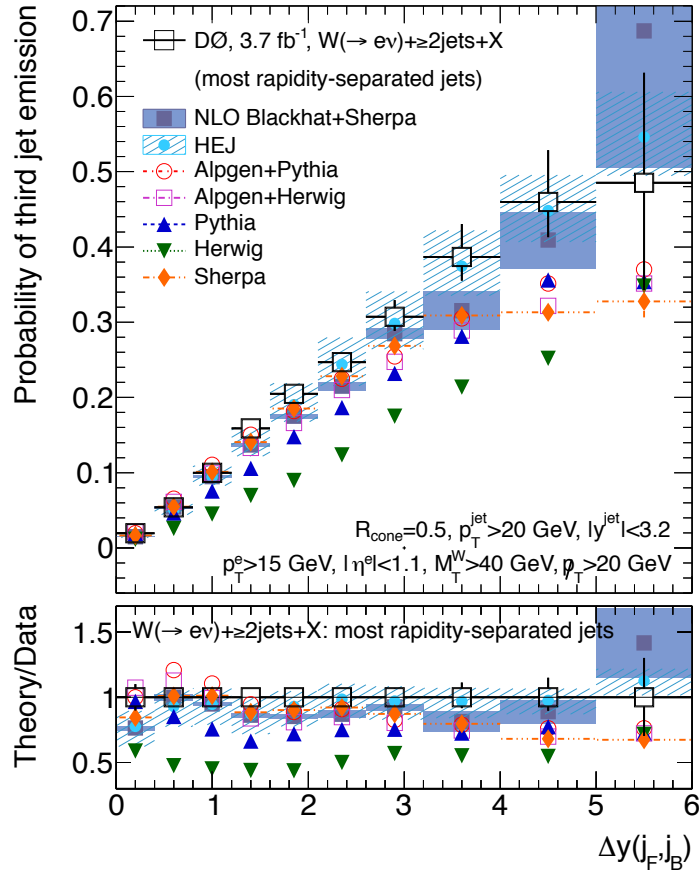


Figure 2.5: The probability of a third jet emission in  $W^\pm$  plus inclusive dijets as a function of the rapidity gap between the two leading jets in rapidity at the D0 experiment at the Tevatron experiment. The data are compared to a number of generators including the leading logarithmic accurate HEJ and the NLO accurate Blackhat+Sherpa.

$$\langle pk \rangle = \langle p- | k+ \rangle, \quad [pk] = \langle p+ | k- \rangle. \quad (2.100)$$

In this language we have the following useful identities:

$$\begin{aligned} \langle ij \rangle [ij] &= s_{ij} & \langle i\pm | \gamma^\mu | i\pm \rangle &= 2k_i^\mu \\ \langle ij \rangle &= -\langle ji \rangle & [ij] &= -[ji] \\ \langle i\pm | \gamma^\mu | j\pm \rangle \langle k\pm | \gamma_\mu | l\pm \rangle &= 2[ik]\langle lj \rangle & \langle k\pm | \gamma^\mu | l\pm \rangle &= \langle l\mp | \gamma^\mu | k\mp \rangle \\ \langle ij \rangle \langle kl \rangle &= \langle ik \rangle \langle lj \rangle + \langle il \rangle \langle kj \rangle & [ij][kl] &= [ik][jl] + [il][kj] \\ \langle i+ | k| j+ \rangle &= [ik]\langle kj \rangle & \langle i- | k| j- \rangle &= \langle ik \rangle [kj] \end{aligned}$$

In the calculations here we use the following convention for spinors. We express the parton momenta in terms of light-cone coordinates where  $p^\pm = E \pm p_z$  and  $p_\perp = p_x + ip_y$ . For outgoing positive (negative) helicity partons,  $u^+(p)$  ( $u^-(p)$ ) we have:

$$u^+(p) = \begin{pmatrix} \sqrt{p^+} \\ \sqrt{p^-} \frac{p_\perp}{|p_\perp|} \\ 0 \\ 0 \end{pmatrix} \quad u^+(p) = \begin{pmatrix} 0 \\ 0 \\ \sqrt{p^-} \frac{p_\perp^*}{|p_\perp|} \\ -\sqrt{p^+} \end{pmatrix} \quad (2.101)$$

respectively. While for incoming positive (negative) helicity partons moving in the positive  $z$  direction,  $u^+(p)$  ( $u^-(p)$ ) we have:

$$u^+(p) = \begin{pmatrix} \sqrt{p^+} \\ 0 \\ 0 \\ 0 \end{pmatrix} \quad u^-(p) = \begin{pmatrix} 0 \\ 0 \\ 0 \\ -\sqrt{p^+} \end{pmatrix} \quad (2.102)$$

respectively. Lastly for incoming positive (negative) helicity partons moving in the negative  $z$  direction,  $u^+(p)$  ( $u^-(p)$ ) we have:

$$u^+(p) = \begin{pmatrix} 0 \\ -\sqrt{p^-} \\ 0 \\ 0 \end{pmatrix} \quad u^-(p) = \begin{pmatrix} 0 \\ 0 \\ -\sqrt{p^-} \\ 0 \end{pmatrix}. \quad (2.103)$$

We also use following form for the Dirac matrices:

$$\gamma^0 = \begin{pmatrix} 0 & 0 & 1 & 0 \\ 0 & 0 & 0 & 1 \\ 1 & 0 & 0 & 0 \\ 0 & 1 & 0 & 0 \end{pmatrix} \quad \gamma^1 = \begin{pmatrix} 0 & 0 & 0 & -1 \\ 0 & 0 & -1 & 0 \\ 0 & 1 & 0 & 0 \\ 1 & 0 & 0 & 0 \end{pmatrix}. \quad (2.104)$$

$$\gamma^2 = \begin{pmatrix} 0 & 0 & 0 & i \\ 0 & 0 & -i & 0 \\ 0 & -i & 0 & 0 \\ i & 0 & 0 & 0 \end{pmatrix} \quad \gamma^3 = \begin{pmatrix} 0 & 0 & -1 & 0 \\ 0 & 0 & 0 & 1 \\ 1 & 0 & 0 & 0 \\ 0 & -1 & 0 & 0 \end{pmatrix}. \quad (2.105)$$

### 2.8.1 Spinor-Helicity Calculations with Massive Partons

To do calculations with massive partons using the spinor-helicity formalism we must be very careful since all of our favourite identities and tricks rely on the spinor brackets,  $|i\rangle$ , representing massless partons with  $p_i^2 = 0$ . We begin by defining ‘fundamental spinors’ [25] which we can use to build more general spinors and go from there. For some  $k_0, k_1$  satisfying  $k_0^2 = 0, k_1^2 = -1$  and  $k_0 \cdot k_1 = 0$  we can define positive and negative helicity spinors as follows:

$$u_-(k_0)\bar{u}_-(k_0) \equiv \omega_- \not{k}_0 \quad (2.106a)$$

$$u_+(k_0) \equiv \not{k}_1 u_-(k_0), \quad (2.106b)$$

where  $\omega_\lambda = \frac{1}{2}(1 + \lambda\gamma^5)$  is the helicity projection operator. In order for these to be valid spinors they must satisfy the following completeness relations:

$$\sum_{\lambda} u_{\lambda}(p) \bar{u}_{\lambda}(p) = \not{p} + m \quad (2.107a)$$

$$u_{\lambda}(p) \bar{u}_{\lambda}(p) = \omega_{\lambda} \not{p} \quad (2.107b)$$

The spinors in eqn. (2.106) can easily be shown to satisfy these as follows:

$$\begin{aligned} u_{-}(k_0) \bar{u}_{-}(k_0) + u_{+}(k_0) \bar{u}_{+}(k_0) &= \omega_{-} \not{k}_0 + \not{k}_1 u_{-}(k_0) \bar{u}_{-}(k_0) \not{k}_1, \\ &= \omega_{-} \not{k}_0 + \not{k}_1 \omega_{-} \not{k}_0 \not{k}_1, \\ &= \omega_{-} \not{k}_0 + \frac{1}{2} \gamma^{\mu} k_{1\mu} (1 - \gamma^5) \gamma^{\nu} k_{0\nu} \gamma^{\sigma} k_{1\sigma}, \\ &= \omega_{-} \not{k}_0 + \frac{1}{2} k_{1\mu} k_{0\nu} k_{1\sigma} (\gamma^{\mu} \gamma^{\nu} \gamma^{\sigma} - \gamma^{\mu} \gamma^5 \gamma^{\nu} \gamma^{\sigma}), \\ &= \omega_{-} \not{k}_0 + \frac{1}{2} k_{1\mu} k_{0\nu} k_{1\sigma} (2\gamma^{\mu} g^{\nu\sigma} - \gamma^{\mu} \gamma^{\sigma} \gamma^{\nu} + 2\gamma^5 \gamma^{\mu} g^{\nu\sigma} - \gamma^5 \gamma^{\mu} \gamma^{\sigma} \gamma^{\nu}), \\ &= \omega_{-} \not{k}_0 + k_{1\mu} k_{0\nu} k_{1\sigma} \omega_{+} \gamma^{\mu} (2g^{\nu\sigma} - \gamma^{\sigma} \gamma^{\nu}), \\ &= \omega_{-} \not{k}_0 + 2 \not{k}_1 k_0 \cdot k_1 - \omega_{+} \not{k}_1 \not{k}_1 \not{k}_0, \\ &= \omega_{-} \not{k}_0 + \omega_{+} \not{k}_0, \end{aligned}$$

where we have used  $\gamma^{\mu}, \gamma^{\mu} = 2g^{\mu\nu}, \gamma^{\mu}, \gamma^5 = 0$  and  $\not{k}_1 \not{k}_1 = k_1^2 = 0$ . This proves the property of eqn. (2.107) and inserting the definition of  $\omega_{\lambda}$  gives:

$$\begin{aligned} u_{-}(k_0) \bar{u}_{-}(k_0) + u_{+}(k_0) \bar{u}_{+}(k_0) &= \frac{1}{2} (1 - \gamma^5) \not{k}_0 + (1 + \gamma^5) \not{k}_0, \\ &= \not{k}_0, \end{aligned}$$

which is eqn. (2.107) for a massless particle.

We can use these fundamental spinors to form spinors for any given momenta,  $p$  (which has  $p^2 = 0$ ), as follows:

$$u_{\lambda}(p) = \not{p} u_{-\lambda}(k_0) \frac{1}{\sqrt{2p \cdot k_0}}, \quad (2.110)$$

provided we don't have  $p \cdot k_0 = 0$ . Once again it is easy to show that this spinor satisfies the necessary conditions, for example:

$$\begin{aligned}
 u_\lambda(p)\bar{u}_\lambda(p) &= \frac{1}{2p \cdot k_0} \not{p} u_{-\lambda}(k_0) \bar{u}_{-\lambda}(p) \not{p}, \\
 &= \frac{1}{2p \cdot k_0} \not{p} \omega_{-\lambda} \not{k}_0 \not{p}, \\
 &= \frac{1}{4p \cdot k_0} \not{p} (1 - \lambda \gamma^5) \not{k}_0 \not{p}, \\
 &= \frac{1}{2p \cdot k_0} p_\mu k_{0\nu} p_\sigma \omega_\lambda \gamma^\mu (2g^{\nu\sigma} - \gamma^\sigma \gamma^\nu), \\
 &= \frac{1}{2p \cdot k_0} \omega_\lambda (2\not{p} p \cdot k_0 - \not{p} \not{p} \not{k}), \\
 &= \omega_\lambda \not{p}.
 \end{aligned}$$

So far so good. This can also be generalised so that we can build massive spinors from our fundamental ones. We can use

$$u(q, s) = \frac{1}{\sqrt{2q \cdot k}} (\not{q} + m) u_-(k) \quad (2.112)$$

to describe a quark with spin 4-vector  $s$ , mass  $m$  and momentum  $q$ . To confirm this we go through the same procedure as above:

$$\begin{aligned}
 u_\lambda(p, s)\bar{u}_\lambda(p, s) &= \frac{1}{2q \cdot k_0} (\not{q} + m) u_-(k_0) \bar{u}_-(q) (\not{q} + m), \\
 &= \frac{1}{2q \cdot k_0} (\not{q} + m) \omega_- \not{k}_0 (\not{q} + m), \\
 &= \frac{1}{4q \cdot k_0} (\not{q} + m) (1 - \gamma^5) \not{k}_0 (\not{q} + m), \\
 &= \frac{1}{4q \cdot k_0} [ (\not{q} \not{k}_0 \not{q} + m \not{k} \not{q} + m \not{q} \not{k}_0 + m^2 \not{k}) - \gamma^5 (\not{q} \not{k} \not{q} - m \not{k} \not{q} + m \not{q} \not{k}_0 - m^2 \not{k}) ], \\
 &= \frac{1}{2} \left( \not{q} + m - \gamma^5 \not{q} - m \gamma^5 + \frac{m \gamma^5 \not{k} \not{q}}{k \cdot q} + \frac{\gamma^5 m^2 \not{k}}{k \cdot q} \right), \\
 &= \frac{1}{2} \left( 1 + \left( \frac{1}{m} \not{q} - \frac{m}{q \cdot k} \not{k} \right) \gamma^5 \right) (\not{q} + m), \\
 &= \frac{1}{2} (1 + \not{q} \gamma^5) (\not{q} + m),
 \end{aligned}$$

where the last line defines the spin vector  $s = \frac{1}{m}q - \frac{m}{q \cdot k}k$ . Conjecturing a similar form for an antiquark spinor with spin 4-vector  $s$ , mass  $m$  and momentum  $q$ :

$$v(q, s) = \frac{1}{\sqrt{2q \cdot k}}(\not{q} - m)u_-(k) \quad (2.114)$$

leads to:

$$\begin{aligned} v_\lambda(p, s)\bar{v}_\lambda(p, s) &= \frac{1}{2q \cdot k_0}(\not{q} - m)u_-(k_0)\bar{u}_-(q)(\not{q} - m), \\ &= \frac{1}{2}\left((\not{q} - m) + \left(-\not{q} + m + \frac{m^2}{q \cdot k_0}\not{k}_0 - \frac{m}{q \cdot k_0}\not{q}\not{k}_0\right)\gamma^5\right), \\ &= \frac{1}{2}(1 + \not{\gamma}^5)(\not{q} - m). \end{aligned}$$

One last check that is worth performing is that these spinors actually satisfy the Dirac equation for both the quark and antiquark case. For the quark:

$$\begin{aligned} \not{q}u(q, s) &= \frac{1}{2q \cdot k_0}\not{q}(\not{q} + m)u_-(k_0), \\ &= \frac{1}{2q \cdot k_0}(m^2 + m\not{q})u_-(k_0). \end{aligned}$$

We now define some momentum  $\tilde{q}$  through the relation  $q = \tilde{q} + k_0$  such that  $\tilde{q}^2 = 0$  and  $q \cdot k = \tilde{q} \cdot k$ . Since  $q^2 = 2\tilde{q} \cdot k = m^2$  we may write

$$\begin{aligned} \not{q}u(q, s) &= \frac{1}{m}(m^2 + m\not{q})u_-(k_0), \\ &= (m + \not{q})u_-(k_0). \end{aligned}$$

We can now back substitute from the definition of  $u(q, s)$  in eq. (2.112) to get:

$$\not{q}u(q, s) = \sqrt{2q \cdot k}u(q, s), \\ = mu(q, s),$$

which is the Dirac equation for a quark. The result for antiquarks follows similarly. Now we have forms for massive quarks and antiquarks in terms of massless spinors we can use all of the spinor-helicity machinery to make our computations more efficient. Slightly more useful forms of equations (2.112) and (2.114) can be found by decomposing  $q$  into massless components once again:  $q = \tilde{q} + k$ . Then from eq. (2.112):

$$u(q, s) = \frac{1}{m}(\not{\tilde{q}} + \not{k} + m)u_-(k), \\ = \frac{1}{m}(|\tilde{q}^+\rangle\langle\tilde{q}^+|k^-\rangle + |\tilde{q}^-\rangle\langle\tilde{q}^-|k^-\rangle + |k^-\rangle\langle k^-|k^-\rangle + |k^-\rangle\langle k^-|k^-\rangle + m|k^-\rangle), \\ = \frac{[\tilde{q}k]}{m}|\tilde{q}^+\rangle + |k^-\rangle,$$

and similarly for the other helicities and the antiquarks:

$$u(q, -s) = \frac{\langle\tilde{q}k\rangle}{m}|\tilde{q}^-\rangle + |k^+\rangle, \quad (2.120a)$$

$$v(q, s) = \frac{[\tilde{q}k]}{m}|\tilde{q}^+\rangle - |k^-\rangle, \quad (2.120b)$$

$$v(q, -s) = \frac{\langle\tilde{q}k\rangle}{m}|\tilde{q}^-\rangle - |k^+\rangle \quad (2.120c)$$

## 2.9 Monte Carlo Techniques

### 2.9.1 One Dimensional Integration

Integrals are ubiquitous in every field of physics and particle physics is no different. We have already seen many examples where meaningful physical results can only be obtained after computing an integral two good examples of this are the convolution of the parton distribution functions with the partonic cross-section seen in section 2.5 and the more complex multi-dimensional integrals seen in section 2.7.2 the calculation

of the one-loop correction to quark-antiquark production.

For some of the integrals derived here it is not always feasible (and sometimes not even possible) to calculate them analytically. In these situations we must use a numerical approach to approximate the full result. Such approaches generally fall into one of two categories; quadrature or Monte-Carlo random sampling approaches. The most appropriate solution depends the integrand itself (and in particular our prior knowledge of the integrand) and the number of dimensions we are integrating over.

Here we briefly consider the one-dimensional case. Given an integral:

$$I = \int_a^b f(x)dx, \quad (2.121)$$

we can use well known results such as the Compound Simpson's Rule to approximate the integral by

$$I \approx \frac{h}{3} \sum_{i=0}^{N/2} (f(x_{2i-2}) + 4f(x_{2i-1}) + f(x_{2i})) + \mathcal{O}(N^{-4}), \quad (2.122)$$

where  $N$  is the number of times we have subdivided the integral range  $(a, b)$  and  $x_i = a + \frac{i(b-a)}{N}$  are the points at which we sample the integrand. The error quoted on eqn. (2.122) only shows the dependence on the sampling rate and it should be noted that there are other factors arising from the size of the domain of integration and on derivatives of the integrand,  $f(x)$ . The  $N^{-4}$  scaling of the error in this method makes it a good choice for numerics in one-dimension.

The Monte-Carlo approach to approximating eqn. (2.121) would be to (pseudo-)randomly select a series of  $N$  points,  $x_i$ , from within the domain of integration and then compute the integral as follows:

$$I \approx I_{MC} = \frac{b-a}{N} \sum_{i=0}^N f(x_i) + \mathcal{O}(N^{-\frac{1}{2}}). \quad (2.123)$$

Convergence of this result is assured by the weak law of large numbers (also known as Bernoulli's Theorem) which states that for a series of independent and identically distributed random variables,  $X_1, \dots, X_N$ , each with  $\mathbb{E}(X_i) = \mu$  the sample mean approaches the population mean as  $N \rightarrow \infty$ . That is,

$$\lim_{N \rightarrow \infty} \frac{X_1 + \cdots + X_N}{N} = \mu. \quad (2.124)$$

We can see this explicitly since the expectation of  $I_{MC}$  under the continuous probability density function  $p$  is:

$$\begin{aligned} \mathbb{E}_p[I_{MC}] &= \mathbb{E}_p \left[ \frac{b-a}{N} \sum_{i=0}^N f(x_i) \right] \\ &= \frac{b-a}{N} \sum_{i=0}^N \mathbb{E}_p [f(x_i)] \\ &= \frac{b-a}{N} \sum_{i=0}^N \int_{-\infty}^{+\infty} f(x)p(x)dx \end{aligned}$$

where  $p(x) = \frac{1}{b-a}$  is the uniform probability distribution for  $x \in (a, b)$ . Hence,

$$\begin{aligned} \mathbb{E}_p[I_{MC}] &= \frac{b-a}{N} \frac{1}{b-a} \sum_{i=0}^N \int_a^b f(x)dx \\ &= \int_a^b f(x)dx = I. \end{aligned}$$

Since the convergence of the Monte-Carlo approximation clearly scales significantly worse than the case for quadrature it would seem that it is not worth considering and, indeed, for a single dimension it is not. However, the picture changes when we consider integrals in dimension  $d \geq 2$ .

### 2.9.2 Higher Dimensional Integration

In the case of higher dimensional integrals e.g.

$$I = \int_{[a,b]} f(\vec{x})d\vec{x} = \int_{x_1=a_1}^{x_1=b_1} \cdots \int_{x_n=a_n}^{x_n=b_n} f(x_1, \dots, x_n)dx_1 \dots dx_n, \quad (2.125)$$

we can still look to generalisations of the quadrature methods touched on in section 2.9.1 however the convergence of these methods is less favourable. Quadrature methods have errors which scale with the number of dimensions we are integrating over, e.g.  $\mathcal{O}(N^{-\frac{4}{d}})$  for the compound Simpson's rule. We can argue this intuitively since if we have  $N$  points in one dimension to get an error which scales as  $\mathcal{O}(N^{-4})$  then in two

dimensions we would require  $N^2$  to achieve the same density of samplings and hence  $N^2 \sim \mathcal{O}(N^{-4}) \implies N^2 \sim \mathcal{O}(N^{-\frac{4}{2}})$  and more generally  $\mathcal{O}(N^{-\frac{4}{d}})$ .

By comparison the error of a Monte Carlo approximation stays fixed at  $\mathcal{O}(N^{-\frac{1}{2}})$  regardless of the number of dimensions in the integrals. We are spared from this so-called ‘curse of dimensionality’ by the Central Limit Theorem which states that for a sequence of independent and identically distributed random variables  $X_1, \dots, X_N$  each with variance  $\sigma^2$  we have:

$$\frac{X_1 + \dots + X_N - N\mathbb{E}(X_1)}{\sqrt{N}\sigma} \xrightarrow{\lim N \rightarrow \infty} \mathcal{N}(0, 1), \quad (2.126)$$

where  $\mathcal{N}(0, 1)$  is the normal distribution with mean zero and variance 1. Then using the additive and multiplicative scaling of the normal distribution we see that:

$$\sum_{i=1}^N X_i \xrightarrow{\lim N \rightarrow \infty} \mathcal{N}\left(\mu, \frac{\sigma^2}{N}\right), \quad (2.127)$$

where  $\mu$  is the mean of the variables  $X_i$ . The variance of a normal distribution is well known and we can use this to see that for a  $d$ -dimensional integral we can approximate our uncertainty as:

$$\int_{[a,b]} f(\vec{x}) d\vec{x} = V\langle f \rangle \pm V\sqrt{\frac{\langle f^2 \rangle - \langle f \rangle^2}{N}} \quad (2.128)$$

$$\equiv V\langle f \rangle \pm V\frac{\sigma_{MC}}{\sqrt{N}}, \quad (2.129)$$

where  $V$  is the volume of the domain of integration,  $\langle f \rangle = \sum_i f(x_i)$  and  $\langle f^2 \rangle = \sum_i f(x_i)^2$ .

### 2.9.3 Variation Reduction Techniques

In equation (2.129) we saw that the error estimate of a Monte Carlo approximation depends not only on the number of points sampled,  $N$ , but also on  $\sigma_{MC}$ . We can try to reduce  $\sigma_{MC}$  by reducing how ‘variable’ the integrand is over the domain of integration, for instance in the extreme example where our integrand is  $f(x) = f_0$ , a constant, it is clear that one Monte Carlo sample is sufficient to compute the integral exactly. Previously when computing  $\mathbb{E}_p[I_{MC}]$  we used a uniform probability density function

but we are free to use any distribution we like to perform the integration. This can be seen since:

$$\begin{aligned}\mathbb{E}_p[I_{MC}] &= \int f(x)p(x)dx, \\ &= \int \frac{f(x)p(x)q(x)}{q(x)}, \\ &= \mathbb{E}_q\left[\frac{I_{MC}p(x)}{q(x)}\right],\end{aligned}$$

where  $q(x)$  is our ‘importance sampling’ distribution. For example let us consider the integral

$$I = 150 \int_0^{\frac{1}{2}} x^2 \arcsin x^2 dx. \quad (2.130)$$

The integrand of eqn. (2.130) is shown in fig. (2.6) along with two potential choices of density functions. The uniform distribution (shown in red) will sample the integrand equally across the domain however it is clear from looking at the functional form of eqn. (2.130) that that isn’t the most efficient approach since it is strongly peaked towards the right hand side of the domain. Hence that is where the largest contribution to the Monte Carlo sum will come from. However if we sample the modified integrand using pseudo-random numbers generated from a distribution proportional to  $x^4$  (shown in green in fig. (2.6)) we can reduce the variance of our approximation significantly. Tab. 2.2 shows how the approximation improves as we vary the number of samples,  $N$ , for the two cases of  $q \sim \mathcal{U}(0, 0.5)$  and  $q \sim x^4$ .

$N$	$q \sim \mathcal{U}(0, 0.5)$		$q \sim x^4$	
	Approximation	Error	Approximation	Error
$10^1$	$0.5111428 \pm 1.5932607$	0.4318912	$0.9424279 \pm 1.6817093$	0.0006061
$10^2$	$0.9098668 \pm 2.0212007$	0.0331672	$0.9429298 \pm 2.6653523$	0.0001042
$10^3$	$0.9337252 \pm 2.0040391$	0.0093088	$0.9431454 \pm 0.8430513$	$8.936 \times 10^{-5}$
$10^4$	$0.9456974 \pm 2.0415918$	0.0026633	$0.9430386 \pm 0.2665659$	$4.504 \times 10^{-6}$
$10^5$	$0.9438040 \pm 2.0222993$	0.0007699	$0.9430241 \pm 0.0842942$	$2.848 \times 10^{-6}$

Table 2.2: The Monte-Carlo approximation to equation (2.130) as we vary the number of sampled points,  $N$ , shown in the naïve sampling case and in the importance sampled case.

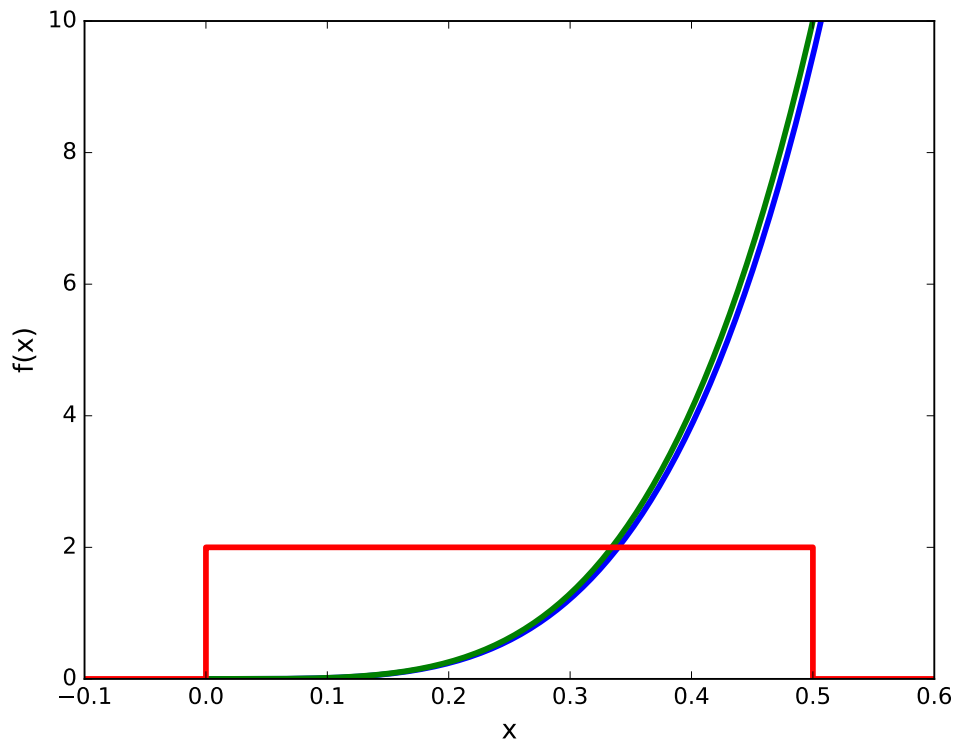


Figure 2.6: A simple importance sampling example (see equation (2.130)). The integrand,  $f(x)$ , is shown in blue, the importance sampling distribution is shown in green and, for comparison, the uniform probability density function used in the naïve case of no importance sampling is also shown (in red).

Tab. 2.2 clearly shows the value of an importance sampling approach converges to the correct result much faster than when we sample uniformly. Of course this tactic relies on us having some prior knowledge of the behaviour of our integrand in order to select the correct probability density function to use which, in more complicated examples is not always possible<sup>3</sup>. A more realistic, and relevant, example of importance sampling comes from the cross-section for the production of a  $Z^0$  boson in association with dijets. The matrix element squared for such a process will have following form upon factoring out the  $Z^0$  propagator squared:

$$|\mathcal{M}_{Z^0+jj}|^2 \sim \left| \frac{1}{p_Z^2 - M_Z^2 + i\Gamma_Z M_Z} \right|^2 \times f(\text{QCD, EW}) \times g(\text{Kinematic}), \quad (2.131)$$

where  $p_Z$  is the momentum carried by the  $Z^0$  boson,  $M_Z$  is its mass,  $\Gamma_Z$  is its width and  $f(\text{QCD, EW})$  will contain all of the coupling information and  $g(\text{Kinematic})$  encodes the remainder of the matrix element. When using a Monte-Carlo approach to generate events of this kind we can use the schematic form of eqn. (2.131) to *a priori* select an appropriate probability density function to sample from. Fig. (2.7) shows the squared  $Z^0$  propagator. Obvious comparisons with fig. (2.6) can be drawn in the sense that were we to generate events with a uniform spread of values for  $p_Z^2$  we would end with a very slow rate of convergence by oversampling areas where the integrand is very small and slowly varying.

Another good example of importance sampling is found in how we sample the incoming partons in our simulations. Simple momentum conservation considerations lead us to values for the Bjorken scaling variables of our incoming partons,  $x_a$  and  $x_b$ , and we can use these to intelligently sample the available partons. The naïve way to perform the sum over all possible incoming states would be to uniformly choose a random number corresponding to one of the light quarks, one the light anti-quarks or to a gluon<sup>4</sup>. We can, however, do better than this by using what we know about how the parton density functions vary with  $x_{a/b}$  - fig. (2.8) shows this behaviour as measured by the HERA experiment. By choosing to randomly sample then incoming parton types according to the relative values for the parton density functions we can, once again, reduce the variance of our numerical integrations as much as possible.

---

<sup>3</sup>More novel approaches whereby the sampling distribution is modified to improve convergence as the Monte-Carlo iterations are calculated, such as the **VEGAS** algorithm, exist but they will not be discussed here.

<sup>4</sup>Here we mean all except the top and anti-top. The parton density functions for these are not available and, even if they were, they would be small enough that we could safely ignore their contribution to cross-sections.

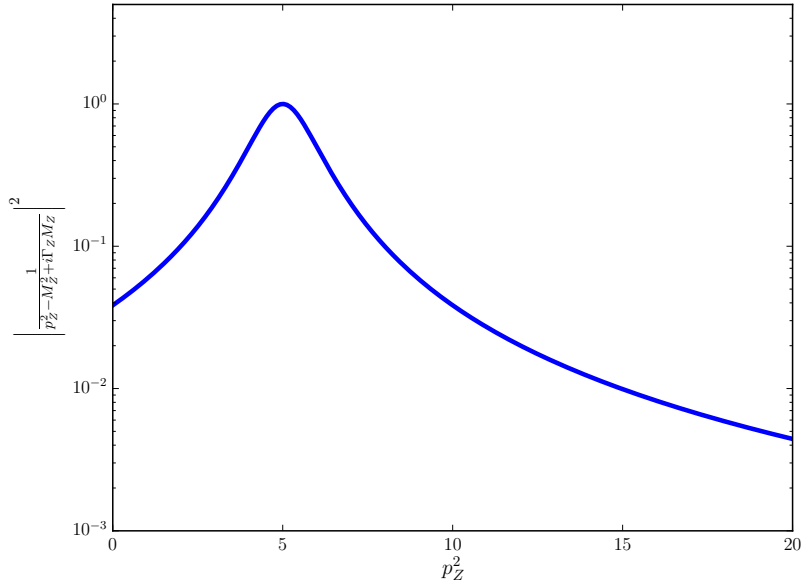


Figure 2.7: The absolute value squared of the  $Z^0$  propagator for a range of values of the invariant mass squared of the  $Z^0$ ,  $p_Z^2$ . We see that, as expected, it is strongly peaked at the  $Z^0$  mass and, as such, is an ideal candidate for using importance sampling.

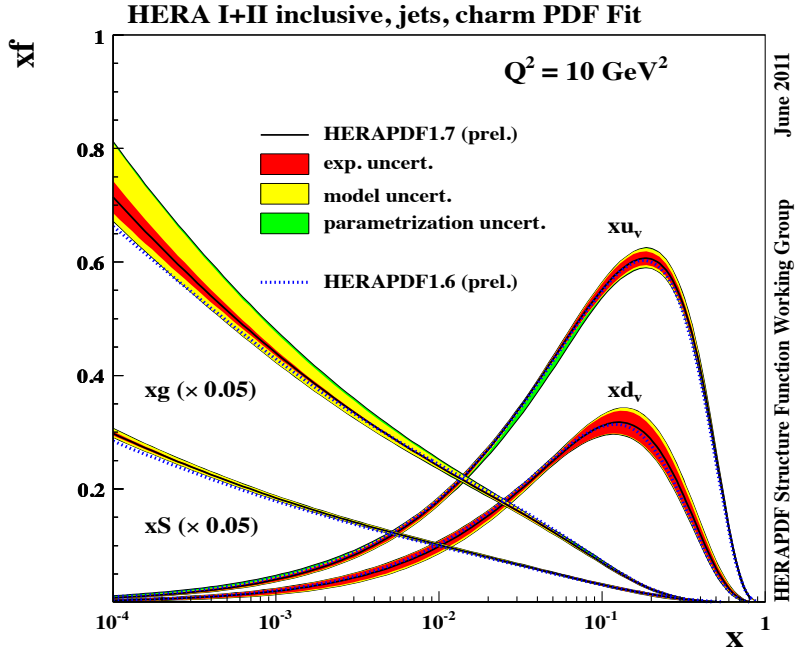


Figure 2.8: Recent parton distribution function fits from the HERA experiment. The observed variation in  $f(x_{a/b}, Q^2)$ , especially at high  $x_{a/b}$ , can be used to reduce the variance of a Monte Carlo approach to computing eqn (2.42) by using an importance sampling approach



# Chapter 3

## High Energy QCD

In this chapter we look in detail at the ‘High Energy’ limit of QCD. We begin by defining this limit and looking at how basic  $2 \rightarrow 2$  scattering behaves at leading order and next-to-leading order in  $\alpha_s$  before discussing how, in this limit, scattering amplitudes may be conveniently expressed as a contraction between two vector ‘current’ terms. Finally, we show how we may adorn  $2 \rightarrow 2$  matrix elements with real and virtual corrections by way of an effective vertex for real emissions and the Lipatov ansatz respectively.

### 3.1 The ‘High Energy’ limit

The ‘High Energy’ limit of QCD, also referred to as the Multi-Regge Kinematic (MRK) limit is defined in terms of the kinematics of the final state. We require a *strong rapidity ordering* of all outgoing radiation as well as all the emissions having *similar transverse momenta*. Mathematically this is:

$$y_1 \gg y_2 \gg \dots \gg y_n \text{ and } |p_{\perp 1}| \approx |p_{\perp 2}| \approx \dots \approx |p_{\perp(n-1)}|, \quad (3.1)$$

where we define the rapidity of a final state particle as

$$y = \frac{1}{2} \ln \frac{E + p_z}{E - p_z} \quad (3.2)$$

where  $E$  is the energy of particle and  $p_z$  is the  $z$  component of its momentum. We can state the criteria in eqn. (3.1) equivalently as:

$$s_{ij} \rightarrow \infty \text{ for all } i, j, \quad (3.3)$$

where  $s_{ij} = (p_i + p_j)^2$  is the invariant mass of a pair of outgoing partons. We sometimes parametrise the final states using pseudo-rapidity,  $\eta$ , rather than rapidity. Pseudo-rapidity is simply related to the angle of the outgoing state to the beam,  $\theta$ :

$$\eta = -\ln \tan \frac{\theta}{2}. \quad (3.4)$$

For massless states eqn. (3.2) and eqn. (3.4) are equivalent.

## 3.2 Mandelstam Variables in the High Energy Limit

The  $2 \rightarrow 2$  QCD scattering amplitudes can be expressed in terms of the well-known Mandelstam variables  $s$ ,  $t$  and  $u$ . Which, in terms of the momenta in the process, are given by:

$$\begin{aligned} s &= (p_a + p_b)^2, \\ t &= (p_a - p_1)^2, \\ u &= (p_b - p_2)^2, \end{aligned} \quad (3.5)$$

where  $p_a$ ,  $p_b$  are the incoming parton momenta and  $p_1$ ,  $p_2$  are the outgoing parton momenta. When working in the high energy limit it is convenient to re-express these in terms of the perpendicular momentum of the outgoing partons,  $p_\perp$ , and the difference in rapidity between the two final state partons,  $\Delta y$ . If we parametrise our outgoing states as

$$\begin{aligned} p_1 &= p_{\perp 1} (\cosh(y_1), \cos(\phi_1), \sin(\phi_1), \sinh(y_1)), \\ p_2 &= p_{\perp 2} (\cosh(y_2), \cos(\phi_2), \sin(\phi_2), \sinh(y_2)), \end{aligned} \quad (3.6)$$

then we can express eqs. (3.5) as follows

$$\begin{aligned} s &= 4p_\perp^2 \cosh^2 \frac{\Delta y}{2}, \\ t &= -2p_\perp^2 \cosh \frac{\Delta y}{2} e^{-\frac{\Delta y}{2}}, \\ u &= -2p_\perp^2 \cosh \frac{\Delta y}{2} e^{\frac{\Delta y}{2}}. \end{aligned} \tag{3.7}$$

In the limit of hard jets well separated in rapidity, i.e.  $\Delta y \rightarrow \infty$ , these are approximated by

$$\begin{aligned} s &= p_\perp^2 e^{\Delta y}, \\ t &= -p_\perp^2, \\ u &= -p_\perp^2 e^{\Delta y}. \end{aligned} \tag{3.8}$$

From eqn. (3.8) it is clear that the ‘hard, wide-angle jet’ limit, i.e.  $\Delta y \rightarrow \infty$ ,  $p_{i\perp} \rightarrow \infty$ , is equivalent to the High Energy limit since as  $\Delta y$  grows large  $s$  will grow exponentially while  $t$  will stay fixed. Rearranging for  $\Delta y$  in the above equations yields:

$$\Delta y = \ln \left( \frac{s}{-t} \right). \tag{3.9}$$

This is a useful result because it relates the simple kinematics of an event to a (potentially) large logarithm. It is already apparent from eqn. (3.9) that a final state with large rapidity gaps between jets will carry with it a large logarithm as seen in eqn. (2.97),  $L = \ln \left( \frac{s}{-t} \right)$ , and therefore we many need a more careful inspection of our perturbative expansion than the fixed-order approach.

### 3.3 $qQ$ -scattering at High Energy (at LO)

Here we begin with the simplest example; the case of  $qQ \rightarrow qQ$  for all negative helicity partons (the capital  $Q$  implies it is a different flavour to  $q$ ). There is only one diagram which contributes shown in fig. (3.1). Using the Feynman rules detailed in section 2.2 we can write the matrix element as:

$$i\mathcal{M}_{q^-Q^- \rightarrow q^-Q^-}^{\text{LO}} = ig_s^2 T_{1a}^d T_{2b}^d \frac{\bar{u}^-(p_1) \gamma^\mu u^-(p_a) \bar{u}^-(p_2) \gamma_\mu u^-(p_b)}{t} \quad (3.10)$$

$$= ig_s^2 T_{1a}^d T_{2b}^d \frac{\langle 1|\mu|a\rangle \cdot \langle 2|\mu|b\rangle}{t}, \quad (3.11)$$

where  $t = (p_a - p_1)^2$  and we have used the shorthand  $\bar{u}^-(p_i) \gamma^\mu u^-(p_j) = \langle i|\mu|j\rangle$  in the second line. Writing the contraction of these two ‘current’ terms in terms of light-cone coordinates we have:

$$i\mathcal{M}_{q^-Q^- \rightarrow q^-Q^-}^{\text{LO}} = ig_s^2 T_{1a}^d T_{2b}^d \frac{2\sqrt{p_a^- p_b^+}}{t} \left( \sqrt{p_1^+ p_2^-} e^{i\phi_2} + \sqrt{p_1^- p_2^+} e^{i\phi_1} \right), \quad (3.12)$$

where  $e^{i\phi_i} = \frac{p_{\perp i}}{|p_{\perp i}|}$ . We now approximate the kinematics in such a way that we may write eqn. (3.12) in a ‘factorised’ form once again. Specifically we consider that the scattering can be thought of as two partons glancing off one another. That is, we assume that  $p_1^+ \ll p_1^-$ ,  $p_2^- \ll p_2^+$  and that  $p_a$  ( $p_b$ ) is moving in the backwards (forward) direction. We can further assume that  $p_1^- \approx p_a^-$  and  $p_2^+ \approx p_b^+$  and with this we see that (3.12) becomes:

$$i\mathcal{M}_{q^-Q^- \rightarrow q^-Q^-}^{\text{LO}} = \frac{2s}{t} \left( g_s T_{1a}^d e^{i\phi_1} \right) \left( -ig_s T_{2b}^d \right), \quad (3.13)$$

which is ‘factorised’ in the sense that each scalar term in brackets depends only on one quark line; either on the  $p_{a/1}$  line or the  $p_{b/2}$  line. We see that the amplitude for  $qQ \rightarrow qQ$  is dominated by the  $s$  kinematic variable. We can express this as:

$$\mathcal{M}_{q^-Q^- \rightarrow q^-Q^-}^{\text{LO}} \sim s^{\alpha(t)}, \quad (3.14)$$

which is exactly the behaviour expected when a particle exchanged in the  $t$ -channel has ‘reggeised’ [20, 33, 65].  $\alpha(t)$  is the Regge trajectory and is equal to the intrinsic spin of the state exchanged. In our example we have a spin-one gluon exchanged and accordingly we can see from eqn. (3.13) that  $\alpha(t) = 1$  for  $qQ \rightarrow qQ$ .

It is also interesting to consider the same process but with a helicity structure  $q^-Q^+ \rightarrow q^-Q^+$ . The calculation proceeds similarly to the  $q^-Q^- \rightarrow q^-Q^-$  and when we write the result in terms of two vector ‘currents’ we get:

$$i\mathcal{M}_{q^-Q^+ \rightarrow q^-Q^+}^{\text{LO}} = ig_s^2 T_{1a}^d T_{2b}^d \frac{\langle 1|\mu|a\rangle \cdot \langle b|\mu|2\rangle}{t}, \quad (3.15)$$

which is still manifestly expressible as a contraction of two vector currents. The contraction can be written approximately as  $2[a2]\langle b1\rangle \sim 2[a2]\langle 2a\rangle = -2u$ . However when we continue on and take the High Energy limit of eqn. (3.15) we get:

$$\begin{aligned} i\mathcal{M}_{q^-Q^+ \rightarrow q^-Q^+}^{\text{LO}} &= ig_s^2 T_{1a}^d T_{2b}^d \frac{2}{t} \sqrt{p_a^- p_2^+} \sqrt{p_b^+ p_1^-} e^{i\phi_1} \\ &= ig_s^2 T_{1a}^d T_{2b}^d \frac{2s}{t} \end{aligned} \quad (3.16)$$

So we see that since in the full High Energy limit we have that  $s = -u$  exactly. Whereas when we leave the amplitude in terms of currents we are able to keep more of the physics by having the weaker constraint  $s \sim -u$ ; at the LHC  $t$  and  $k_\perp^2$  can often differ significantly and so the over-approximating the kinematics here would lead to a poor description of the data.

### 3.4 $qg$ scattering at High Energy

We now explore the more involved case of  $q^-g^+ \rightarrow q^-g^+$  scattering. At leading order this consists of three diagrams shown in fig. (3.2). We use the following gauge choice for the gluon polarisations:

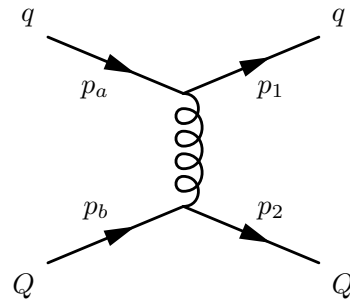


Figure 3.1: The only diagram which contributes to  $qQ \rightarrow qQ$  at leading order in  $\alpha_s$ .

$$\epsilon_{2\sigma}^{+*} = \frac{\langle b|\sigma|2\rangle}{\sqrt{2}\langle b2\rangle} \quad \epsilon_{2\sigma}^{-*} = -\frac{\langle b|\sigma|2\rangle}{\sqrt{2}[b2]} \quad (3.17)$$

$$\epsilon_{b\sigma}^+ = -\frac{\langle b|\sigma|2\rangle}{\sqrt{2}[2b]} \quad \epsilon_{2\sigma}^{-*} = -\frac{\langle b|\sigma|2\rangle}{\sqrt{2}\langle 2b\rangle} \quad (3.18)$$

For simplicity we choose to write everything in terms of negative helicity spinor-helicity brackets; to describe positive helicities we can use the transposition property of spinor-helicity brackets discussed in section 2.8.

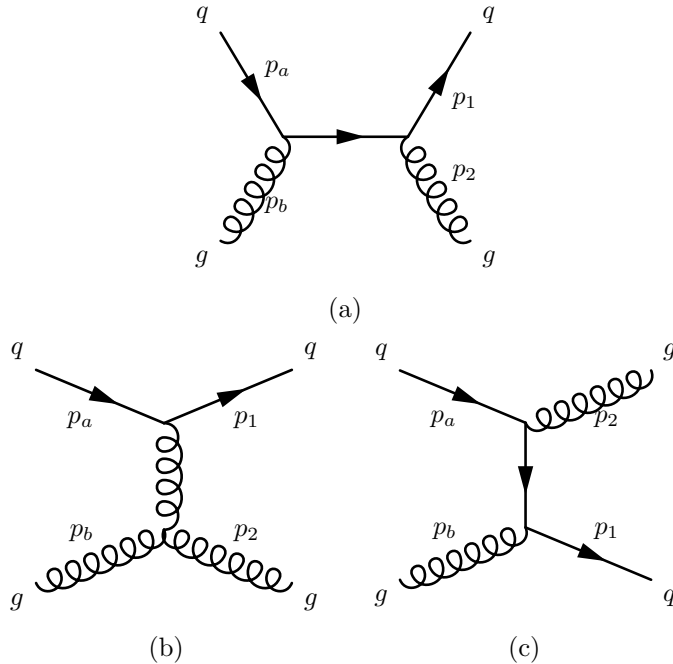


Figure 3.2: The  $s$ ,  $t$  and  $u$  channel diagrams contributing to  $q^- g^+ \rightarrow q^- g^+$  at leading order in  $\alpha_s$  in figures (3.2a), (3.2b) and (3.2c) respectively.

### 3.4.1 $s$ -channel

The matrix element for the  $s$ -diagram, shown in fig. (3.2a), is:

$$\mathcal{M}_{q^-g^+ \rightarrow q^-g^+, s}^{\text{LO}} = T_{ae}^b T_{e1}^2 \bar{u}^-(p_1) \left( -\frac{i g_s}{2} \gamma^\mu \right) \epsilon_\mu^{*+}(p_2) \frac{i(q+m)}{q^2 - m^2} \left( -\frac{i g_s}{2} \gamma^\nu \right) \epsilon_\nu^+(p_b) u^-(p_a), \quad (3.19)$$

$$= -\frac{g_s^2}{4q^2} \epsilon_{2\mu}^{*+} \epsilon_{b\nu}^+ \bar{u}_1^- \gamma^\mu q \gamma^\nu u_a^-, \quad (3.20)$$

where we have used  $q \gg mc$  for the high energy case (i.e. we treat the quarks as massless in the High Energy limit). The propagator has momentum  $q = p_a + p_b = p_1 + p_2$  and therefore:

$$\mathcal{M}_{q^-g^+ \rightarrow q^-g^+, s}^{\text{LO}} = -T_{ae}^b T_{e1}^2 \frac{g_s^2}{4q^2} \frac{\langle b|\mu|2\rangle}{\sqrt{2}\langle b2\rangle} \frac{\langle b|\nu|2\rangle}{\sqrt{2}[2b]} \bar{u}_1^- \gamma^\mu (\not{p}_a + \not{p}_b) \gamma^\nu u_a^-. \quad (3.21)$$

Now we can use the completeness relations for  $\not{p}_{a/b}$  and see that:

$$\mathcal{M}_{q^-g^+ \rightarrow q^-g^+, s}^{\text{LO}} = -T_{ae}^b T_{e1}^2 \frac{g_s^2}{4q^2 t} [2a] \langle ab \rangle \langle b|\mu|2\rangle \langle 1|\mu|a \rangle \quad (3.22)$$

Using  $q^2 = s_{ab} = \langle ab \rangle [ba]$  and  $t = \langle 2b \rangle [b2]$  we have:

$$\mathcal{M}_{q^-g^+ \rightarrow q^-g^+, s}^{\text{LO}} = -T_{ae}^b T_{e1}^2 \frac{g_s^2}{4} \frac{[2a]\langle ab \rangle}{\langle ab \rangle [ba] \langle 2b \rangle [b2]} \langle b|\mu|2\rangle \langle 1|\mu|a \rangle. \quad (3.23)$$

Now we must calculate the spinor products. We use the conventions for spinors outlined in the previous chapter. For example:

$$[2a] = \bar{u}_2^+ u_a^- = -\frac{\sqrt{p_a^+ p_2^-} p_2^\perp}{|p_2^\perp|}, \quad (3.24)$$

and after calculating the other brackets we see:

$$\mathcal{M}_{q^-g^+ \rightarrow q^-g^+, s}^{\text{LO}} = -T_{ae}^b T_{e1}^2 \frac{g_s^2}{4} \sqrt{\frac{p_2^-}{p_b^+}} \frac{1}{p_2^+ p_b^-} \frac{p_{2\perp}^*}{|p_{2\perp}|} \langle b|\mu|2\rangle \langle 1|\mu|a \rangle \quad (3.25)$$

Which can be simplified to give the final result:

$$\mathcal{M}_{q^-g^+ \rightarrow q^-g^+, s}^{\text{LO}} = -T_{ae}^b T_{e1}^2 \frac{g_s^2}{2\hat{t}} \sqrt{\frac{p_2^-}{p_b^-}} \frac{p_{2\perp}^*}{|p_{2\perp}|} \langle b|\mu|2\rangle \langle 1|\mu|a\rangle \quad (3.26)$$

### 3.4.2 *t*-channel

The matrix element for the *t*-channel diagram, shown in fig. (3.2b), is:

$$-i\mathcal{M}_{q^-g^+ \rightarrow q^-g^+, t}^{\text{LO}} = -T_{a1}^e f^{b2e} \bar{u}_1^- \left( -\frac{ig_s}{2} \gamma^\mu \right) \left( -\frac{ig_{\mu\nu}}{q^2} \right) u_a^- g_s \left( g_{\sigma\nu}(p_b - q)_\rho + g_{\nu\rho}(q + p_b)_\sigma - g_{\rho\sigma}(p_b + p_2)_\nu \right) \epsilon_{2+}^{\rho*} \epsilon_{b+}^\sigma \quad (3.27)$$

Now using  $q = p_2 - p_b$  and  $p_2 \cdot \epsilon_2 = p_b \cdot \epsilon_b = 0$ :

$$-i\mathcal{M}_{q^-g^+ \rightarrow q^-g^+, t}^{\text{LO}} = -T_{a1}^e f^{b2e} \frac{g_s^2}{2q^2 s_{2b}} (\bar{u}_1^- \gamma^\nu u_a^-) (\bar{u}_b^- \gamma^\rho u_2^-) (\bar{u}_b^- \gamma^\sigma u_2^-) \left( 2g_{\sigma\nu} p_{b\rho} + 2g_{\nu\rho} p_{2\sigma} - g_{\rho\sigma} (p_b + p_2)_\nu \right), \quad (3.28)$$

which cancels completely and therefore:

$$\mathcal{M}_{q^-g^+ \rightarrow q^-g^+, t}^{\text{LO}} = 0, \quad (3.29)$$

in this gauge.

### 3.4.3 *u*-channel

The matrix element for the *u*-diagram, shown in fig. (3.2b), is:

$$\begin{aligned} -i\mathcal{M}_{q^-g^+ \rightarrow q^-g^+, u}^{\text{LO}} &= T_{ae}^2 T_{e1}^b \bar{u}^-(p_1) \left( -\frac{ig_s}{2} \gamma^\mu \right) \frac{i(\not{q} + mc)}{q^2 - m^2 c^2} \left( -\frac{ig_s}{2} \gamma^\nu \right) u^-(p_a) \epsilon_\mu^{*+}(p_b) \epsilon_\nu^+(p_2) \\ \mathcal{A}_u &= \frac{g_s^2}{4q^2} \bar{u}_1^- \gamma^\mu \not{q} \gamma^\nu u_a^- \epsilon_{b\mu}^{*+} \epsilon_{2\nu}^* \\ &= \frac{g_s^2}{8q^2 s_{2b}} \langle b|\mu|2\rangle \langle b|\nu|1\rangle \bar{u}_1^- \gamma^\mu (\not{p}_a - \not{p}_2) \gamma^\nu u_a^- \end{aligned} \quad (3.30)$$

Where we have used  $q = p_a - p_2$ . By direct comparison with the procedure used for the  $s$ -channel we can see the result will be:

$$\mathcal{M}_{q^-g^+ \rightarrow q^-g^+, u}^{\text{LO}} = T_{ae}^2 T_{e1}^b \frac{g_s^2}{2\hat{t}} \sqrt{\frac{p_b^-}{p_2^-}} \frac{p_{2\perp}^*}{|p_{2\perp}|} \langle b|\mu|2\rangle \langle 1|\mu|a\rangle. \quad (3.31)$$

The total total matrix element is given by the sum of eqs. (3.26), (3.29) and (3.31) which is:

$$\mathcal{M}_{q^-g^+ \rightarrow q^-g^+}^{\text{LO}} \frac{g_s^2}{2} \frac{p_{2\perp}^*}{|p_{2\perp}|} \left( T_{ae}^2 T_{e1}^b \sqrt{\frac{p_b^-}{p_2^-}} - T_{ae}^b T_{e1}^2 \sqrt{\frac{p_b^-}{p_2^-}} \right) \frac{\langle b|\mu|2\rangle \langle 1|\mu|a\rangle}{\hat{t}}, \quad (3.32)$$

We also see that eqn. (3.32) has the same spinor-helicity brackets contracted as eqn. (3.11) and so the dominant behaviour of  $q^-g^+ \rightarrow q^-g^+$  in the high energy limit is  $\frac{s}{t}$ . In the High Energy limit we have  $p_b^- \sim p_2^-$  and so eqn. (3.32) could be simplified further to:

$$\mathcal{M}_{q^-g^+ \rightarrow q^-g^+}^{\text{LO}} = i \frac{g_s^2}{2} \frac{p_{2\perp}^*}{|p_{2\perp}|} f^{2bc} T_{a1}^c \frac{\langle b|\mu|2\rangle \langle 1|\mu|a\rangle}{\hat{t}}. \quad (3.33)$$

which is identical to the result found in the previous  $qQ \rightarrow qQ$  calculation (save for a phase which cancels at the amplitude squared level). Since the kinematics of which is exactly in the form of two ‘currents’ contracted as seen in section 3.3. We have:

$$\mathcal{M}_{qg \rightarrow qg}^{\text{LO}} = \frac{C_A}{C_f} \mathcal{M}_{qQ \rightarrow qQ}^{\text{LO}}, \quad (3.34)$$

in the High Energy limit. In practice we actually choose *not* to take the High Energy limit to obtain eqn. (3.33) so as to approximate as little as possible. Even without this extra approximation eqn. (3.32) is still exactly the form of a  $t$ -channel gluon exchange we saw in eqn. (3.11).

In section 3.9 we will return this result and the results of section 3.3 and discuss how, despite their simplicity, they can be used to construct very general approximate forms for matrix elements which could otherwise not be evaluated

### 3.5 $qQ$ -scattering at High Energy (at NLO)

Before we continue on to look at how we might add extra real and virtual emissions to high energy matrix elements we briefly look at higher order (in  $\alpha_s$ ) corrections to the process we studied in section 3.3. So far we have seen the leading order processes with a  $t$ -channel exchange are logarithmically enhanced but in eqn. (2.97) we sketched out a form for the perturbative expansion which also had logarithmically enhanced higher order corrections.

Here we continue on from section 3.3 and calculate the virtual diagrams which contribute a leading logarithm for  $qQ \rightarrow qQ$  at next-to-leading in  $\alpha_s$  [33, 65].

We might naïvely expect that the next-to-leading order diagrams with the maximal number of  $t$ -channel exchanges will give the greatest enhancement and, indeed, this turns out to be the case. These diagrams are shown for the case of  $qQ \rightarrow qQ$  in fig. (3.3). We can rule out the other virtual diagrams which contribute at this order since they will contain (anti-)quark propagators along the  $p_{a/1}$  or  $p_{b/2}$  lines and in the high energy limit these will lead to a suppression.

These diagrams in fig. (3.3) can be elegantly computed by employing the ‘Cutkosky rules’ which are used to relate two sub-diagrams to the imaginary part of a higher order diagram through the Optical theorem. This can be seen very quickly since the scattering matrix,  $S$ , must be unitary i.e.  $S^\dagger S = 1$ . If we write this instead in terms of the transition matrix,  $T$ , defined by  $S = 1 + iT$  then we immediately have that

$$-i(T - T^\dagger) = T^\dagger T. \quad (3.35)$$

The left hand side of which can be written as twice the imaginary part of  $T$ . If we now imagine that  $T$  represents the transition from some initial state  $|i\rangle$  to some final state  $|f\rangle$  then we can write this as:

$$2i\text{Im}(\langle i|T|f\rangle) = \sum_p \langle i|T^\dagger|p\rangle \langle p|T|f\rangle, \quad (3.36)$$

where we have inserted a sum over a complete set of states  $|p\rangle$ . Pictorially we ‘cut’ propagators by forcing them on-shell with delta functions and inserting a complete set of states.

For example the uncrossed amplitude in fig. (3.3a),  $\mathcal{M}_{qQ \rightarrow qQ}^{\text{NLO, II}}$ , may be expressed as a combination of two copies of the amplitude arising from fig. (3.1):

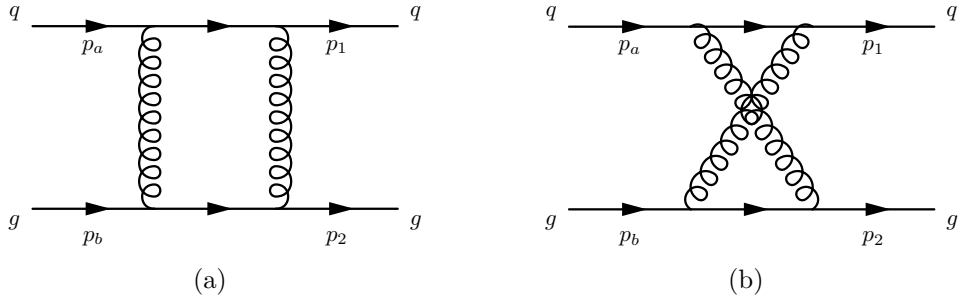


Figure 3.3: The leading logarithmic contributions to  $qg \rightarrow qg$  at NLO. The uncrossed diagram,  $\mathcal{M}_{qQ \rightarrow qQ}^{\text{NLO}, II}$ , shown in (a) exchanges two gluons in the  $t$  channel and the crossed diagram,  $\mathcal{M}_{qQ \rightarrow qQ}^{\text{NLO}, X}$ , case (b) exchanges two gluons in the  $u$  channel and is related to (a) (up to a colour factor) via a crossing symmetry

$$\mathcal{M}_{q^-Q^- \rightarrow q^-Q^-}^{\text{LO}} = -g_s^2 T_{1a}^d T_{2b}^d \frac{\langle 1|\mu|a\rangle \cdot \langle 2|\mu|b\rangle}{t}, \quad (3.37)$$

as follows:

$$2\text{Im}\left(\mathcal{M}_{qQ \rightarrow qQ}^{\text{NLO}, II}\right) = \frac{1}{(2\pi)^2} \int d^4 k \delta((p_a - k)^2) \delta((p_b + k)^2) \quad (3.38)$$

$$\mathcal{M}_{q^-Q^- \rightarrow q^-Q^-}^{\text{LO}}(k) \mathcal{M}_{q^-Q^- \rightarrow q^-Q^-}^{\dagger \text{LO}}(k - q), \quad (3.39)$$

where  $\text{Im}(\cdot)$  denotes the imaginary part,  $k$  is the loop momentum,  $q$  is the momentum transfer and  $\dagger$  denotes Hermitian conjugation. The sum a complete of states here just corresponds to integrating over all possible momenta flowing around the loop. In the High Energy limit we can perform the integration to give:

$$\text{Im}\left(\mathcal{M}_{qQ \rightarrow qQ}^{\text{NLO}, II}\right) = 4\alpha_s^2 s \mathcal{C}_1(T^a, T^b) \int \frac{dk_\perp}{k_\perp(k_\perp - q_\perp)}, \quad (3.40)$$

where  $\mathcal{C}_1(T^a, T^b)$  is the colour factor for the diagram in fig. (3.3a) and  $k_\perp$  is the transverse component of  $k$ . We can now relate the imaginary part of the amplitude to the full amplitude by conjecturing that the amplitude will be logarithmically enhanced as follows:

$$\mathcal{M}_{qQ \rightarrow qQ}^{\text{NLO}, II} = \text{Re}(\mathcal{M}_{qQ \rightarrow qQ}^{\text{NLO}, II}) + i\text{Im}(\mathcal{M}_{qQ \rightarrow qQ}^{\text{NLO}, II}), \quad (3.41)$$

and defining  $\widetilde{\mathcal{M}}_{qQ \rightarrow qQ}^{\text{NLO, II}}$  as the leading logarithmic coefficient of the matrix element:

$$\begin{aligned}\mathcal{M}_{qQ \rightarrow qQ}^{\text{NLO, II}} &= \widetilde{\mathcal{M}}_{qQ \rightarrow qQ}^{\text{NLO, II}} \ln \frac{s}{t} + \text{sub-leading} \\ &= \widetilde{\mathcal{M}}_{qQ \rightarrow qQ}^{\text{NLO, II}} \ln \left( \left| \frac{s}{t} \right| - i\pi \right) + \text{sub-leading},\end{aligned}\tag{3.42}$$

where we have used that  $\frac{s}{t} < 0$ . Comparing real and imaginary parts of eqn. (3.42) and assuming that  $\widetilde{\mathcal{M}}_{qQ \rightarrow qQ}^{\text{NLO, II}}$  is real we see that:

$$\text{Re}(\mathcal{M}_{qQ \rightarrow qQ}^{\text{NLO, II}}) = -\frac{1}{\pi} \text{Im}(\mathcal{M}_{qQ \rightarrow qQ}^{\text{NLO, II}})\tag{3.43}$$

and we can therefore reconstruct the real part of the amplitude as:

$$\text{Re}(\mathcal{M}_{qQ \rightarrow qQ}^{\text{NLO, II}}) = -\frac{4\alpha_s^2 u}{\pi} \mathcal{C}_1(T^a, T^b) \ln \left| \frac{u}{t} \right| \int \frac{dk_\perp}{k_\perp(k_\perp - q_\perp)}.\tag{3.44}$$

The crossed-diagram, (3.3b), also contributes a leading logarithmic piece and is related to eqn. (3.3a) by a crossing symmetry and so we simply replace  $u$  with  $s$  in eqn. (3.44) and calculate a new colour factor,  $\mathcal{C}_2(T^a, T^b)$ :

$$\text{Re}(\mathcal{M}_{qQ \rightarrow qQ}^{\text{NLO, X}}) = -\frac{4\alpha_s^2 s}{\pi} \mathcal{C}_2(T^a, T^b) \ln \left| \frac{s}{t} \right| \int \frac{dk_\perp}{k_\perp(k_\perp - q_\perp)}.\tag{3.45}$$

But in the high energy limit  $s \sim -u$  (this is clear from eqn. (3.8)) and so we can combine these terms and express the leading logarithmic NLO term in terms of the leading order result:

$$\mathcal{M}_{qQ \rightarrow qQ}^{\text{NLO}} = \frac{3\alpha_s}{\pi^2} \hat{\alpha}(q) \ln \left| \frac{s}{t} \right| \mathcal{M}_{qQ \rightarrow qQ}^{\text{LO}},\tag{3.46}$$

where:

$$\hat{\alpha}(q) = \int dk_\perp \frac{q_\perp^2}{k_\perp(k_\perp - q_\perp)}\tag{3.47}$$

From eqn. (3.46) we can see the logarithmic enhancement explicitly; there is still a suppression from the inclusion of an extra factor of  $\alpha_s$  with respect to the leading order term but as we have seen previously the logarithm is related to the kinematics of the final state - namely - the rapidity gap between the outgoing quarks  $p_1$  and  $p_2$  and

compensate for the smallness of  $\alpha_s$ . Eqn. (3.47) will clearly diverge when we come to integrate over the soft region (where  $k_\perp$  is very small). This divergence will be treated, that is regularised and shown to cancel, in chapter 4.

### 3.6 *t*-channel Dominance

In what follows we construct high multiplicity matrix elements by approximating the full result by the contraction of two currents and a number of effective vertices. This choice allows us to construct matrix elements with a simple form which contains the leading logarithms by ensuring that they have the maximal number of gluons exchanged in the *t*-channel.

As a simple example we consider the production of 4 exclusive jets in the High Energy limit. Fig. (3.4) shows three diagrams which all contribute at leading order in  $\alpha_s$ ; fig. (3.4a) has three gluons exchanged in the *t*-channel and so its amplitude will have propagator terms akin to:

$$\mathcal{M}_{(a)} \sim \frac{1}{(p_a - p_1)^2(p_a - p_1 - p_2)^2(p_a - p_1 - p_2 - p_3)^2}, \quad (3.48)$$

arising from the gluon propagators. By contrast figs. (3.4b) and (3.4c) will have, in place of (3.48):

$$\mathcal{M}_{(b)} \sim \frac{\not{p}_a - \not{p}_1}{(p_a - p_1)^2(p_a - p_1 - p_2)^2(p_a - p_1 - p_2 - p_3)^2}, \quad (3.49)$$

and,

$$\mathcal{M}_{(c)} \sim \frac{(\not{p}_a - \not{p}_1)(\not{p}_4 - \not{p}_b)}{(p_a - p_1)^2(p_a - p_1 - p_2)^2(p_a - p_1 - p_2 - p_3)^2}, \quad (3.50)$$

respectively. Since in the High Energy limit we have  $p_a \sim p_1$  and  $p_b \sim p_4$  it is clear that  $\mathcal{M}_{(b)}$  and  $\mathcal{M}_{(c)}$  will be suppressed with respect to  $\mathcal{M}_{(a)}$ . Clearly this is only a heuristic argument but it is sufficient to motivate the construction of high multiplicity amplitudes from *t*-channel gluon exchanges with the understanding that any other diagrams will be formally sub-leading. We call the configurations with a maximal number of gluons exchanged in the *t*-channel an ‘FKL’ configuration; For example fig. (3.4a) is an FKL configuration while fig. (3.4b) and fig. (3.4c) are ‘non-FKL’ configurations.

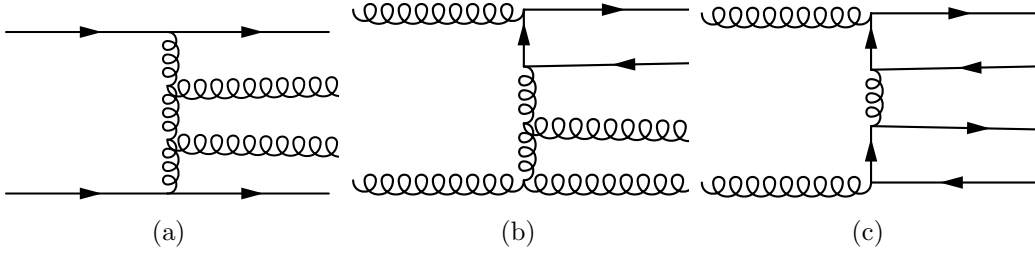


Figure 3.4: Three processes contributing to exclusive quad-jet production. (a) has the maximum number of gluons exchanged in the  $t$ -channel (three) and will dominate in the High Energy limit, (b) and (c) only have two and one gluon which can reggeise. As such as we move from left to right we will lose powers of large logarithms but maintain the same power of  $\alpha_s$  and therefore we can reasonably approximate quad-jet production by neglecting (b) and (c).

A more formal argument for which processes dominate in this limit was given by Fadin and Lipatov [21, 54]. They found that, in the High Energy limit, scattering amplitudes scaled in the same way as was predicted by Regge theory. This states that in the large invariant mass region a  $2 \rightarrow n$  matrix element has a limiting behaviour determined by the maximum spin of any particle which could be exchanged in the  $t$ -channel between final state partons neighbouring in rapidity. We can then find the scaling of a process, for example  $qg \rightarrow qg$ , in particular regions of phase space where either  $y_g \gg y_q$  or  $y_q \gg y_g$  simply by drawing the associated colour connection diagrams for it. This is shown in (3.5). Since when we have  $y_g \gg y_q$  it is only possible to exchange a colour triplet (with spin one half) the cross-section will be dominated by the region where  $y_q \gg y_g$ . The case for  $2 \rightarrow n$  is similar with the limiting behaviour of the matrix element given by

$$\mathcal{M}_{2 \rightarrow n}^{\text{HE}} \sim s_{12}^{\omega_1} \cdots s_{(n-1)n}^{\omega_{(n-1)}}. \quad (3.51)$$

Eqn. (3.51) now makes the previous discussion regarding figs. (3.4) formally clear since fig. (3.4a) will scale like:

$$\mathcal{M}_{2 \rightarrow 4}^{\text{HE}} \sim s_{12}s_{23}s_{34}, \quad (3.52)$$

in the High Energy limit while figs. (3.4b) and (3.4c) will scale like:

$$\begin{aligned}\mathcal{M}_{2 \rightarrow 4}^{\text{HE}} &\sim s_{12}^{1/2} s_{23} s_{34}, \\ \mathcal{M}_{2 \rightarrow 4}^{\text{HE}} &\sim s_{12}^{1/2} s_{23} s_{34}^{1/2},\end{aligned}\tag{3.53}$$

respectively. Since  $s_{ij}$  are all large here, the processes with a (anti)quark exchanged in the  $t$ -channel will be highly suppressed.

To further illustrate this we can look at the various processes contributing to the two jet exclusive cross-section, and in particular, the High Energy limits of their matrix elements. Table 3.1 shows several examples of parton level processes and their exact leading order matrix elements [60]. We can see clearly from this that any process which can proceed through a  $t$ -channel gluon exchange has a term proportional to  $s^2/t^2$  which will dominate in the High Energy limit; for example  $q\bar{Q} \rightarrow q\bar{Q}$  has only the diagram which such an exchange. Conversely processes in which a  $t$ -channel gluon diagram can not contribute are suppressed in this limit. For example  $q\bar{q} \rightarrow Q\bar{Q}$  may only happen via an  $s$ -channel gluon and we can see that in the limit  $s \rightarrow \infty$  and  $t \rightarrow 0$  its matrix element tends to  $4/9$ . Processes like  $gg \rightarrow gg$  have diagrams with *and* without the exchange we are interested in and, as such, only some of the terms from the exact leading order matrix element contribute - but they do still contribute.

### 3.7 Effective Vertices For Real Emissions

In order to generalise what we have done so far to higher multiplicity scattering events we begin by considering  $qQ \rightarrow qQg$  in the high energy limit. The five diagrams which

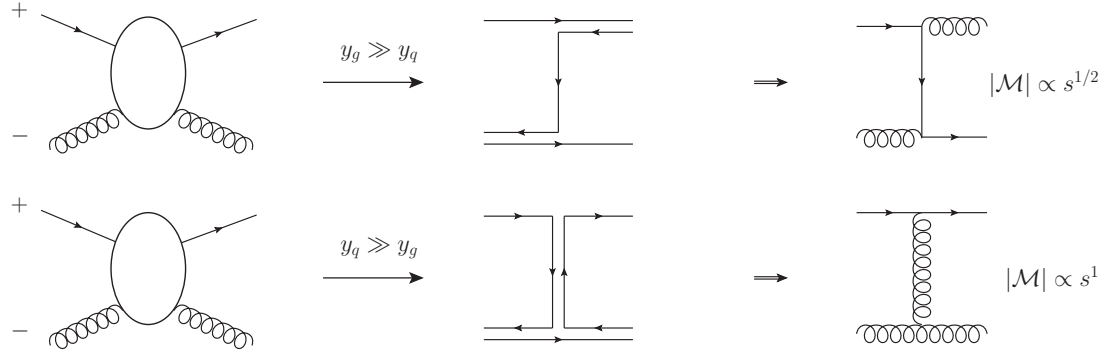


Figure 3.5: The limiting behaviour of  $qg \rightarrow qg$  in the regions of phase space where either  $y_g \gg y_q$  or  $y_q \gg y_g$ . The intermediate diagrams indicate the flow of colour through the process.

Process	$1/g^4  \bar{\mathcal{M}} ^2$
$qQ \rightarrow qQ$	$\frac{4}{9} \frac{s^2+u^2}{t^2}$
$q\bar{Q} \rightarrow q\bar{Q}$	$\frac{4}{9} \frac{s^2+u^2}{t^2}$
$qq \rightarrow qq$	$\frac{4}{9} \left( \frac{s^2+u^2}{t^2} + \frac{s^2+t^2}{u^2} \right) - \frac{8}{27} \frac{s^2}{ut}$
$q\bar{q} \rightarrow Q\bar{Q}$	$\frac{4}{9} \frac{t^2+u^2}{s^2}$
$gg \rightarrow gg$	$\frac{9}{2} \left( 3 - \frac{tu}{s^2} - \frac{su}{t^2} - \frac{st}{u^2} \right)$

Table 3.1: Some examples of  $2 \rightarrow 2$  leading order matrix elements which contribute to the two jet exclusive cross-section.

contribute at leading order are given in fig. (3.6). The diagram where the extra gluon is emitted from the  $t$ -channel gluon is given by:

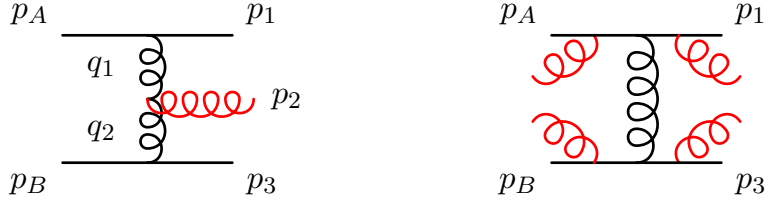


Figure 3.6: The 5 possible emission sites of extra QCD radiation in  $qQ \rightarrow qQ$ . Fig. from [15].

$$\begin{aligned} \mathcal{M}_{t\text{-channel}} = & - \frac{g_s^3}{t_{a1} t_{b2}} f^{i2j} T_{1a}^i T_{3b}^j \langle 1 | \rho | a \rangle \langle 3 | \mu | b \rangle \epsilon_{2\nu}^* \\ & (2p_2^\mu g^{\nu\rho} - 2p_2^\rho g^{\mu\nu} - (q_1 + q_2)^\nu g^{\mu\rho}), \end{aligned} \quad (3.54)$$

and the remaining four diagrams contribute like:

$$\begin{aligned} \mathcal{M}_{\text{Eik.}} = & (ig_s)^3 \epsilon_{2\nu} \left( T_{1i}^2 T_{ia}^d T_{3b}^d \frac{2p_1^\nu \langle 1 | \mu | a \rangle + \langle 1 | \nu | 2 \rangle \langle 2 | \mu | a \rangle}{s_{12} t_{b3}} \langle 3 | \mu | b \rangle \right. \\ & + T_{1i}^d T_{ia}^2 T_{3b}^d \frac{2p_a^\nu \langle 1 | \mu | a \rangle - \langle 1 | \mu | 2 \rangle \langle 2 | \nu | a \rangle}{t_{a2} t_{b3}} \langle 3 | \mu | b \rangle \\ & + T_{3i}^2 T_{ib}^d T_{1a}^d \frac{2p_3^\nu \langle 3 | \mu | b \rangle + \langle 3 | \nu | 2 \rangle \langle 2 | \mu | b \rangle}{s_{32} t_{a1}} \langle 1 | \mu | a \rangle \\ & \left. + T_{3i}^d T_{ib}^2 T_{1a}^d \frac{2p_b^\nu \langle 3 | \mu | b \rangle - \langle 3 | \mu | 2 \rangle \langle 2 | \nu | b \rangle}{t_{b2} t_{a1}} \langle 1 | \mu | a \rangle \right). \end{aligned} \quad (3.55)$$

In the High Energy limit the second term in each of the line is suppressed with respect

to the first and can therefore be disregarded. This turns out to be equivalent to if we considered  $p_2$  as a soft emission using the Eikonal approximation. The resulting amplitude for the sum of all four may be written in terms of the tree level amplitude as:

$$\begin{aligned} \mathcal{M}_{\text{Eik.}} = (ig_s)^3 \epsilon_{2\nu} \langle 1|\mu|a\rangle \langle 3|\mu|b\rangle & \left( T_{1i}^2 T_{ia}^d T_{3b}^d \frac{2p_1^\nu}{s_{12} t_{b3}} + T_{1i}^d T_{ia}^2 T_{3b}^d \frac{2p_a^\nu}{t_{a2} t_{b3}} \right. \\ & \left. + T_{3i}^2 T_{ib}^d T_{1a}^d \frac{2p_3^\nu}{s_{32} t_{a1}} + T_{3i}^d T_{ib}^2 T_{1a}^d \frac{2p_b^\nu}{t_{b2} t_{a1}} \right). \end{aligned} \quad (3.56)$$

We now use that  $p_a \sim p_1 = p_+$  and  $p_b \sim p_2 = p_-$ :

$$\begin{aligned} \mathcal{M}_{\text{Eik.}} = (ig_s)^3 \epsilon_{2\nu} \langle 1|\mu|a\rangle \langle 3|\mu|b\rangle & \left( \frac{2p_+^\nu}{p_+ \cdot p_2 t_{b3}} (T_{1i}^2 T_{ia}^d - T_{1i}^d T_{ia}^2) T_{3b}^d \right. \\ & \left. + \frac{2p_-^\nu}{p_- \cdot p_2 t_{a1}} (T_{3i}^2 T_{ib}^d - T_{3i}^d T_{ib}^2) T_{1a}^d \right). \end{aligned} \quad (3.57)$$

Now tidying up the colour factors:

$$\mathcal{M}_{\text{Eik.}} = (ig_s)^3 \epsilon_{2\nu} \langle 1|\mu|a\rangle \langle 3|\mu|b\rangle f^{2de} T_{3b}^b T_{1a}^e \frac{1}{t_{a1} t_{b3}} \left( \frac{2p_+^\nu}{p_+ \cdot p_2} t_{a1} - \frac{2p_-^\nu}{p_- \cdot p_2} t_{b3} \right), \quad (3.58)$$

which has a colour factor similar to that found for the diagrams with a gluon emitted from the  $t$ -channel gluon. We choose to ‘symmetrise’ eqn. (??) by returning to  $p_{a/1}$  and  $p_{b/3}$  explicitly in place of  $p_+$  and  $p_-$  respectively:

$$\begin{aligned} \mathcal{M}_{\text{Eik.}} = (ig_s)^3 \epsilon_{2\nu} \langle 1|\mu|a\rangle \langle 3|\mu|b\rangle f^{2de} T_{3b}^b T_{1a}^e \frac{1}{t_{a1} t_{b3}} & \\ \frac{1}{2} \left( \frac{2p_a^\nu}{p_a \cdot p_2} t_{a1} + \frac{2p_1^\nu}{p_1 \cdot p_2} t_{a1} - \frac{2p_b^\nu}{p_b \cdot p_2} t_{b3} - \frac{2p_3^\nu}{p_3 \cdot p_2} t_{b3} \right). \end{aligned} \quad (3.59)$$

We now consider (3.54). The final term contracts the two currents and so it is only the first two terms which need to be massaged into the right form. Once again we

approximate using  $p_a \sim p_1 = p_+$  and  $p_b \sim p_3 = p_-$  to write the currents as momenta. Upon doing this we find:

$$\begin{aligned} \mathcal{M}_{t\text{-channel}} = & -\frac{g_s^3}{t_{a1}t_{b2}} f^{i2j} T_{1a}^i T_{3b}^j \epsilon_{2\nu}^* \\ & \left( 8e^{i\phi_-} (p_+^\nu p_- \cdot p_2 - p_-^\nu p_+ \cdot p_2) - (q_1 + q_2)^\nu \langle 1|\mu|a\rangle \langle 3|\mu|b\rangle \right), \end{aligned} \quad (3.60)$$

where  $\phi_-$  is a phase resulting from the spinor conventions detailed in chapter 2. Now using that  $s \sim 2p_+ \cdot p_- = \frac{1}{2}\langle 1|\mu|a\rangle \langle 3|\mu|b\rangle e^{-i\phi_-}$  we can write all three terms as something proportional to the desired current structure:

$$\begin{aligned} \mathcal{M}_{t\text{-channel}} = & -\frac{g_s^3}{t_{a1}t_{b2}} f^{i2j} T_{1a}^i T_{3b}^j \epsilon_{2\nu}^* \langle 1|\mu|a\rangle \langle 3|\mu|b\rangle \\ & \left( 4 \left( p_+^\nu \frac{p_- \cdot p_2}{s} - p_-^\nu \frac{p_+ \cdot p_2}{s} \right) - (q_1 + q_2)^\nu \right). \end{aligned} \quad (3.61)$$

Similarly as for  $\mathcal{M}_{\text{Eik.}}$  we chose to include as much of the actual kinematic information as possible by symmetrising (3.61) to get:

$$\begin{aligned} \mathcal{M}_{t\text{-channel}} = & -\frac{g_s^3}{t_{a1}t_{b2}} f^{i2j} T_{1a}^i T_{3b}^j \epsilon_{2\nu}^* \langle 1|\mu|a\rangle \langle 3|\mu|b\rangle \\ & \left( -(q_1 + q_2)^\nu + \frac{1}{2} \left( p_a^\nu \frac{p_2 \cdot p_b}{p_a \cdot p_b} + p_a^\nu \frac{p_2 \cdot p_3}{p_a \cdot p_3} + p_1^\nu \frac{p_2 \cdot p_b}{p_1 \cdot p_b} + p_1^\nu \frac{p_2 \cdot p_3}{p_1 \cdot p_3} \right. \right. \\ & \left. \left. - p_b^\nu \frac{p_2 \cdot p_a}{p_a \cdot p_b} - p_b^\nu \frac{p_1 \cdot p_2}{p_b \cdot p_1} - p_2^\nu \frac{p_2 \cdot p_a}{p_a \cdot p_3} - p_2^\nu \frac{p_1 \cdot p_2}{p_1 \cdot p_3} \right) \right). \end{aligned} \quad (3.62)$$

Since eqns. (3.62) and (3.59) to the same colour factor we can simply sum them to get:

$$\mathcal{M}_{qQ \rightarrow qQg} = \frac{S_{qQ \rightarrow qQ}}{t_{a1}t_{b2}} f^{2de} T_{3b}^b T_{1a}^e g_s^3 \epsilon_\rho^* V_\rho(q_1, q_2), \quad (3.63)$$

where

$$V^\rho(q_1, q_2) = -(q_1 + q_2)^\rho + \frac{p_a^\rho}{2} \left( \frac{q_1^2}{p_a \cdot p_2} + \frac{p_2 \cdot p_b}{p_a \cdot p_b} + \frac{p_2 \cdot p_3}{p_a \cdot p_3} \right) + (p_a \leftrightarrow p_1) \\ - \frac{p_b^\rho}{2} \left( \frac{q_2^2}{p_b \cdot p_2} + \frac{p_2 \cdot p_a}{p_b \cdot p_b} + \frac{p_2 \cdot p_1}{p_b \cdot p_1} \right) - (p_b \leftrightarrow p_3). \quad (3.64)$$

Eqn. (3.64) is manifestly gauge invariant which can be checked explicitly by calculating  $p_g \cdot V$ . It is, however clearly divergent: if any of  $p_a$ ,  $p_b$ ,  $p_1$ ,  $p_2$  or  $p_3$  becomes soft then the momenta contractions in the denominators of eqn. (3.64) will become zero and the whole expression will explode. We organise the cancellation of divergences is shown to cancel in the following chapter.

Armed with eqn. (3.64) and the quark and gluon currents we can calculate high multiplicity matrix elements by generalising eqn. (3.70) to include contractions of this effective vertex expression. The  $2 \rightarrow n$  matrix element squared for  $qQ$  scattering is therefore given by:

$$|\bar{\mathcal{M}}_{qQ \rightarrow qg \dots gQ}^t|^2 = \frac{1}{4(N_c^2 - 1)} \frac{g^2 C_F}{t_1} \frac{g^2 C_F}{t_2} \sum_{h_a, h_b, h_1, h_2} |S_{qQ \rightarrow qQ}^{h_a h_b \rightarrow h_1 h_2}|^2 \\ \times \prod_{i=1}^{n-1} \left( \frac{-g_s C_A}{t_i t_{i+1}} V^\mu(q_i, q_{i+1}) V_\mu(q_i, q_{i+1}) \right). \quad (3.65)$$

Using eqn. (3.65) we can describe the real emission high order corrections but this expression is manifestly divergent for the reasons outlined in section 2.3. As in section 2.7.2 we must calculate the virtual corrections to render the integrated cross section finite.

### 3.8 Virtual Corrections To All Orders

Thus far we have a prescription for approximating high energy scattering amplitudes with additional real radiation added through the effective vertices described in section (3.7). However, to complete our picture we must also include the virtual corrections to the process in a similar way to the example shown in section (2.7.2). This is important not only since these processes obviously contribute to the process but also because, as we saw in the one loop  $\gamma^* \rightarrow q\bar{q}$  calculation, the soft divergences in eqn. (3.64) need to be cancelled. Both the cancellation in section (2.7.2) and the

cancellation we will see here are examples of the KLN theorem [57] which states that the soft and virtual divergences in QCD must cancel - though of course we must still show that this is the case and that our final result is manifestly finite.

In the High Energy limit we may include the virtual corrections to all orders in  $\alpha_s$  by using the Lipatov ansatz [54]. For  $t$ -channel gluons we replace the usual gluon propagator with a ‘dressed’ version:

$$\frac{1}{q_i^2} \rightarrow \frac{1}{q_i^2} e^{\hat{\alpha}(q_i)\Delta_{i,i-1}}, \quad (3.66)$$

where:

$$\hat{\alpha}(q_i) = \alpha_s C_A q_i^2 \int \frac{d^{2+2\epsilon} k_\perp}{(2\pi)^{2+2\epsilon}} \frac{1}{k_\perp^2 (k_\perp - q_{i\perp})^2} \mu^{-2\epsilon}, \quad (3.67)$$

and  $\Delta_{i,i-1}$  is the rapidity gap between the external gluon legs emitted from the dressed gluon. Similarly to eqn. (3.64) in the preceding section this new expression for the propagator contains divergences arising from the soft limit of the integral in the expression for  $\hat{\alpha}(q_i)$ . In the following chapter we show in some detail that these divergences cancel with those mentioned in section 3.7.

The keen reader will have noticed that eqn. (3.67) is exactly what we found in our next-to-leading order calculation in eqn. (3.47) expressed in  $2 + 2\epsilon$  dimensions rather than 2 (save for a few numerical factors). This is no coincidence and, indeed, is the source of the ansatz. Higher order (in  $\alpha_s$ ) calculations [33, 38] have shown that to two loops the leading logarithmic part of the full amplitude is found exactly by expanding the exponential term in eqn. (3.66).

## 3.9 High Energy Jets

### 3.9.1 The High Energy Jets Framework

The High Energy Jets framework is the basis of the later chapters of this thesis. Details of this framework beyond the brief summary presented here may be found in [13, 15–17, 51].

### 3.9.2 Factorisation Into Currents

The High Energy Jets framework is based, in part, on the observations of sections (3.3) and (3.4).

In this sections we saw that in the High Energy limit we can write down matrix elements in the form of two vector ‘currents’ contracted over a  $t$ -channel pole. While one could argue that the fact that the  $qQ \rightarrow qQ$  matrix element would factorise into a contraction of two vector currents with a  $t$ -channel pole was obvious (since the only contribution was from a  $t$ -channel diagram!), it was not at all obvious that this would also be the case for the  $qg \rightarrow qg$  amplitude would. It can also be shown that the same structure is found even in the case of gluon-gluon scattering [17].

It turns out that this factorisation into a form with only a  $t$ -channel pole holds for all the helicity configurations where the helicities of the incoming-outgoing parton lines remain unchanged. For those diagrams where the helicity *is* flipped we find poles in  $s$  and  $u$  and so these contributions are heavily suppressed in the High Energy limit. The fact that all of the approximate helicity averaged matrix elements squared for any combination of incoming partons,  $a$  and  $b$ , can be written as:

$$|\bar{\mathcal{M}}_{2 \rightarrow 2}| \sim \sum_{h_a, h_b, h_1, h_2} \left| \frac{j_a^\mu(p_a, p_1) j_{b,\mu}(p_b, p_2)}{t} \right|^2, \quad (3.68)$$

is exploited in High Energy Jets to express more general matrix elements (those with higher multiplicity or more complicated final states) approximately.

For example by constructing a current describing a  $W^\pm$  boson being emitted from an incoming-outgoing quark line we can then write down the matrix element for the process  $q'q \rightarrow (W^\pm \rightarrow) \nu e^\pm q'Q$  as:

$$|\bar{\mathcal{M}}_{2 \rightarrow 2}|^2 \sim \sum_{h_a, h_b, h_1, h_2, h_{e^\pm}, h_\nu} \left| \frac{j_{W^\pm}^\mu(p_a, p_1, p_{e^\pm}, p_\nu) j_\mu(p_b, p_2)}{t} \right|^2, \quad (3.69)$$

where the quark line which emitted the  $W^\pm$  has changed flavour from  $q$  to  $Q$ . Eqn. (3.69) is an approximation which, technically, is only valid in the strict limit of infinite invariance mass between the outgoing quarks however, as we will see later, this approximation does a remarkably good job at describing data far away from its formal region of applicability.

Here is a convenient place to define the ‘ $t$ -channel factorised’ form for matrix elements,

$\overline{\mathcal{M}}_{qQ \rightarrow qQ}^t$ , in which we extract the  $t$  poles from the rest of the matrix element [15]. We write the square of eqn. (3.11) as:

$$|\overline{\mathcal{M}}_{qQ \rightarrow qQ}^t|^2 = \frac{1}{4(N_c^2 - 1)} \frac{g^2 C_F}{t_1} \frac{g^2 C_F}{t_2} \sum_{h_a, h_b, h_1, h_2} |S_{qQ \rightarrow qQ}^{h_a h_b \rightarrow h_1 h_2}|^2, \quad (3.70)$$

where  $N_c = 3$  and  $C_F = 4/3$  for QCD,  $S$  is the matrix element for a  $2 \rightarrow 2$  process in the form of a contraction of two currents, and  $t_i$  are the squared  $t$ -channel momenta - in this case  $t_1 = (p_a - p_1)^2$  and  $t_2 = (p_2 - p_b)^2$ .

While for the  $2 \rightarrow 2$  examples in section (3.3) and section (3.4) eqn. (3.70) is just an exact rewriting of a previous result however we will use the form shown here to generalise to describing extra final state radiation in the next section at which point the  $t$ -channel factorisation weakens to an approximation of the full result (but one which contains enough of the underlying physics to be useful nonetheless).

Extending eqn. (3.70) to more higher multiplicity final states within the High Energy Jets framework is then done by using chains of products of effective vertices discussed in section (3.7) (for the real emissions) and the Lipatov ansatz described in section (3.8) (for the virtual emissions).

### 3.9.3 The High Energy Jets Monte Carlo

The High Energy Jets framework is implemented in a general purpose Monte Carlo, referred to simply as **HEJ**, and publicly available at <http://hej.web.cern.ch/HEJ/>. This C++ package is under continual development to test and improve it and the work of chapter 4 (among many other tweaks and improvements) was contributed to it throughout the course of this work.

Here we briefly summarise the main aspects of the software aspects of High Energy Jets. A general HEJ run consists of three main stages.

1. **Setup:** a setup phase at which point a user defined input file is parsed and, based on the specifics of the input, one of several class hierarchies is initialised after which essential components for the physics stage are constructed including: an interface to a PDF package (either **MSTW** or **LHAPDF** (v6)), a (pseudo-)random number generator and a physics analysis.

HEJ comes with a stand-alone analysis class which implements many standard operations and is therefore sufficient in most cases however it may also be interfaced with the **Rivet** analysis package; this is particularly useful when

comparing Monte Carlo results to data since many analyses are implemented in `Rivet` routines and it is, in principle, just a matter of plugging in the right analysis name.

2. **Monte Carlo Generation:** In the Monte Carlo stage of a `HEJ` run we proceed iteratively over a (typically very large) number of events. For each event we much generate a phase space; how many outgoing partons and with what momentum they carry. With this information we can use our knowledge of  $x_a$  and  $x_b$  and the importance sampling ideas discussed in chapter 2 to randomly generate parton types for our incoming partons - there are, of course, additional constraints which are process dependent to consider. For example, we will never select a gluon-gluon incoming pairing if we wish to calculate the matrix element for  $Z/\gamma^* + \text{jets}$  in an FKL configuration since this would be computationally wasteful.

Once we have a definite phase space and the incoming types have been specified we can calculate the matrix element using some generalisation of eqn. (3.70) - the exact matrix element used will depend on the final state multiplicity and the process chosen by the user in stage (1). Virtual corrections are also included at this stage.

Lastly we perform a multiplicative matching to the exact leading order matrix element provided by `MadGraph` (v5), the details of which will be discussed further in chapter 4.

3. **Analysis:** In the analysis stage the event is passed off to either the `HEJ` analysis framework or to `Rivet` (depending on the user input file). Here we enforce kinematic constraints on our final state to study on the regions of phase space we are interested in - or those regions probed by a particular experimental analysis whose results we wish to compare to. In `HEJ` it is possible perform a complete run ‘un-cut’ whereby the generated events are outputted before the analysis phase in to a given format (`ROOT` N-tuples, `LH` events and `HepMC` (v2) records are all supported). This is preferable when the same generation can be reused multiple times however for very long runs outputting all of the events becomes unfeasible and we must take the second option of performing `HEJ` analyses on-the-fly i.e. cutting as iterate through events.

While this breakdown is a good broad strokes overview of `HEJ` there are hundreds of intricacies which must be treated along the way. One worth mentioning is the calculation of scale uncertainty bands for predictions. In section (2.3) we discussed how some given observable,  $R$ , will depend on the renormalisation scale,  $\mu_r$ , or more specifically - how is must not. Our theory is, after all, meaningless if its predictions

are effected by a choice of an unphysical scale. However, when we do our perturbative expansion (through a resummation or fixed-order approach) we develop a dependence on this scale. It is important to understand the size of this dependence and so when generating Monte Carlo predictions we must produce not only a ‘central’ prediction for each value but also an associated ‘scale uncertainty’ band. For fixed-order calculations this is simple a case of varying  $\alpha_s$  through the value of  $\mu_r$  but since the High Energy Jets matrix element contains scale dependence through the QCD coupling *and* the Lipatov ansatz we must evaluate entire matrix elements at a variety of scales to properly understand our dependence and to provide meaningful predictions. The factorisation scale dependence must also be varied (in a tandem with varying  $\mu_r$ ) to get a complete scale uncertainty band and this is run by default as part of HEJ.

### 3.9.4 Matching to HEJ+ARIADNE

The current schema for describing all-order corrections to jet rates at hadronic colliders is based on the limit in which emissions are both hard and well separated. Of course, some radiation at hadronic colliders is soft or produced collinear to other radiation (or both) and such emissions lead to large logarithmic enhancements similar to those discussed in this work (I stress here that by similar I mean their effect on the assumptions behind fixed-order perturbation theory is similar - their *soft and collinear* cause is completely opposite to the *hard wide-angle* logarithms resummed here!).

These effects can be included by including a parton shower description. Several schemes for performing this ‘matching’. The CKKW(L) and MLM schemes work by generating showered predictions and then applying a correction above some merging scale above which the hard scatter is considered to be the dominant force. In this way fixed order predictions can be augmented to also contain the leading logarithms from the parton shower.

HEJ has been matched to the HEJ+ARIADNE parton shower [14]. HEJ+ARIADNE is based on the Lund colour dipole model which attempts to describe final state QCD radiation resulting from a hard scatter: it considers the splitting of colour dipoles in to more colour dipoles rather than partons splitting to more partons. It calculates the probability of an emission from the splitting function,  $\mathcal{D}(p_\perp^2, y)$ , as being approximately given by:

$$\mathcal{D}(p_\perp^2, y) \approx \frac{z}{16\pi^2} \frac{|\mathcal{M}_{n+1}|^2}{|\mathcal{M}_n|^2}. \quad (3.71)$$

From this we can define ‘no-emission’ probabilities,  $\Delta(p_{1\perp}^2, p_{2\perp}^2)$ , which give us the probability that we don’t emit extra radiation as we evolve a partons transverse momentum between two scales  $p_{1\perp}^2$  and  $p_{2\perp}^2$ :

$$\Delta(p_{1\perp}^2, p_{2\perp}^2) = \exp \left( - \int_{p_{1\perp}^2}^{p_{2\perp}^2} dp_{\perp}^2 \int dy \mathcal{D}(p_{\perp}^2, y) \right). \quad (3.72)$$

When it comes to matching the High Energy Jets framework to `HEJ+ARIADNE` the matching picture is different. As we will see later on, we include radiation down to a very soft scale (this is required in order to render the integrated cross-section finite) and so were we to perform a naïve matching to a parton shower we would be double-counting all of the soft non-collinear radiation. As such we....

### 3.9.5 Comparisons to data

- No more plots! Talk about and reference the papers instead...



# Chapter 4

## **$Z/\gamma^* + \text{Jets}$ at the LHC**

Except where otherwise referenced the work in this chapter and the subsequent chapters refers to work undertaken as part of the High Energy Jets collaboration.

This work is the theoretical foundation for the full-flexible parton level Monte Carlo generator available publicly from

<http://hej.web.cern.ch/HEJ/>

and is published in [51].

### **4.1 Introducing $Z/\gamma^* + \text{Jets}$ at the LHC**

The Large Hadron Collider (LHC) opens up a new region of energies for hadronic collisions. It has already been a resounding success with the discovery of the scalar Higgs boson completing the particle content of the Standard Model (SM). Hadronic colliders, by their very nature, lead to final states with large amounts of QCD radiation and being able to accurately describe this is essential. Both the SM and many ‘Beyond the Standard Model’ (BSM) theories predict events with multiple jets in the final state.

The current best approach for describing QCD radiation is through the use of a Monte Carlo (MC) generator using the basic principles outlined in section 2.9. A wide range of such MC generator are available implementing everything from fixed-order perturbative schemes such as those described in [] to parton shower models which resum the logarithms arising from soft and collinear logarithms []. This soft and collinear radiation is experimentally observed to cascade from outgoing high energy quarks and gluons in chaotic patterns we refer to as jets. While parton showers do a good job of describing the composition of jets they do not give the correct description of the

$p_T$  spectrum of events with a high multiplicity of jets. It is also possible, through a procedure known as ‘matching’, to combine the theoretical ideas behind fixed order and parton shower predictions. These schemes typically produce resummed results and then match to either leading order [1] or next-to-leading [2] results giving a formal accuracy of LO+LL or NLO+LL respectively. This approach gives a better description of multi-jet states however the current state-of-the-art for the fixed order component is still next-to-leading order in  $\alpha_s$ .

In the high energy jets framework we aim to resum the large logarithmic corrections arising well separated (in rapidity), hard final state jets. We capture these important terms by shuffling the perturbative expansion and calculating only those diagrams which contribute a ‘leading logarithm’ in the limit we are interested in.

In the remainder of this chapter we discuss how we can describe the production of di-leptons plus multiple hard jets through the emission of an electroweak  $Z^0$  boson and an off-shell photon,  $\gamma^*$ . We do this by constructing a current describing  $Z/\gamma^*$  emission from one of the incoming quark or anti-quark lines and then combine this with a ‘passive’ quark or gluon current as was described in section 3.9.2. The effective vertex derived in section 3.7 can then be used to generalise the resulting matrix element to give an approximate description of the  $(Z/\gamma^* \rightarrow e^+e^- + n \text{ jets})$  final state valid in the High Energy limit of QCD discussed at length in chapter 3. The interference present from the possible emission sites of the  $Z/\gamma^*$  is described exactly by a generalisation of the  $t$ -channel picture which allows for multiple ‘chains’ of momenta flowing through the reggeised gluons in the  $t$ -channel. This approach requires a new regularisation procedure to carefully render the resulting matrix element finite when we consider the cancellation of poles from the Lipatov propagator terms and the effective vertices.

The formal accuracy of the description given here is LO+LL. The leading order accuracy is achieved by performing a multiplicative matching to exact matrix elements generated using `MadGraph5`. As discussed in chapter ?? this required a completely new matching set-up and this too is described later in this chapter along with some of the other computational challenges encountered along the way.

Finally we present a comparison of results from High Energy Jets  $Z/\gamma^*$  plus jets to two recent experimental studies at the LHC; one from the ATLAS collaboration and the other from the CMS experiment. We see that we describe the data well in all of the plots picked by the experiment groups and, indeed, in the regions of phase-space with large rapidity gaps and high invariant mass High Energy Jets gives a better description of the data than the other fixed-order and fixed-order plus parton shower predictions included.

## 4.2 Constructing $Z/\gamma^* + \text{jets}$

We now consider the construction of a current and indeed an all orders inclusive cross-section for the  $Z/\gamma^*$ . We begin by looking at just the  $Z^0$  emission.

### 4.2.1 A Current for $Z^0 + \text{Jets}$

For any given initial state (excluding the case of gluon-gluon scattering which will not contribute an FKL configuration) there are two possible emission sites for the  $Z^0$  per fermion i.e. two for  $qg$  and  $\bar{q}g$  scattering and four for  $qq$ ,  $\bar{q}\bar{q}$  and  $\bar{q}\bar{q}$  scattering. The emission sites on a single fermion line are illustrated in fig. (4.1). In the language of currents discussed previously we call the left hand side of fig. (4.1)  $j_\mu^Z/\gamma^*$ . It is given by:

$$j_\mu^Z = \frac{C_{Zq} C_{Ze}}{p_Z^2 - M_Z^2 + i\Gamma_Z M_Z} \left( \frac{\langle 1 | \gamma^\sigma (\not{p}_{out} + \not{p}_{e^+} + \not{p}_{e^-}) \gamma_\mu | a \rangle}{(p_{out} + p_Z)^2} + \frac{\langle 1 | \gamma^\mu (\not{p}_{in} - \not{p}_{e^+} - \not{p}_{e^-}) \gamma_\sigma | a \rangle}{(p_{in} - p_Z)^2} \right) \langle e^+ | \gamma_\sigma | e^- \rangle, \quad (4.1)$$

where  $M_Z$  is the mass of the  $Z$  boson,  $\Gamma_Z$  is its width,  $C_{Zx}$  is the coupling of the  $Z$  to  $x$ ,  $x = e, q, \nu_e, \dots$  and  $\mu$  is the Lorentz index for the  $t$ -channel gluon propagator.

We can expand the quark and lepton momenta using their completeness relations which, in terms of spinor-helicity brackets, is given by:

$$\not{p}_i = |i_+\rangle\langle i_+| + |i_-\rangle\langle i_-|. \quad (4.2)$$

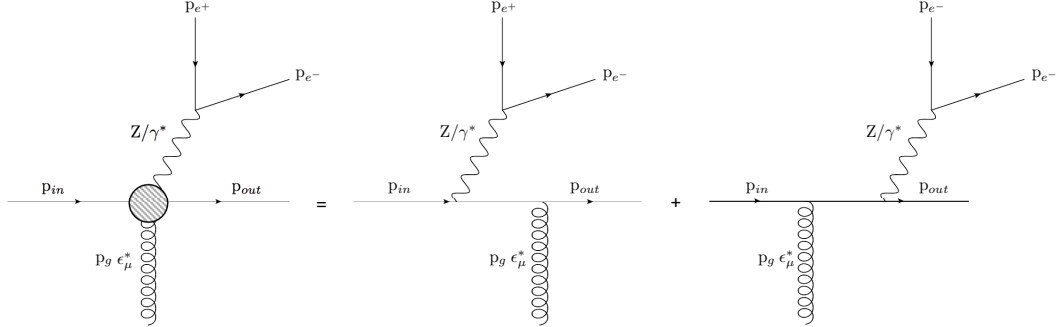


Figure 4.1: The possible emission sites for a neutral weak boson.

This fixes the helicity of the incoming quark,  $h_{in}$ , and the outgoing quark,  $h_{out}$ , to be identical, and we are left with a current which only has four possible helicity configurations depending on  $h_q = h_{in} = h_{out}$  and the electron helicity,  $h_e$ :

$$j_\mu^Z(h_q, h_e) = C_{Zq}^{h_q} C_{Ze}^{h_e} \frac{\langle e_{h_e}^+ | \gamma_\sigma | e_{h_e}^- \rangle}{p_Z^2 - M_Z^2 + i\Gamma_Z M_Z} \\ \times \left( \frac{2p_1^\sigma \langle 1_{h_q} | \gamma^\mu | a_{h_q} \rangle + \langle 1_{h_q} | \gamma^\sigma | e_{h_q}^+ \rangle \langle e_{h_q}^+ | \gamma^\mu | a_{h_q} \rangle + \langle 1_{h_q} | \gamma^\sigma | e_{h_q}^- \rangle \langle e_{h_q}^- | \gamma^\mu | a_{h_q} \rangle}{(p_{out} + p_Z)^2} \right. \\ \left. + \frac{2p_a^\sigma \langle 1_{h_q} | \gamma^\mu | a_{h_q} \rangle - \langle 1_{h_q} | \gamma^\mu | e_{h_q}^+ \rangle \langle e_{h_q}^+ | \gamma^\sigma | a_{h_q} \rangle - \langle 1_{h_q} | \gamma^\mu | e_{h_q}^- \rangle \langle e_{h_q}^- | \gamma^\sigma | a_{h_q} \rangle}{(p_{in} - p_Z)^2} \right). \quad (4.3)$$

We can then express amplitudes for  $Z^0$  plus jets in terms of contractions of a  $Z$  emitting current with either a quark or gluon current discussed previously. Taking the concrete example of  $qg \rightarrow Zqg$  we can write the matrix element as follows:

$$|\bar{\mathcal{M}}_{qg \rightarrow Zqg}^t|^2 = \frac{g_s^2}{8} \frac{1}{(p_a - p_1 - p_{e^+} - p_{e^-})^2 (p_b - p_n)^2} \sum_{h_q, h_e, h_g} |j_\mu^Z(h_q, h_e) j^{g\mu}(h_g)|^2. \quad (4.4)$$

We will investigate eqn. (4.4) for a ‘slice’ through the final state phase-space where each particles momenta is parametrised by:

$$p_i = k_{i\perp} \left( \cosh(y_i); \cos(\phi_i), \sin(\phi_i), \sinh(y_i) \right)$$

and,

$$k_{1\perp} = k_{e^+\perp} = 40 \text{ GeV} \quad k_{e^-\perp} = \frac{m_Z^2}{2k_{e^+\perp} (\cosh(y_{e^+} - y_{e^-}) - \cos(\varphi_{e^+} - \varphi_{e^-}))), \quad (4.5)$$

$$\varphi_1 = \pi \quad \varphi_{e^+} = \pi + 0.2 \quad \varphi_{e^-} = -(\pi + 0.2),$$

$$y_1 = \Delta \quad y_2 = -\Delta \quad y_{e^+} = \Delta \quad y_{e^-} = \Delta - 1.5,$$

So as  $\Delta$  increases we pull the two jets apart in rapidity. In this phase space slice the lepton pair are emitted in the forward region and so the physical picture is that

the incoming quark with  $p_a \sim p_1 = p_+$  emits a  $Z^0$  and then a  $t$ -channel gluon (or a  $t$ -channel gluon and *then* a  $Z^0$ ).

We then observe the behaviour shown in fig. (4.2): as we pull the jets apart in rapidity (i.e. as we go to large  $\Delta$ ) we see that the matrix element approaches a constant; this is the result which would be obtained by using the BFKL formalism in which all jets are taken to be infinitely well separated in rapidity.

As we expect for the case of  $2 \rightarrow 2$  scattering we see exact agreement between our expression and the leading order result obtained from `MadGraph5` [9]. It is clear that the BFKL limit is not obtained until relatively large values for  $\Delta$ , therefore it would be a poor approximation were we to just take the infinite rapidity limit of this as our expression for the  $Z^0$  matrix element.

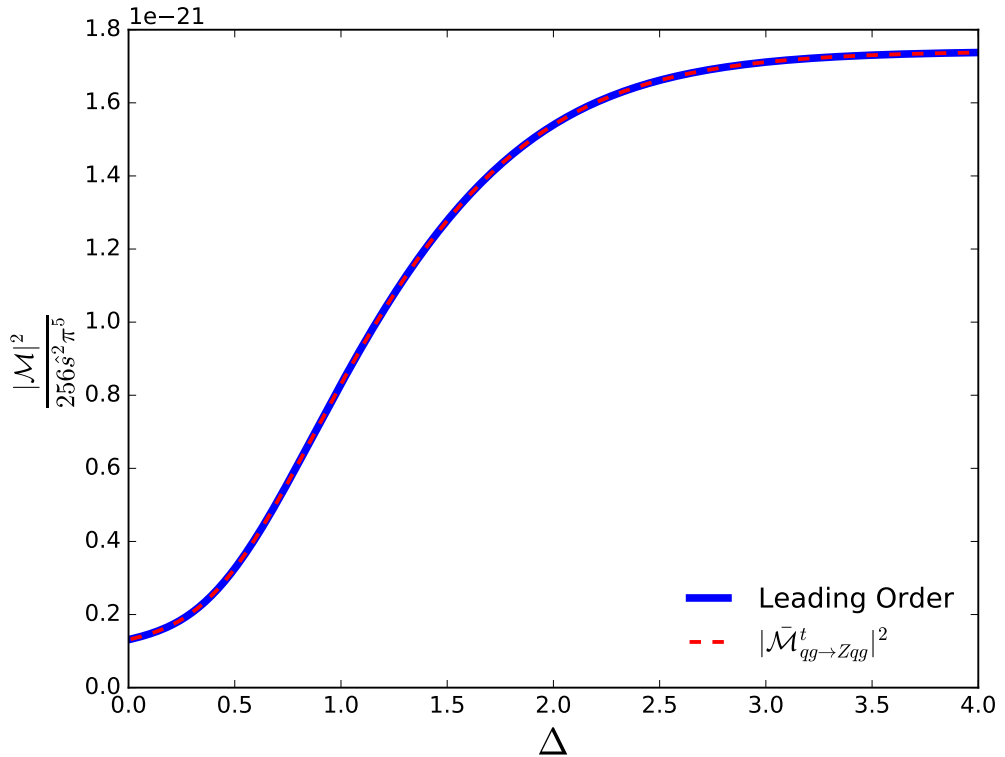


Figure 4.2:  $\overline{|\mathcal{M}_{qg \rightarrow Zqg}^t|^2}$  shown for a slice through the final state phase-space defined by eqn. (4.5). We compare to the leading order result obtained from `MadGraph`.

The picture becomes more complicated when considering the  $qQ \rightarrow ZqQ$  scattering since there are now four possible places where the (anti-)quark may emit the  $Z^0$ . In previous work by the High Energy Jets collaboration the case of  $W^\pm$  plus multiple hard jets was treated by simply attaching the boson to an external quark line probabilistically

[13]. In the case of  $W^\pm$  the interference terms are less of a factor since the emission of the boson changes the flavour of the quark line and so there are less diagrams to contribute to the interference effects. However as we will see later this leads to an approximate matrix element which differs significantly from the leading-order result and so here we will include not only the contributions to the matrix element arising from the  $Z^0$  being emitted from both (anti-) quark legs separately but also the resulting interference term.

### 4.2.2 $Z^0$ Emission Interference

Our high-energy description of the matrix elements relies on the correct description of the  $t$ -channel momenta, and this obviously depends on which of the quark lines the  $Z$  or  $\gamma^*$  was emitted from. We therefore need to modify the simple framework outlined above. We will use the subscript  $a$  ( $b$ ) to label the current at the lowest (highest) end of the rapidity chain. We then define  $t_a$  ( $t_b$ ) to be the  $t$ -channel momentum exchanged when the bosons are emitted at the lowest (highest) end of the rapidity chain. Then the full amplitude squared for  $qQ \rightarrow qQ(Z/\gamma^* \rightarrow) e^+e^-$  is given by:

$$\begin{aligned} |\bar{\mathcal{M}}_{qQ \rightarrow ZqQ}^t|^2 &= g_s^2 \frac{C_F}{8N_c} \left| \frac{j_a^{Z^0} \cdot j_b}{t_a} + \frac{j_a \cdot j_b^{Z^0}}{t_b} \right|^2 \\ &= g_s^2 \frac{C_F}{8N_c} \left( \left| \frac{j_a^{Z^0} \cdot j_b}{t_a} \right|^2 + \left| \frac{j_a \cdot j_b^{Z^0}}{t_b} \right|^2 + 2\Re \left\{ \left( \frac{j_a^{Z^0} \cdot j_b}{t_a} \right) \left( \frac{j_a \cdot j_b^{Z^0}}{t_b} \right)^* \right\} \right), \end{aligned} \quad (4.6)$$

where  $j_{a,b}$  are the pure quark currents defined previously. The coupling constants of the  $Z$  to the relevant quarks and leptons are contained within  $j^{Z^0}(h_q, h_e)$ , as in eqn. ((4.1)).

Fig. (4.3) shows the value of this matrix element squared divided by the squared partonic centre-of-mass energy for increasing rapidity separation of the two jets. Once again the result is compared with that obtained from the full, tree-level matrix elements from **MadGraph5**. The slice through phase space here is the same as that used in the previous section given by eqn. (4.5). Fig. (4.3) also shows the separate contributions to the total matrix element squared coming from the  $Z/\gamma^*$  emission from the forward moving quark line (black, dashed) and emission from the backward moving quark line (green, dotted). In this phase space slice, the leptons also have an increasing positive rapidity and so the forward emission matrix element describes the full matrix element most closely, with the contribution from backward-emission falling at large values of  $\Delta y$ .

The sum of the forward and backward emission matrix elements neglecting interference (magenta, dotted) significantly overestimates the final result. Once the destructive interference effects have been taken into account, the full sum (red, solid) correctly reproduces the LO matrix element (blue, thick solid). It is therefore clear that at low rapidities the inclusion of the interference effect plays an important rôle in the accuracy of the matrix element.

Fig. (4.3) shows that in the region of very high rapidity separation the full matrix element squared (scaled by  $s^2$  and an irrelevant phase space factor) approaches a constant. We could have predicted this behaviour by considering eqn. (3.16); in the strict High Energy limit *all* the rapidity information becomes lost and we only have dependence on  $s$  and the transverse momenta of the outgoing partons. In this case we also have the  $Z^0$  propagator and its couplings to the partons and leptons to consider but the kinematics of the  $t$ -channel gluon still dominates. The limit approached can be easily evaluated by applying the high energy limit, since in the  $\Delta y \rightarrow \infty$  limit only the forward emission term contributes we have:

$$\frac{|\bar{\mathcal{M}}_{qQ \rightarrow ZqQ}^{HE}|^2}{256\pi^5 s^2} = \frac{\alpha_s^2 C_F^2}{64\pi^3 (N_c^2 - 1)} \sum_{h_q, h_e} \frac{|C_{Za}^{h_a} C_{Ze}^{h_e}|^2}{|p_{1\perp}|^2 |p_{2\perp}|^2}. \quad (4.7)$$

Once we have scaled out the invariant mass squared divergence (as well as the usual phase space factor) out we have the limiting behaviour shown in fig (4.3).

### 4.2.3 Photonic Interference

Since any virtual  $Z^0$  could also have proceeded via an off-shell virtual photon,  $\gamma^*$ , we must also include these processes and the resulting interference between the  $Z^0$  and  $\gamma^*$ .

The  $\gamma^*$  emission matrix element is similar to that of the  $Z^0$ -only matrix element shown in equation (4.4) and the same story applies with the possible emission sites causing interference. All that needs to be changed is the propagator term and the couplings of the boson to the emitting (anti-)quark and the decay products. The full current for  $Z/\gamma^*$  emission is then obtained by summing the two separate currents as follows:

$$j_\mu^{Z/\gamma^*}(h_q, h_e) = j_\mu^Z(h_q, h_e) + j_\mu^\gamma(h_q, h_e). \quad (4.8)$$

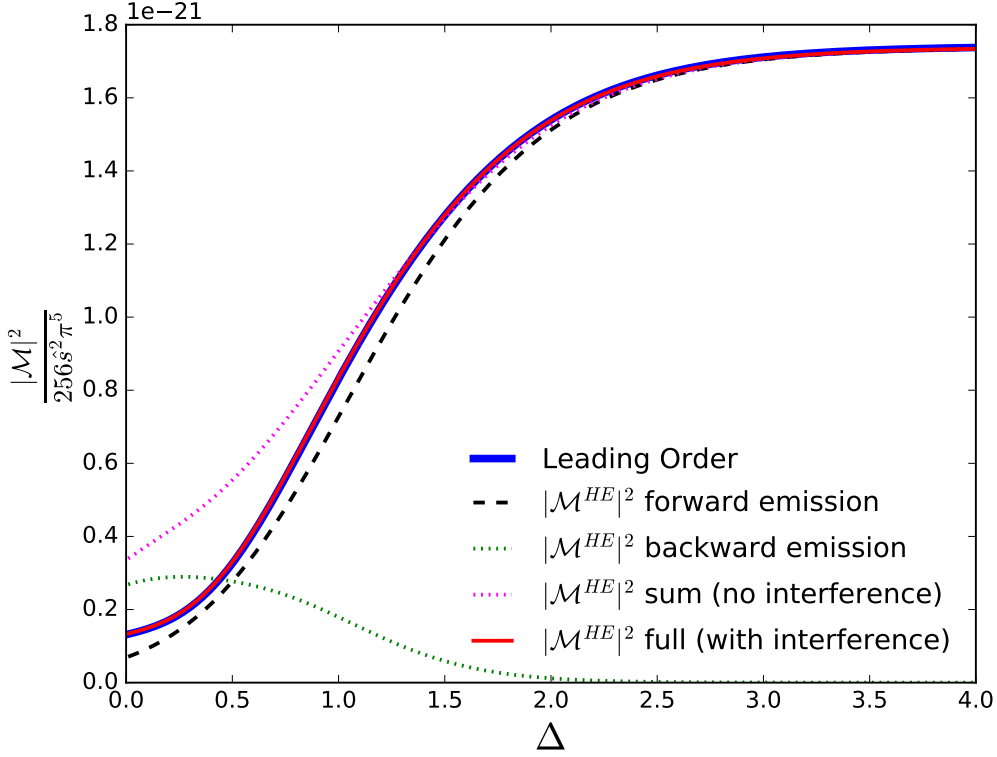


Figure 4.3: The matrix-element squared divided by the square of the partonic centre-of-mass energy for  $qQ \rightarrow ZqQ$  with the  $Z$  decaying to an electron-positron pair for the phase space slice described in eqn. (4.5). Increasing values of  $\Delta$  represent increasing rapidity separation between the jets. The different lines show the contributions from different terms in the calculation: only emission from the forward or the backward quark line (black, dashed and green, dotted), their sum without the interference term (magenta, dotted) and their sum including interference (red, solid) which is seen to agree exactly with the LO result (blue, thick solid).

Then upon squaring eqn. (4.8) we will automatically include the interference terms from the cross-terms. The inclusion of the virtual photon terms is particularly important when studying a combined lepton invariant mass,  $(p_{e^+} + p_{e^-})^2$ , far from the  $Z$  Breit-Wigner mass peak. This can be seen in fig. (4.4), where slices through phase space are shown similarly to fig. (4.3), but now for an (a) lower and (b) higher value of the di-lepton mass. In both cases, the contribution of the virtual photon processes is above 25%.

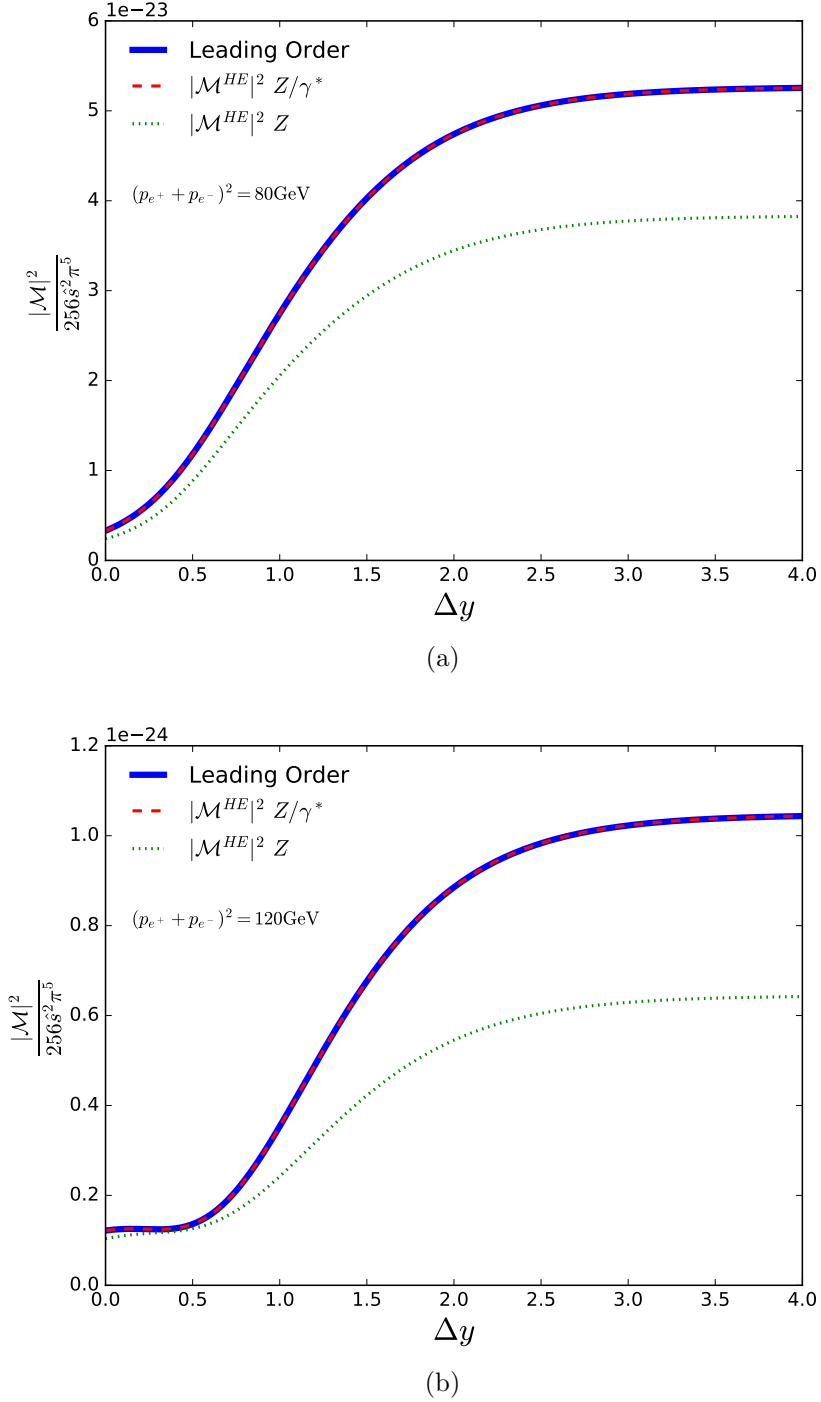


Figure 4.4: The matrix-element squared divided by the square of the partonic centre-of-mass energy for  $qQ \rightarrow Z/\gamma^* qQ$  with the  $Z/\gamma^*$  decaying to an electron-positron pair. The  $\mathcal{O}(\alpha_s^2 \alpha_W)$  tree-level contribution as described in HEJ (red, dashed) exactly matches that of **MadGraph5** (blue, solid). The terms corresponding to the production of a  $Z$  boson only (green, dotted) significantly undershoots the full result. The virtual photon terms are, therefore, clearly an important contribution to the matrix element away from the  $Z$  Breit-Wigner peak.

#### 4.2.4 The $2 \rightarrow n$ Matrix Element

Armed with eqn. (4.8) we can extend eqn. (4.4) in the obvious way to form a complete matrix element for the emission of a  $Z/\gamma^*$  boson. We can also describe the various possibilities ( $qq$ ,  $qg$  and  $gq$ ) simply by substituting the currents which apply in any given situation. Of course, in practice we use the importance sampling techniques discussed in chapter 3 to randomly sample the possible incoming parton types and so all combinations of currents are included.

Following in the vein of the previous chapter we now look to extend our description to higher multiplicity final states. Based on eqn. (3.65) from chapter 3 we can write the squared matrix element for  $qQ \rightarrow (Z/\gamma^* \rightarrow) e^+ e^- q(n-2)gQ$  is:

$$|\mathcal{M}_{qQ \rightarrow Z/\gamma^* q(n-2)gQ}^t|^2 = \frac{g_s^{2n} C_F}{8N_c} \times \left( \begin{aligned} & \frac{|j_a^{Z/\gamma^*} \cdot j_b|^2}{t_{a1} t_{a(n-1)}} \prod_{i=1}^{n-2} \frac{-C_A V^2(q_{ai}, q_{a(i+1)})}{t_{ait} t_{a(i+1)}} \\ & + \frac{|j_a \cdot j_b^{Z/\gamma^*}|^2}{t_{b1} t_{b(n-1)}} \prod_{i=1}^{n-2} \frac{-C_A V^2(q_{bi}, q_{b(i+1)})}{t_{bit} t_{b(i+1)}} \\ & - \frac{2\Re\{(j_a^{Z/\gamma^*} \cdot j_b)(\overline{j_a \cdot j_b^{Z/\gamma^*}})\}}{\sqrt{t_{a1} t_{b1}} \sqrt{t_{a(n-1)} t_{b(n-1)}}} \prod_{i=1}^{n-2} \frac{C_A V(q_{ai}, q_{a(i+1)}) \cdot V(q_{bi}, q_{b(i+1)})}{\sqrt{t_{ait} t_{bi}} \sqrt{t_{a(i+1)} t_{b(i+1)}}} \end{aligned} \right). \quad (4.9)$$

In the case of  $n = 2$ , this reduces back to eqn. (4.6). If either  $a$  or  $b$  is an incoming gluon then there are only two possible emission sites for the  $Z/\gamma^*$  once again and therefore we only need calculate one  $t$ -channel momenta chain and one can set the relevant  $j_a^{Z/\gamma^*}$  or  $j_b^{Z/\gamma^*}$  to zero in eqn. (4.6).

Eqn. (4.9) gives us the all-orders real corrections to  $Z/\gamma^*$  plus jets. However, before proceeding to calculate the cross-section we must carefully render eqn. (4.9) finite by including the virtual corrections whose divergences will cancel the pathologies in the effective vertices.

## 4.3 Regularising the $Z/\gamma^* + \text{Jets}$ Matrix Element

### 4.3.1 Real Soft Emissions

To calculate useful quantities such a cross sections etc. we must integrate equation eqn. (4.9) over all of phase space. However, as discussed in chapter 2 problems arise when we attempt to integrate over the soft regions of phase space. It is well understood that the divergences coming from soft real emissions cancel with those coming from soft virtual emissions and so we must explicitly show this cancellation and calculate the remaining finite contribution multiplying the  $(n - 1)$ -final state parton matrix element.

In the previous work on  $W^\pm$  emission the finite remainder from this cancellation was found to be [12, 15]:

$$\frac{\alpha_s C_a \Delta_{j-1,j+1}}{\pi} \ln \frac{\lambda_{cut}^2}{|\vec{q}_{j\perp}|^2}, \quad (4.10)$$

where  $\Delta_{i-1,i+1}$  is the rapidity span of the final state partons either side of our soft emission and  $|\vec{q}_{j\perp}|^2$  is the sum of squares of the transverse components of the  $j^{th}$   $t$ -channel gluon momenta.  $\lambda_{cut}$  is a parameter we choose which *defines* the soft region. I.e. any real emission satisfying  $p^2 \geq \lambda_{cut}^2$  we consider a hard perturbative emission while any emission with  $p^2 < \lambda_{cut}^2$  we consider too soft to be resolved.

Here we investigate the cancellation of these divergences for  $Z$  emission and most importantly whether the finite term is of the same form for the interference term which was previously excluded.

We start by looking at a  $2 \rightarrow n$  process and take the limit of one final state parton momentum,  $p_i$ , becoming small. Because of the form of eqn. (4.9) this amounts to looking at the effect of an external gluon becoming soft on our expression for the effective vertex for real emissions.

We can immediately see that for  $p_i$  going soft the gluon ‘chain’ momenta going into, and coming out of, the  $j^{th}$  emission site will coincide:  $q_{j+1} \sim q_j$ :

$$V^\rho(q_j, q_{j+1}) \rightarrow -2q_j^\rho - 2 \left( \frac{s_{aj}}{s_{ab}} - \frac{q_j^2}{s_{bj}} \right) p_b^\rho + 2 \left( \frac{s_{bj}}{s_{ab}} + \frac{q_j^2}{s_{aj}} \right) p_a^\rho \quad (4.11)$$

In eqn. (4.9) we have three terms involving the effective vertex; quadratic terms like  $V^2(q_{tj}, q_{t(j+1)})$  and  $V^2(q_{bj}, q_{b(j+1)})$  and interference terms like  $V(q_{tj}, q_{t(j+1)}) \cdot V(q_{bj}, q_{b(j+1)})$ . The procedure for the  $V^2$  terms follows similarly for both the quadratic

top-line emission and bottom-line emission terms and so only the calculation for top-line emission is shown here.

### $V^2(q_{tj}, q_{t(j+1)})$ Terms

Once we square eqn. (4.11) and impose the on-shell conditions for  $p_a$  and  $p_b$  we get:

$$V^2(q_{tj}, q_{tj}) = 4q_j^2 + 8q_j \cdot p_b \left( \frac{s_{aj}}{s_{ab}} - \frac{q_j^2}{s_{bj}} \right) - 8q_j \cdot p_a \left( \frac{s_{bj}}{s_{ab}} + \frac{q_j^2}{s_{aj}} \right) \quad (4.12)$$

$$- 4s_{ab} \left( \frac{s_{aj}}{s_{ab}} - \frac{q_j^2}{s_{bj}} \right) \left( \frac{s_{bj}}{s_{ab}} + \frac{q_j^2}{s_{aj}} \right). \quad (4.13)$$

Since  $p_j \rightarrow 0$  the dot-products  $s_{aj}$  and  $s_{bj}$  will also become vanishingly small and therefore:

$$V^2(q_{tj}, q_{tj}) = 4q_j^2 + 8q_j \cdot p_b \frac{q_j^2}{s_{bj}} - 8q_j \cdot p_a \frac{q_j^2}{s_{aj}} - 4s_{ab} \frac{q_j^4}{s_{bj}s_{aj}}. \quad (4.14)$$

Clearly the final term now dominates due to its  $\sim \frac{1}{p_i^2}$  behaviour and so in the soft limit we have:

$$V^2(q_{ti}, q_{ti}) = -\frac{4s_{ab}}{s_{bi}s_{ai}} q_i^4 + \mathcal{O}\left(\frac{1}{|p_i|}\right). \quad (4.15)$$

We must now explicitly calculate the invariant mass terms. Since we are in the High Energy regime we may take:

$$p_a \sim p_1 = p_+ = \left( \frac{1}{2}p_z, 0, 0, \frac{1}{2}p_z \right), \quad (4.16)$$

and,

$$p_b \sim p_n = p_- = \left( \frac{1}{2}p_z, 0, 0, -\frac{1}{2}p_z \right). \quad (4.17)$$

We describe our soft gluon with  $p_i = (E, \vec{p})$  and therefore we may express the products of momenta as follows:

$$s_{ai} = 2p_a \cdot p_i \sim 2p_+ \cdot p_i = \frac{1}{2}p_z E - \frac{1}{2}p_z^2, \quad (4.18)$$

$$s_{bi} = 2p_b \cdot p_i \sim 2p_- \cdot p_i = \frac{1}{2}p_z E + \frac{1}{2}p_z^2, \quad (4.19)$$

$$s_{ab} = \frac{1}{2}p_z^2. \quad (4.20)$$

Using these to extract the leading divergence in eqn. (4.15) we get:

$$V^2(q_{ti}, q_{ti}) = -\frac{4p_z^2}{(p_z E - p_z^2)(p_z E + p_z^2)} q_i^4 + \mathcal{O}\left(\frac{1}{|p_i|}\right), \quad (4.21a)$$

$$V^2(q_{ti}, q_{ti}) = -\frac{4p_z^2}{p_z^2(E^2 - p_z^2)} q_i^4 + \mathcal{O}\left(\frac{1}{|p_i|}\right), \quad (4.21b)$$

but since  $E^2 - \vec{p}_1^2 = 0$  for the on-shell external parton this can be written as:

$$V^2(q_{ti}, q_{ti}) = -\frac{4}{|\vec{p}_{1\perp}|^2} q_i^4 + \mathcal{O}\left(\frac{1}{|p_i|}\right), \quad (4.22)$$

Now looking back to eqn. (4.9) we see that each vertex is associated with factors of  $q_{ti}^{-2} q_{t(i+1)}^{-2}$  but since the emission is soft this becomes  $q_{ti}^{-4}$ . That factor conspires to cancel with the corresponding factor in eqn. (4.22). Including the addition factors of  $C_A$  and  $g_s$  and dropping any sub-leading divergences, the finite factor remaining is given by:

$$\frac{4C_A g_s^2}{|\vec{p}_{1\perp}|^2}, \quad (4.23)$$

### $V(q_{ti}, q_{t(i+1)}) \cdot V(q_{bi}, q_{b(i+1)})$ Terms

The calculation of the interference term with a soft emission follows similarly to that in above section. After taking  $p_i \rightarrow 0$  and taking the dot-product of the two vertex terms together we have:

$$\begin{aligned} V(q_{ti}, q_{ti}) \cdot V(q_{bi}, q_{bi}) &= 4q_i^t \cdot q_i^b - 4q_i^t \cdot p_a \left( \frac{s_{bi}}{s_{ab}} + \frac{t_i^b}{s_{ai}} \right) + 4q_i^t \cdot p_b \left( \frac{s_{ai}}{s_{ab}} + \frac{t_i^b}{s_{bi}} \right) \\ &\quad - 4q_i^b \cdot p_a \left( \frac{s_{bi}}{s_{ab}} + \frac{t_i^t}{s_{ai}} \right) + 4q_i^b \cdot p_b \left( \frac{s_{ai}}{s_{ab}} + \frac{t_i^t}{s_{bi}} \right), \end{aligned} \quad (4.24)$$

having simplified the expression using  $p_a^2 = 0$  and  $p_b^2 = 0$  once again. We may drop all the terms with  $s_{ai}$  or  $s_{bi}$  in the denominator and this time we are left with two terms which contribute. They combine to give:

$$V(q_{ti}, q_{ti}) \cdot V(q_{bi}, q_{bi}) = -\frac{s_{ab}}{s_{ai}s_{bi}} t_i^t t_i^b + \mathcal{O}\left(\frac{1}{|p_i|}\right). \quad (4.25)$$

The invariant mass terms here are identical to those we saw in the  $V^2$  terms and the products of  $t_i^t t_i^b$  also appear in the denominator of the interference term in eqn. (4.9). After this cancelling we are left with exactly what we had before (see eqn. (4.23)). Since exactly the same factor comes from all three terms at the amplitude squared level we may factor them out and express the amplitude squared for an  $n$ -parton final state with one soft emission in terms of an  $(n-1)$ -parton final state amplitude squared multiplied by a common factor:

$$\lim_{p_i \rightarrow 0} |\mathcal{A}_{Z/\gamma}^{2 \rightarrow n}|^2 = \left( \frac{4C_A g_s^2}{|\vec{p}_{i\perp}|^2} \right) |\mathcal{A}_{Z/\gamma}^{2 \rightarrow (n-1)}|^2 \quad (4.26)$$

### Integration of Soft Divergences

As mentioned above the divergences contained in eqn. (4.26) only become apparent after we have attempted to integrate over phase space. The Lorentz invariant phase space integral associated with  $p_i$  is given by:

$$\int \frac{d^3 \vec{p}_i}{(2\pi)^3 2E_i} \frac{4C_A g_s^2}{|\vec{p}_{i\perp}|^2}. \quad (4.27)$$

It is convenient to replace the integral over the  $z$ -component of momentum with one over rapidity,  $y_2$ . Rapidity and transverse momentum are related through the definition of rapidity given in eqn. (3.2). The Jacobian of this transformation is given by:

$$\frac{dy}{dp_z} = \frac{1}{2(E+p_z)} \frac{\partial}{\partial p_z}(E+p_z) - \frac{1}{2(E-p_z)} \frac{\partial}{\partial p_z}(E-p_z), \quad (4.28)$$

$$= \frac{E}{E^2 - p_z^2} - \frac{p_z}{E^2 - p_z^2} \frac{\partial E}{\partial p_z}, \quad (4.29)$$

$$= \frac{E}{E^2 - p_z^2} - \frac{p_z}{E^2 - p_z^2} \frac{p_z}{E}, \quad (4.30)$$

$$= \frac{1}{E}, \quad (4.31)$$

and therefore the rewritten phase space integral then reads:

$$\int_{\lambda_{\text{cut}}} \frac{d^{2+2\epsilon} \vec{p}_\perp}{(2\pi)^{2+2\epsilon}} \frac{dy}{4\pi} \frac{4C_A g_s^2}{|\vec{p}_\perp|^2} \mu^{-2\epsilon} = \frac{4C_A g_s^2 \mu^{-2\epsilon}}{(2\pi)^{2+2\epsilon} 4\pi} \Delta_{i-1,i+1} \int_{\lambda_{\text{cut}}} \frac{d^{2+2\epsilon} \vec{p}_\perp}{|\vec{p}_\perp|^2}, \quad (4.32)$$

where we have analytically continued the integral to  $2 + 2\epsilon$  dimensions to regulate the anticipated divergences and introduced the parameter  $\mu$  to keep the coupling dimensionless in the process. We have also introduced a lower bound on the transverse momentum integration of  $\lambda_{\text{cut}}$  - this parameter will be discussed in more detail later. Converting to polar coordinates and using the result for the volume of a unit hypersphere gives to integrated soft contribution:

$$\frac{4C_A g_s^2}{(2\pi)^{2+2\epsilon} 4\pi} \Delta_{i-1,i+1} \frac{1}{\epsilon} \frac{\pi^{1+\epsilon}}{\Gamma(\epsilon+1)} \left( \frac{\lambda_{\text{cut}}^2}{\mu^2} \right)^\epsilon. \quad (4.33)$$

As promised eqn. (4.33) is clearly divergent in the limit where  $\epsilon \rightarrow 0$ .

### 4.3.2 Virtual Emissions

As discussed in chapter 3 the virtual emission diagrams are included using the Lipatov ansatz for the gluon propagator:

$$\frac{1}{q_i^2} \longrightarrow \frac{1}{q_i^2} e^{\hat{\alpha}(q_i) \Delta_{i,i-1}}, \quad (4.34)$$

where:

$$\hat{\alpha}(q_i) = \alpha_s C_A q_i^2 \int \frac{d^{2+2\epsilon} k_\perp}{(2\pi)^{2+2\epsilon}} \frac{1}{k_\perp^2 (k_\perp - q_{i\perp})^2} \mu^{-2\epsilon}. \quad (4.35)$$

To see the cancellation of the infrared  $\epsilon$  poles we must perform the integral explicitly using dimensional regularisation. Using Feynman parameters to re-express eqn. (??):

$$\hat{\alpha}(q_i) = \alpha_s C_A q_i^2 \int \frac{d^{2+2\epsilon} k_\perp}{(2\pi)^{2+2\epsilon}} \int_0^1 \frac{dx}{[x(k - q_i)_\perp^2 + (1-x)k_\perp^2]^2} \mu^{-2\epsilon}, \quad (4.36)$$

$$= \alpha_s C_A q_i^2 \int \frac{d^{2+2\epsilon} \hat{k}_\perp}{(2\pi)^{2+2\epsilon}} \int_0^1 \frac{dx}{[\hat{k}_\perp^2 + q_{i\perp}^2 (1-x)]^2} \mu^{-2\epsilon}, \quad (4.37)$$

where we have performed a change of variables to  $\hat{k}_\perp = k_\perp - x q_{i\perp}$ . Changing the order of integration we can perform the  $\hat{k}_\perp$  integral using the following result:

$$\int \frac{d^d k}{(2\pi)^d} \frac{1}{(k^2 - C)^\alpha} = \frac{1}{(4\pi)^{\frac{d}{2}}} \frac{\Gamma(\alpha - \frac{d}{2})}{\Gamma(\alpha)} \frac{(-1)^\alpha}{C^{\alpha - \frac{d}{2}}}, \quad (4.38)$$

to give:

$$\hat{\alpha}(q_i) = \alpha_s C_A q_i^2 \frac{\Gamma(1 - \epsilon)}{(4\pi)^{1+\epsilon}} (-q_{i\perp}^2)^{\epsilon-1} \int_0^1 dx (1-x)^{\epsilon-1}, \quad (4.39)$$

$$= -\frac{2g_s^2 C_A}{(4\pi)^{2+\epsilon}} \frac{\Gamma(1 - \epsilon)}{\epsilon} \left( \frac{q_{i\perp}^2}{\mu^2} \right)^\epsilon, \quad (4.40)$$

having completed the  $x$  integral and used the definition  $\alpha_s = \frac{g_s^2}{4\pi}$ .

### 4.3.3 Cancellation of Infrared Divergences

We now have all the necessary ingredients to show how the infrared contributions from soft real emissions and virtual emissions cancel leaving our integrated matrix element finite. The only subtlety being that we must sum two diagrams with different multiplicity final states to see the cancellation. This is because they are experimentally indistinguishable; the  $2 \rightarrow (n-1)$  virtual diagram has  $(n-1)$  resolvable partons in the final state and we only ‘see’  $(n-1)$  of the final states partons from  $2 \rightarrow n$  process because we consider one of the emissions too soft to resolve.

The matrix element squared for the real emission diagram with one soft parton will look like:

$$|\mathcal{A}_{Z/\gamma}^{2 \rightarrow n}|^2 = \left( \frac{4g_s^2 C_a}{|p_{i\perp}|^2} \right) \left[ \left| \mathcal{K}_a j_1^{Z/\gamma} \cdot j_2 \right|^2 \frac{\prod_{i \neq j}^{n-2} V^2(q_{ti}, q_{t(i+1)})}{\prod_{i \neq j}^{n-1} q_{ti}^2} + \dots \right] \quad (4.41)$$

$$\left| \mathcal{K}_b j_2^{Z/\gamma} \cdot j_1 \right|^2 \frac{\prod_{i \neq j}^{n-2} V^2(q_{bi}, q_{b(i+1)})}{\prod_{i \neq j}^{n-1} q_{bi}^2} + \dots \quad (4.42)$$

$$2\Re\{\mathcal{K}_a \overline{\mathcal{K}_b} \times (j_1^{Z/\gamma} \cdot j_2)(\overline{j_2^{Z/\gamma} \cdot j_1})\} \quad (4.43)$$

$$\times \frac{\prod_{i \neq j}^{n-2} V(q_{ti}, q_{t(i+1)}) \cdot V(q_{bi}, q_{b(i+1)})}{\prod_{i \neq j}^{n-1} q_{ti} q_{bi}} \Big], \quad (4.44)$$

where we have taken the  $i^{th}$  gluon to be soft.

After including the virtual corrections via the insertion of the Lipatov ansatz the  $2 \rightarrow (n-1)$  matrix element squared is:

$$|\mathcal{A}_{Z/\gamma}^{2 \rightarrow (n-1)}|^2 = \left| \mathcal{K}_a j_1^{Z/\gamma} \cdot j_2 \right|^2 \frac{\prod_i^{n-3} V^2(q_{ti}, q_{t(i+1)})}{\prod_i^{n-2} q_{ti}^2} e^{2\hat{\alpha}(q_{ti})\Delta_{i-1,i+1}} + \dots \quad (4.45)$$

$$\left| \mathcal{K}_b j_2^{Z/\gamma} \cdot j_1 \right|^2 \frac{\prod_i^{n-3} V^2(q_{bi}, q_{b(i+1)})}{\prod_i^{n-2} q_{bi}^2} e^{2\hat{\alpha}(q_{bi})\Delta_{i-1,i+1}} + \dots \quad (4.46)$$

$$2\Re\{\mathcal{K}_a \overline{\mathcal{K}_b} \times (j_1^{Z/\gamma} \cdot j_2)(\overline{j_2^{Z/\gamma} \cdot j_1})\} \quad (4.47)$$

$$\times \frac{\prod_i^{n-3} V(q_{ti}, q_{t(i+1)}) \cdot V(q_{bi}, q_{b(i+1)})}{\prod_i^{n-2} q_{ti} q_{bi}} e^{(\hat{\alpha}(q_{bi}) + \hat{\alpha}(q_{ti}))\Delta_{i-1,i+1}}, \quad (4.48)$$

We can now go through term-by-term to show the divergences cancel and find the finite contribution to the matrix element squared.

Similarly to when we calculated the soft terms the arguments for the pure top- and bottom-line emissions follow similarly and so here we will only state the procedure for the top emission.

For the top line emission we identify the following terms that will appear in the sum of the  $2 \rightarrow (n-1)$  virtual and  $2 \rightarrow n$  real matrix elements. This finite contribution to the matrix element is given by:

$$\mathcal{F}_{\text{top}} = \frac{4C_A g_s^2}{(2\pi)^{2+2\epsilon} 4\pi} \Delta_{i-1,i+1} \frac{1}{\epsilon} \frac{\pi^{1+\epsilon}}{\Gamma(\epsilon+1)} \left( \frac{\lambda_{cut}^2}{\mu^2} \right)^\epsilon + e^{2\hat{\alpha}(q_{ti})\Delta_{i-1,i+1}}. \quad (4.49)$$

Extract the relevant power of the strong coupling order from the exponential and substituting for  $\hat{\alpha}(q_i)$  gives:

$$\mathcal{F}_{\text{top}} = \frac{4C_A g_s^2}{(2\pi)^{2+2\epsilon} 4\pi} \Delta_{i-1,i+1} \frac{1}{\epsilon} \frac{\pi^{1+\epsilon}}{\Gamma(\epsilon+1)} \left( \frac{\lambda_{cut}^2}{\mu^2} \right)^\epsilon - \frac{2g_s^2 C_A}{(4\pi)^{2+\epsilon}} \frac{\Gamma(1-\epsilon)}{\epsilon} \left( \frac{q_{ti\perp}^2}{\mu^2} \right)^\epsilon, \quad (4.50)$$

$$= \frac{g_s^2 C_A}{4^{1+\epsilon} \pi^{2+\epsilon}} \Delta_{i-1,i+1} \left( \frac{1}{\epsilon \Gamma(1+\epsilon)} \left( \frac{\lambda_{cut}^2}{\mu^2} \right)^\epsilon - \frac{\Gamma(1-\epsilon)}{\epsilon} \left( \frac{q_{ti\perp}^2}{\mu^2} \right)^\epsilon \right). \quad (4.51)$$

Expanding the terms involving the regularisation parameter for small values,  $\epsilon \rightarrow 0$ , yields:

$$\mathcal{F}_{\text{top}} = \frac{\alpha_s C_A \Delta_{i-1,i+1}}{\pi} \ln \left( \frac{\lambda_{\text{cut}}^2}{q_{ti\perp}^2} \right), \quad (4.52)$$

where we have used:

$$\frac{1}{\Gamma(1+\epsilon)} = 1 + \gamma_E \epsilon + \mathcal{O}(\epsilon^2), \quad \Gamma(1-\epsilon) = 1 + \gamma_E \epsilon + \mathcal{O}(\epsilon^2), \quad \left( \frac{x}{y} \right)^\epsilon = 1 + \epsilon \ln \left( \frac{x}{y} \right) + \mathcal{O}(\epsilon^2). \quad (4.53)$$

Similarly, for the terms arising from the bottom quark-line emission we have:

$$\mathcal{F}_{\text{bottom}} = \frac{\alpha_s C_A \Delta_{i-1,i+1}}{\pi} \ln \left( \frac{\lambda_{\text{cut}}^2}{q_{bi\perp}^2} \right) \quad (4.54)$$

Lastly, for the interference terms we expand the exponential with both top-line emission,  $q_{ti}$ , momenta and bottom-line emission,  $q_{bi}$ , momenta to get a:

$$\begin{aligned} \mathcal{F}_{\text{interf.}} &= \frac{g_s^2 C_A \Delta_{i-1,i+1}}{4^{1+\epsilon} \pi^{2+\epsilon}} \left( \left( \frac{1}{\epsilon} + \gamma_E + \ln \left( \frac{\lambda_{\text{cut}}^2}{\mu^2} \right) + \mathcal{O}(\epsilon) \right) - \right. \\ &\quad \left. \frac{1}{2} \left[ \frac{2}{\epsilon} + 2\gamma_E + \ln \left( \frac{q_{ti\perp}^2}{\mu^2} \right) - \ln \left( \frac{q_{bi\perp}^2}{\mu^2} \right) + \mathcal{O}(\epsilon) \right] \right) \quad (4.55) \\ &= \frac{\alpha_s C_A \Delta_{i-1,i+1}}{\pi} \ln \left( \frac{\lambda_{\text{cut}}^2}{\sqrt{q_{ti\perp}^2 q_{bi\perp}^2}} \right). \end{aligned}$$

Eqn. 4.55 is a new result which allows the inclusion of the interference terms shown to be important in previous discussion. We can now express the regulated  $qQ \rightarrow Z/\gamma^* q(n-2)gQ$  matrix element as follows:

$$\begin{aligned}
 |\mathcal{M}_{qQ \rightarrow Z/\gamma^* q(n-2)gQ}^{HEJ-\text{reg}}|^2 = & g_s^2 \frac{C_F}{8N_c} (g_s^2 C_A)^{n-2} \\
 & \times \left( \frac{|j_a^{Z/\gamma^*} \cdot j_b|^2}{t_{a1} t_{a(n-1)}} \exp(\omega^0(q_{a(n-1)\perp}) \Delta y_{n-1}) \prod_{i=1}^{n-2} \frac{-V^2(q_{ai}, q_{a(i+1)})}{t_{ait} t_{a(i+1)}} \exp(\omega^0(q_{ai\perp}) \Delta y_i) \right. \\
 & + \frac{|j_a \cdot j_b^{Z/\gamma^*}|^2}{t_{b1} t_{b(n-1)}} \exp(\omega^0(q_{b(n-1)\perp}) \Delta y_{n-1}) \prod_{i=1}^{n-2} \frac{-V^2(q_{bi}, q_{b(i+1)})}{t_{bit} t_{b(i+1)}} \exp(\omega^0(q_{bi\perp}) \Delta y_i) \\
 & - \frac{2\Re\{(j_a^{Z/\gamma^*} \cdot j_b)(\overline{j_a \cdot j_b^{Z/\gamma^*}})\}}{\sqrt{t_{a1} t_{b1}} \sqrt{t_{a(n-1)} t_{b(n-1)}}} \exp(\omega^0(\sqrt{q_{a(n-1)\perp} q_{b(n-1)\perp}}) \Delta y_{n-1}) \\
 & \left. \prod_{i=1}^{n-2} \frac{V(q_{ai}, q_{a(i+1)}) \cdot V(q_{bi}, q_{b(i+1)})}{\sqrt{t_{ait} t_{bi}} \sqrt{t_{a(i+1)} t_{b(i+1)}}} \exp(\omega^0(\sqrt{q_{ai\perp} q_{bi\perp}}) \Delta y_i) \right), \tag{4.56}
 \end{aligned}$$

where we have defined

$$\omega^0(q_\perp^2) = -\frac{g_s^2 C_A}{4\pi^2} \log\left(\frac{q_\perp^2}{\lambda_{cut}^2}\right). \tag{4.57}$$

There is one final improvement we can make to eqn. (4.56). The expressions we obtain upon taking the soft limit of the three effective vertex terms,  $V_t^2$ ,  $V_b^2$  and  $V_t \cdot V_b$ , are not exact and there are sub-leading terms which we can account for. We therefore have to account for the difference between, e.g  $-V^2(q_{i-1}, q_i)/(t_{i-1} t_i)$ , and its strict limit of  $4/p_{i\perp}^2$  for values of  $p_{i\perp}$  below  $\lambda_{cut}$ . In practice, we include this correction for  $c_{cut} < |p_\perp| < \lambda_{cut}$  with  $c_{cut} = 0.2$  GeV and find stable results around this value (see section 4.4).

We are, at last, in a position to move forward and form an expression for an all-orders gauge invariant *finite* matrix element for  $Z/\gamma^*$  plus jets. Before pressing on we now discuss one final example calculation showing explicitly the finite nature of our matrix element expression.

#### 4.3.4 Example: $2 \rightarrow 3$ Scattering

Consider the case of  $2 \rightarrow 3$  where the  $p_2$  momentum has become soft. A contributing soft diagram is shown in fig. (4.5a) and one example of a contributing virtual diagram of the same order is shown in fig. (4.5b). When  $p_2$  goes soft we have the following form

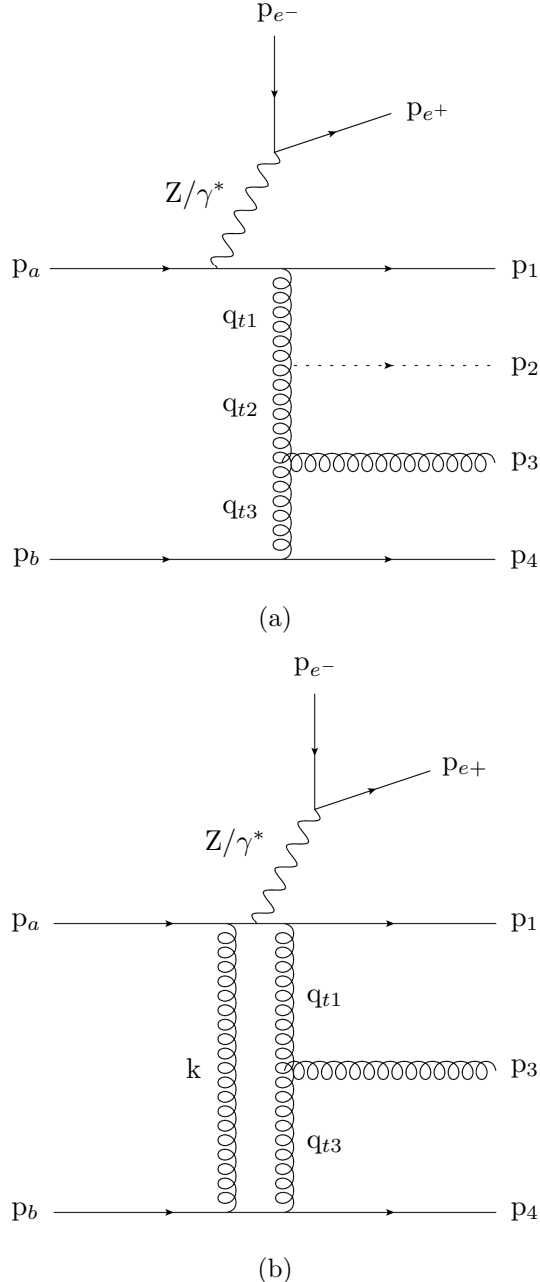


Figure 4.5: Examples of both real and virtual diagrams contributing to  $2 \rightarrow 3$  scattering. In fig. (4.5a) the  $p_2$  has been drawn with a dashed line to denote it is not resolvable. In fig. (4.5b) the final state momenta have been labelled in a seemingly strange way - this was done to make clear the cancellation when working through the algebra.

for the  $2 \rightarrow 3$  integrated amplitude squared (N.B.: The integration is only schematic and doesn't represent the full Lorentz invariant phase space):

$$\begin{aligned} \int dPS |\mathcal{A}_{soft}^{2 \rightarrow 3}|^2 = & \frac{4C_A g_s^2 \Delta_{1,3}}{(2\pi)^{2+2\epsilon} 4\pi} \frac{\pi^{\epsilon+1}}{\epsilon \Gamma(\epsilon+1)} \left( \frac{\lambda_{cut}^2}{\mu^2} \right)^\epsilon \left[ |\mathcal{K}_a j_1^Z \cdot j_2|^2 \frac{V^2(q_{t1}, q_{t3})}{q_{t1}^2 q_{t3}^2} \right. \\ & \left. + |\mathcal{K}_b j_1 \cdot j_2^Z|^2 \frac{V^2(q_{b1}, q_{b3})}{q_{b1}^2 q_{b3}^2} + 2\Re \left\{ \mathcal{K}_a \overline{\mathcal{K}_b} (j_1^Z \cdot j_2) \overline{(j_1 \cdot j_2^Z)} \right\} \frac{V(q_{t1}, q_{t3}) \cdot V(q_{b1}, q_{b3})}{q_{t1} q_{t3} q_{b1} q_{b3}} \right], \end{aligned} \quad (4.58)$$

and the virtual contributions for the  $2 \rightarrow 3$  amplitude is:

$$\begin{aligned} \int dPS |\mathcal{A}_{virtual}^{2 \rightarrow 3}|^2 = & |\mathcal{K}_b j_1 \cdot j_2^Z|^2 \frac{V^2(q_{t1}, q_{t3})}{q_{t1}^2} e^{2\hat{\alpha}(q_{t1}) \Delta_{1,3}} + \\ & |\mathcal{K}_t j_1^Z \cdot j_2|^2 \frac{V^2(q_{b1}, q_{b3})}{q_{b1}^2} e^{2\hat{\alpha}(q_{b1}) \Delta_{1,3}} + \\ & 2\Re \left\{ \mathcal{K}_a \overline{\mathcal{K}_b} (j_1^Z \cdot j_2) \overline{(j_1 \cdot j_2^Z)} \right\} \frac{V(q_{t1}, q_{t3}) \cdot V(q_{b1}, q_{b3})}{q_{t1} q_{t3} q_{b1} q_{b3}} e^{(\hat{\alpha}(q_{t1}) + \hat{\alpha}(q_{b1})) \Delta_{1,3}}. \end{aligned} \quad (4.59)$$

Once we expand the exponential to the correct order in  $g_s^2$ , the sum of these matrix elements squared over the region of phase space when  $p_2$  is soft is:

$$\begin{aligned} \int dPS (|\mathcal{A}_{soft}^{2 \rightarrow 3}|^2 + |\mathcal{A}_{virtual}^{2 \rightarrow 3}|^2) = & |\mathcal{K}_a j_1^Z \cdot j_2|^2 \frac{V^2(q_{t1}, q_{t3})}{q_{t1}^2} \left( \frac{4C_A g_s^2 \Delta_{1,3}}{(2\pi)^{2+2\epsilon} 4\pi} \frac{\pi^{\epsilon+1}}{\epsilon \Gamma(\epsilon+1)} - 2\hat{\alpha}(q_{t1}) \Delta_{1,3} \right) + \\ & |\mathcal{K}_b j_1 \cdot j_2^Z|^2 \frac{V^2(q_{b1}, q_{b3})}{q_{b1}^2} \left( \frac{4C_A g_s^2 \Delta_{1,3}}{(2\pi)^{2+2\epsilon} 4\pi} \frac{\pi^{\epsilon+1}}{\epsilon \Gamma(\epsilon+1)} - 2\hat{\alpha}(q_{b1}) \Delta_{1,3} \right) + \\ & 2\Re \left\{ \mathcal{K}_a \overline{\mathcal{K}_b} (j_1^Z \cdot j_2) \overline{(j_1 \cdot j_2^Z)} \right\} \frac{V(q_{t1}, q_{t3}) \cdot V(q_{b1}, q_{b3})}{q_{t1} q_{t3} q_{b1} q_{b3}} \\ & \left( \frac{4C_A g_s^2 \Delta_{1,3}}{(2\pi)^{2+2\epsilon} 4\pi} \frac{\pi^{\epsilon+1}}{\epsilon \Gamma(\epsilon+1)} - (\hat{\alpha}(q_{t1}) + \hat{\alpha}(q_{b1})) \Delta_{1,3} \right) + \mathcal{O}(g_s^4), \end{aligned} \quad (4.60)$$

These bracketed terms are exactly the cancellations calculated in section 4 above. Therefore:

$$\begin{aligned}
 \int dPS (|\mathcal{A}_{soft}^{2 \rightarrow 3}|^2 + |\mathcal{A}_{virtual}^{2 \rightarrow 3}|^2) = & \frac{\alpha_s C_A \Delta_{1,3}}{\pi} \left( |\mathcal{K}_a j_1^Z \cdot j_2|^2 \frac{V^2(q_{t1}, q_{t3})}{q_{t1}^2} \ln \left( \frac{\lambda_{cut}^2}{|q_{1t\perp}|^2} \right) + \right. \\
 & |\mathcal{K}_b j_1 \cdot j_2^Z|^2 \frac{V^2(q_{b1}, q_{b3})}{q_{b1}^2} \ln \left( \frac{\lambda_{cut}^2}{|q_{1b\perp}|^2} \right) + \\
 & 2\Re \left\{ \mathcal{K}_a \overline{\mathcal{K}_b} (j_1^Z \cdot j_2) \overline{(j_1 \cdot j_2^Z)} \right\} \frac{V(q_{t1}, q_{t3}) \cdot V(q_{b1}, q_{b3})}{q_{t1} q_{t3} q_{b1} q_{b3}} \\
 & \left. \ln \left( \frac{\lambda_{cut}^2}{\sqrt{|q_{1t\perp}|^2 |q_{1b\perp}|^2}} \right) \right) + \mathcal{O}(\alpha_s^2),
 \end{aligned} \tag{4.61}$$

Which is manifestly finite.

## 4.4 Subtractions and the $\lambda_{cut}$ scale

We now show the stability of the High Energy Jets predictions with respect to the  $\lambda_{cut}$  scale described above.

We increase our sensitivity to the parameter by showing results for FKL momentum configurations only. The non-FKL samples which are added to give the total cross sections have no dependence on  $\lambda_{cut}$  and would therefore dilute any dependence in the full sample. We begin in table 4.1 where we show the value of the cross section for different values of  $\lambda_{cut}$  for exclusive 2-, 3- and 4-jet samples. The cuts applied are the same as in section ???. It is clear that the cross section does not display a large dependence on the value of  $\lambda_{cut}$ .

$\lambda_{cut}$ (GeV)	$\sigma(2j)$ (pb)	$\sigma(3j)$ (pb)	$\sigma(4j)$ (pb)
0.2	$5.03 \pm 0.02$	$0.70 \pm 0.02$	$0.13 \pm 0.03$
0.5	$5.05 \pm 0.01$	$0.70 \pm 0.01$	$0.13 \pm 0.01$
1.0	$5.09 \pm 0.01$	$0.71 \pm 0.01$	$0.13 \pm 0.01$
2.0	$5.16 \pm 0.04$	$0.72 \pm 0.01$	$0.13 \pm 0.01$

Table 4.1: The FKL-only cross sections for the 2-, 3- and 4-jet exclusive rates with associated statistical errors shown for different values of the regularisation parameter  $\lambda_{cut}$ . The scale choice was half the sum over all transverse scales in the event,  $H_T/2$ .

Figure 4.6 shows the effect of the same variation in  $\lambda_{cut}$  on the differential distribution in both the rapidity gap between the two leading jets in  $p_\perp$ ,  $\Delta y_{j1,j2}$ , (a)–(c), and the rapidity gap between the two extremal jets in rapidity,  $\Delta y_{jf,jb}$ , (d)–(f). Results are shown for exclusive 2-, 3- and 4-jet samples in each case, once again the cuts applied

are the same as in the ATLAS study presented in section 4.7.1. Again the scale choice for the central line was  $\mu_F = \mu_R = H_T/2$ . The variation bands have been determined by varying these two scales independently by up to a factor of two in either direction with the extremal points removed where the relative difference between  $\mu_F$  and  $\mu_R$  is greater than a factor of 2. The distributions also show a very weak dependence on the choice of  $\lambda_{cut}$ .

In practice, our default chosen value for  $\lambda_{cut}$  is 0.2.

## 4.5 The Differential $Z/\gamma$ Cross-Section

Starting from eqn. (4.56) we can write down a total (differential) cross section can then be obtained by summing over all values of  $n$  and integrating over the full  $n$ -particle phase space, using an efficient Monte Carlo sampling algorithm [12, 18]:

$$\begin{aligned} \sigma = & \sum_{f_a, f_b} \sum_{n=2}^{\infty} \int \frac{d^3 p_a}{(2\pi)^3 2E_a} \int \frac{d^3 p_b}{(2\pi)^3 2E_b} \left( \prod_{i=2}^n \int \frac{d^3 p_i}{(2\pi)^3 2E_i} \right) (2\pi)^4 \delta^{(4)} \left( p_a + p_b - \sum_i p_i \right) \\ & \times |\mathcal{M}_{f_a f_b \rightarrow Z/\gamma^* f_a(n-2) g f_b}^{HEJ-reg}(p_a, p_b, \{p_i\})|^2 \frac{x_a f_{f_a}(x_a, Q_a) x_b f_{f_b}(x_b, Q_b)}{\hat{s}^2} \Theta_{cut}, \end{aligned} \quad (4.62)$$

where  $x_{a,b}$  are the momentum fractions of the incoming partons and  $f_{f_k}(x_k, Q_k)$  are the corresponding parton density functions for beam, k, and flavour  $f_k$ . The factor of  $\hat{s}^2$  is the usual phase space factor. The function  $\Theta_{cut}$  term imposes any desired cuts on the final state. The minimum requirement is that the final state momenta cluster into at least two jets for the desired algorithm

In the regions of phase space where all final state particles are well separated in rapidity, this gives the dominant terms in QCD at all orders in  $\alpha_s$  (the leading logarithmic terms in  $s/t$ ). However, in other areas of phase space, the differences due to the approximations used in  $|\mathcal{M}_{qQ \rightarrow Z/\gamma^* q(n-2) g Q}^{HEJ-reg}|^2$  will become more significant. We can therefore further improve upon eq. (4.62) by matching our results to fixed order results. Here, we match to high-multiplicity tree-level results obtained from `Madgraph5` [9] in two different ways. This amounts to merging tree-level samples of different orders according to the logarithmic prescription of HEJ.

1. Matching for FKL configurations As described in section ??, these are the particle assignments and momentum configurations which contain the dominant leading-

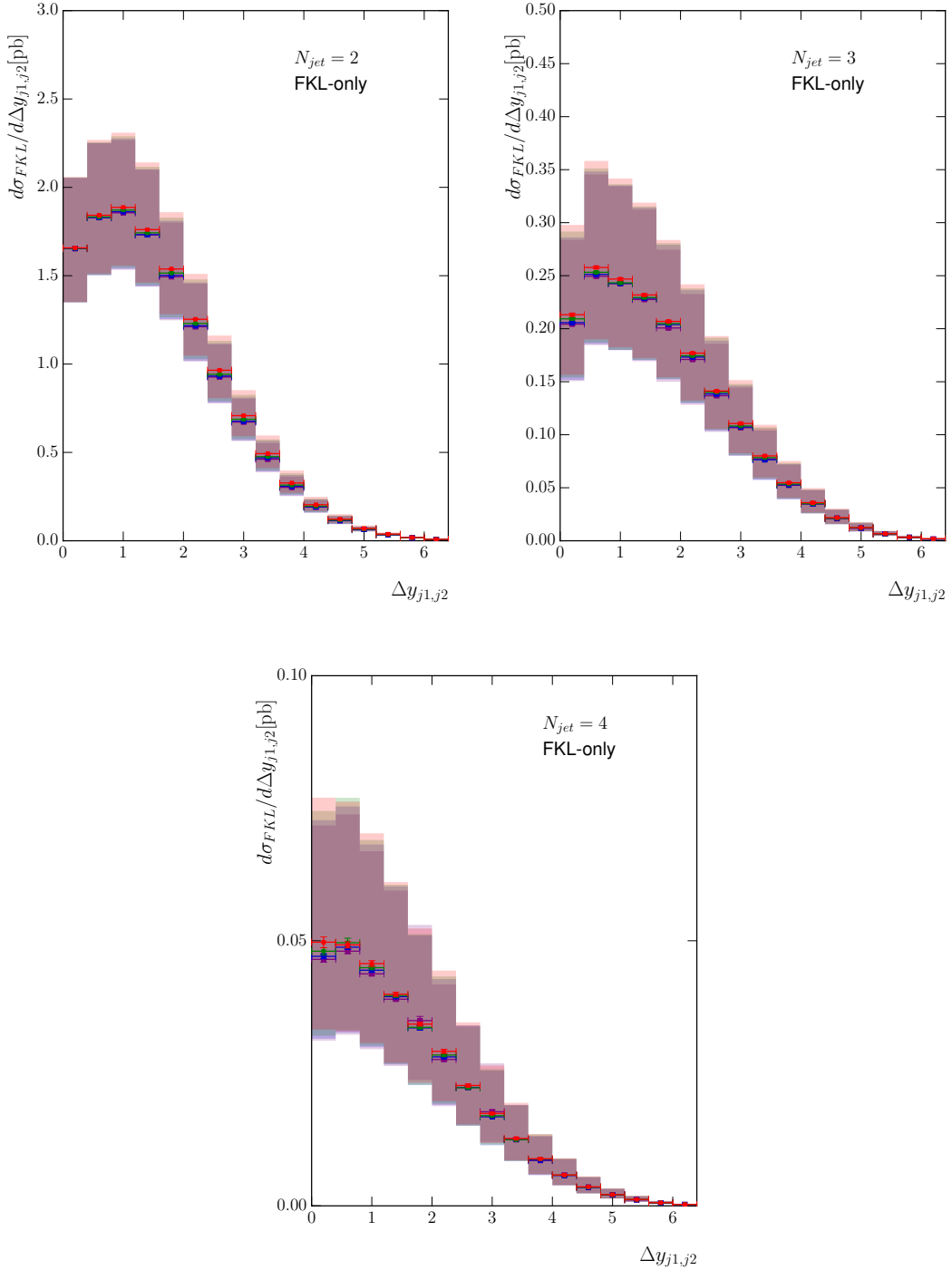


Figure 4.6: The effect of varying  $\lambda_{cut}$  on the differential distribution in the rapidity gap between the two leading jets in  $p_\perp$ ,  $\Delta y_{j1,j2}$ , with the  $N_{jet} = 2, 3, 4$  exclusive selections shown from left to right.  $\lambda_{cut} = 0.2$  (red),  $0.5$  (blue),  $1.0$  (green),  $2.0$  (purple). The bands represent the scale variation described in the text.

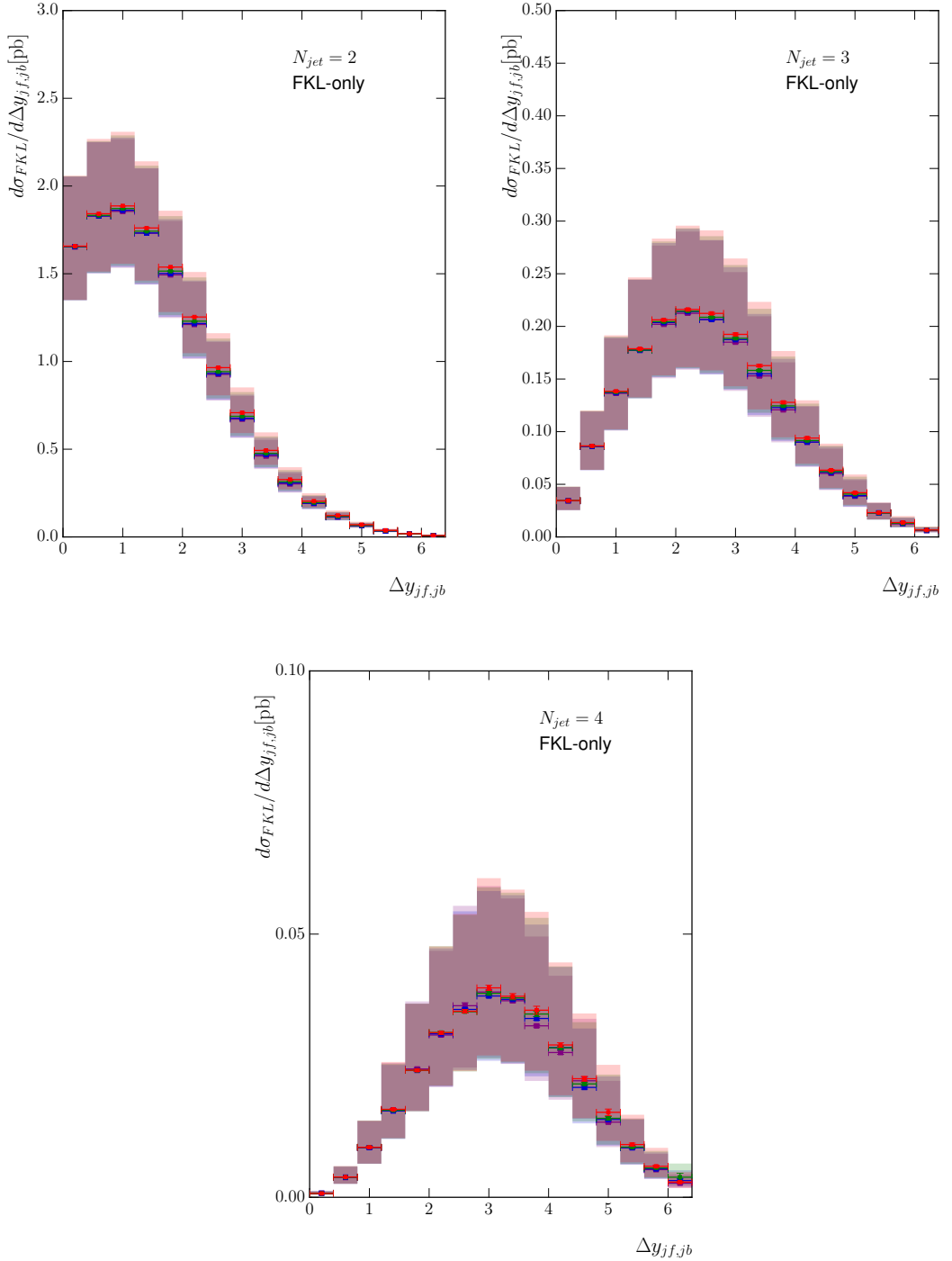


Figure 4.7: The effect of varying  $\lambda_{cut}$  on the differential distribution in the rapidity gap between the two extremal jets in rapidity,  $\Delta y_{jf,jb}$ , with the  $N_{jet} = 2, 3, 4$  exclusive selections shown from left to right.  $\lambda_{cut} = 0.2$  (red), 0.5 (blue), 1.0 (green), 2.0 (purple). The bands represent the scale variation described in the text.

logarithmic terms in  $s/t$ . The first step of the HEJ description was to develop an approximation to the matrix element for these processes which was later supplemented with the finite correction which remained after cancelling the real and virtual divergences:  $|\overline{\mathcal{M}}_{qg \rightarrow Zqg}^{HE}|^2$  (eq. (4.4)) or  $|\overline{\mathcal{M}}_{qQ \rightarrow ZqQ}^{HE}|^2$  (eq. (4.9)). The approximation is necessary to allow us to describe the matrix element for any (and in particular, large)  $n$  and for including both the leading real and virtual corrections. However, if the parton momenta cluster into four or fewer *jets* (These may have arisen from many more partons), the full tree-level matrix element remains calculable. In these cases, we perform the matching multiplicatively, so we multiply the integrand of eq. (4.62) by

$$|\mathcal{M}_{qQ \rightarrow Z/\gamma^* q(k-2)gQ}^{\text{full}}(p_a, p_b, \{j'_i\})|^2 / |\mathcal{M}_{qQ \rightarrow Z/\gamma^* q(k-2)gQ}^{HEJ}(p_a, p_b, \{j'_i\})|^2. \quad (4.63)$$

Here,  $\{j'_i\}$  are the jet momenta after a small amount of reshuffling. This is necessary because the evaluation of the tree-level matrix elements assumes that the jet momenta are both on-shell and have transverse momenta which sum to zero, neither of which is true in general for our events due to the presence of extra emissions. Our reshuffling algorithm [17] redistributes this extra transverse momentum in proportion to the size of the transverse momentum of each jet. The plus and minus light-cone components are then adjusted such that the jet is put on-shell and the rapidity remains unaltered. This last feature ensures that after reshuffling the event is still in an FKL configuration.

After this multiplicative matching factor has been included, the regularisation then proceeds as before.

## 2. Matching for non-FKL configurations

Away from regions in phase space where the quarks and gluons are well-separated, the non-FKL configurations will play a more significant rôle. These have so far not been accounted for at all, and hence we add three exclusive samples of leading-order two-jet, three-jet and four-jet leading-order events to our resummed events. The distinction between the samples is made following the choice of jet algorithm and parameters.

These two matching schemes complete our description of the production of  $Z/\gamma^*$  with at least two jets, including the leading high-energy logarithms at all orders in  $\alpha_s$ . In the next sections, we discuss the computational aspects of the work presented here and compare the resulting predictions from this formalism to LHC data from recent ATLAS

and CMS analyses.

## 4.6 $Z/\gamma^* + \text{Jets}$ : Computational Aspects

The physics presented in the preceding sections is a significant departure from work previously done by the High Energy Jets collaboration. As such developing the Monte Carlo for  $Z/\gamma^*$  plus jets was a serious undertaking; the inclusion of the aforementioned interference terms required that two  $t$ -channel ‘chains’ of momenta and vertices be computed. Furthermore to correctly calculate at the amplitude level the method in which we evaluate eqn. 4.3. Since the virtual corrections are scale dependent it was necessary to change large sections of code to work with multiple copies of  $t$ -chains and multiple scales.

In previous `HEJ` releases the matching mentioned above was performed using `MadGraph` version 4. However, due to increases in speed and efficiency we chose to match the  $Z/\gamma^* + \text{jets}$  `HEJ` matrix elements to `MadGraph` version 5. While this might seem like a trivial change the underlying computational work was anything but; since the latest version of `MadGraph` outputs matrix elements in C++ (rather than Fortran 90) a completely new approach to incorporating matching was required. A novel ‘abstract factory’ design pattern was employed to efficiently construct and call the relevant exact leading order matrix element. In this way we avoided the necessity of having extremely large matching files containing 18,000+ lines of code which was very difficult to debug and improve; instead this new structure allowed the matching code to be reduced to only a few thousand lines since the abstract factory class presents a uniform interface and therefore almost all of the process specific lines became unnecessary (some process specific content remains due to the distinction made between FKL and non-FKL configurations).

Throughout the course of this work it became apparent that the High Energy Jets codebase as it was at the time needed to be restructured. Each physics process (pure jets,  $W^\pm + \text{jets}$ , Higgs+jets and  $Z/\gamma^* + \text{jets}$ ) was structured individually as a stand-alone piece of code. This became a problem when testing and modifying `HEJ` since there are large sections of code which are the same regardless of what electroweak boson emission (if any) we are concerned with, for example the parton distribution function calls are almost entirely the same no matter which code is run. To improve upon this situation a unified `HEJ` package was created. This was a complete restructure of the code into a form in which a general `HejGen` polymorphic base class could be constructed abstractly and then made concrete depending on user input. The unified version of the code is an

improvement in that it is much more user friendly, and significantly easier to test and extend.

Lastly a word about the generation of High Energy Jets predictions for comparisons to data. The sections and chapters which follow contain theoretical predictions to experimental analyses. These predictions were generated using distributed computing both locally in Edinburgh and using the CERN GRID system. The former required the development of a set-up to distribute, execute and finalise jobs across a large network of machines standard desktop machines (i.e. not actual computing nodes) distributed through Edinburgh University. This was a time-consuming process however without this system it would not have been possible to produce the interesting results of chapter 5 (see chapter 5 for a discussion of the computational challenges of generating HEJ+ARIADNE predictions).<sup>1</sup> The GRID distributed computing work was available only in the final stages of this work (had it been available sooner the aforementioned local distributed computing set-up could have been avoided completely). This involved a good deal of learning to work with (properly) distributed systems and working with the `Ganga` batch submission system which was, again, time-consuming.

## 4.7 $Z/\gamma^* + \text{Jets}$ at the LHC

### 4.7.1 $Z/\gamma^* + \text{Jets}$ at the ATLAS Experiment

We now compare the results of the formalism described in the previous sections to data. We begin with a recent ATLAS analysis of  $Z$ -plus-jets events from 7 TeV collisions [1]. We summarise the cuts in the following table:

Lepton Cuts	$p_{T\ell} > 20 \text{ GeV},  \eta_\ell  < 2.5$ $\Delta R^{\ell^+\ell^-} > 0.2, 66 \text{ GeV} \leq m^{\ell^+\ell^-} \leq 116 \text{ GeV}$
Jet Cuts (anti- $k_T$ , 0.4)	$p_{Tj} > 30 \text{ GeV},  y_j  < 4.4$ $\Delta R^{j\ell} > 0.5$

Table 4.2: Cuts applied to theory simulations in the ATLAS  $Z$ -plus-jets analysis results shown in Figs. (4.8)–(4.11).

Any jet which failed the final isolation cut was removed from the event, but the event itself is kept provided there are a sufficient number of other jets present. Throughout the central value of the HEJ predictions has been calculated with factorisation and

---

<sup>1</sup>At this point I feel it is necessary to apologise to those undergraduate physics students whose local computing use was disrupted by my scripts accidentally converting their computing labs into a server farm.

renormalisation scales set to  $\mu_F = \mu_R = H_T/2$ , and the theoretical uncertainty band has been determined by varying these independently by up to a factor of 2 in each direction (removing the corners where the relative ratio is greater than two). Also shown in the plots taken from the ATLAS paper are theory predictions from Alpgen [56], Sherpa [45, 48], MC@NLO [42] and BlackHat+Sherpa [22, 50]. We will also comment on the recent theory description of Ref. [39].

In Fig. (4.8), we begin this set of comparisons with predictions and measurements of the inclusive jet rates. HEJ and most of the other theory descriptions give a reasonable description of these rates. The MC@NLO prediction drops below the data because it only contains the hard-scattering matrix element for  $Z/\gamma^*$  production and relies on a parton shower for additional emissions. The HEJ predictions have a larger uncertainty band which largely arises from the use of leading-order results in the matching procedures.

The first differential distribution we consider here is the distribution of the invariant mass between the two hardest jets, Fig. (4.9). The region of large invariant mass is particularly important because this is a critical region for studies of vector boson fusion (VBF) processes in Higgs-plus-dijets. Radiation patterns are largely universal between these processes, so one can test the quality of theoretical descriptions in  $Z/\gamma^*$ -plus-dijets and use these to inform the VBF analyses. It is also a distribution which will be studied to try to detect subtle signs of new physics. In this study, HEJ and the other theory descriptions all give a good description of this variable out to 1 TeV, with HEJ being closest throughout the range. The merged sample of Ref. [39] (Fig. 9 in that paper) combined with the Pythia8 parton shower performs reasonably well throughout the range with a few deviations of more than 20%, while that combined with Herwig++ deviates badly. In a recent ATLAS analysis of  $W$ -plus-dijet events [3], the equivalent distribution was extended out to 2 TeV and almost all of the theoretical predictions deviated significantly while the HEJ prediction remained flat. This is one region where the high-energy logarithms which are only included in HEJ are expected to become large.

In Fig. (4.10), we show the comparison of various theoretical predictions to the distribution of the absolute rapidity difference between the two leading jets. It is clear in the left plot that HEJ gives an excellent description of this distribution. This is to some extent expected as high-energy logarithms are associated with rapidity separations. However, this variable is only the rapidity separation between the two hardest jets which is often not representative of the event as harder jets tend to be more central. Nonetheless, the HEJ description performs well in this restricted scenario.

The next-to-leading order (NLO) calculation of Blackhat+Sherpa also describes the distribution quite well while the other merged, fixed-order samples deviate from the data at larger values. The merged samples of Ref. [39] (Fig. 8 in that paper) describe this distribution well for small values of this variable up to about 3 units when combined with Herwig++ and for most of the range when combined with the Pythia8 parton shower, only deviating above 5 units.

The final distribution in this section is that of the ratio of the transverse momentum of the second hardest jet to the hardest jet. The perturbative description of HEJ does not contain any systematic evolution of transverse momentum and this can be seen where its prediction undershoots the data at low values of  $p_{T2}/p_{T1}$ . However, for values of  $p_{T2} \gtrsim 0.5p_{T1}$ , the ratio of the HEJ prediction to data is extremely close to 1. The fixed-order based predictions shown in Fig. (4.8) are all fairly flat above about 0.2, but the ratio of the data differs by about 10%.

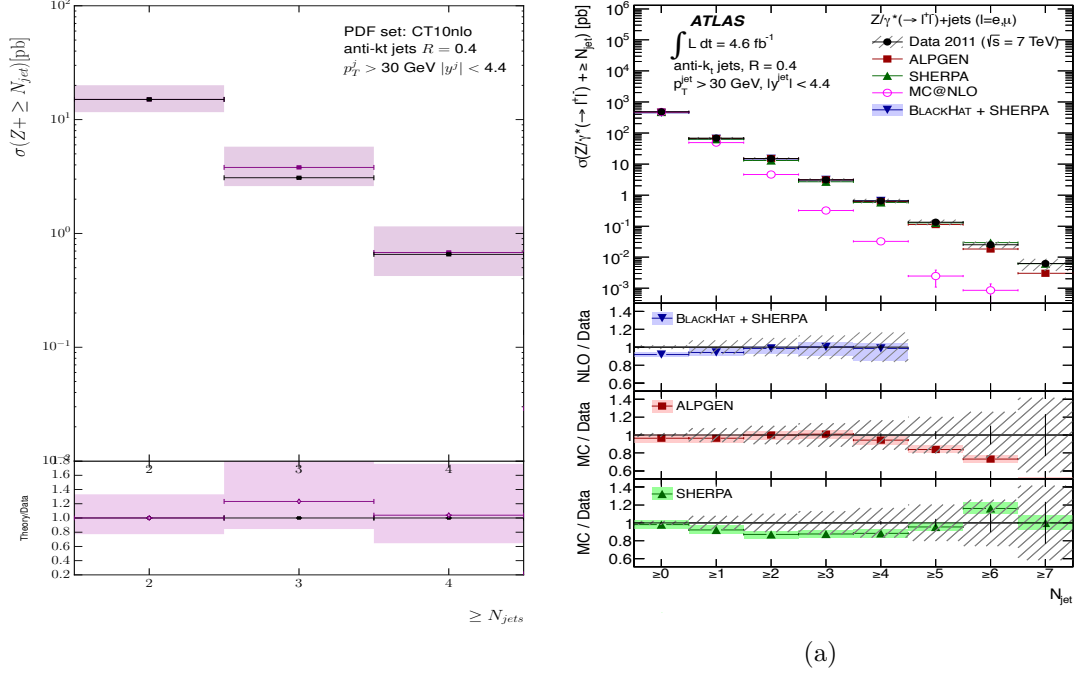


Figure 4.8: These plots show the inclusive jet rates from (a) HEJ and (b) other theory descriptions and data [1]. HEJ events all contain at least two jets and do not contain matching for 5 jets and above, so these bins are not shown.

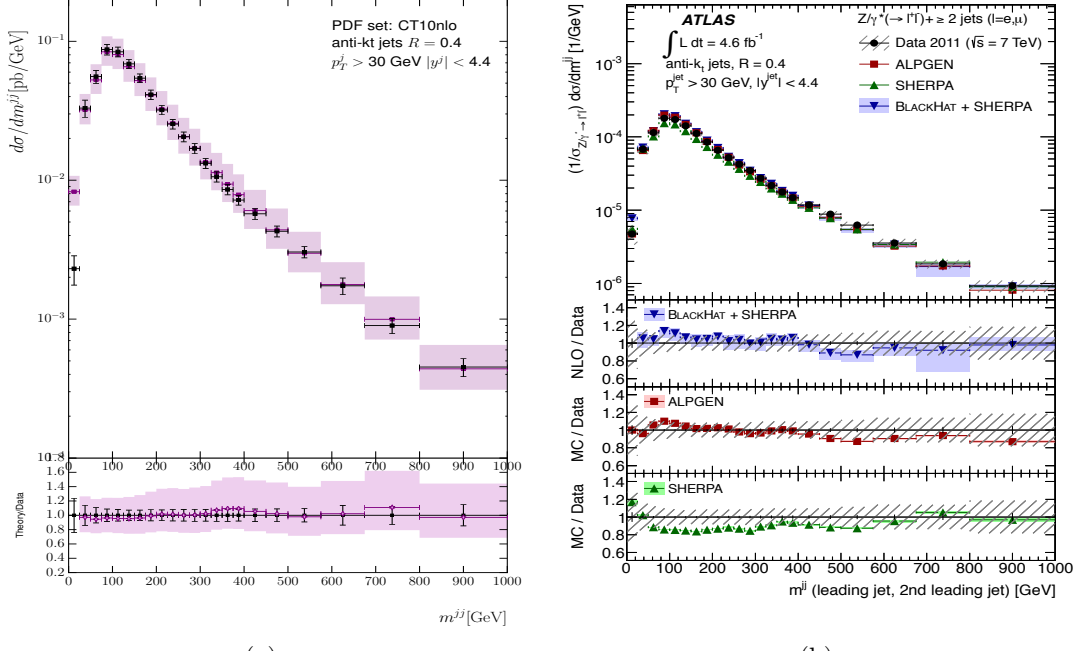


Figure 4.9: These plots show the invariant mass between the leading and second-leading jet in  $p_T$ . As in Fig. (4.8), predictions are shown from (a) HEJ and (b) other theory descriptions and data [1]. These studies will inform Higgs plus dijets analyses, where cuts are usually applied to select events with large  $m_{12}$ .

### 4.7.2 $Z/\gamma^* + \text{Jets}$ at the CMS Experiment

We now compare to data from a CMS analysis of events with a  $Z/\gamma^*$  boson produced in association with jets [52]. We show, for comparison, the plots from that analysis which contain theoretical predictions from Sherpa [45, 48], Powheg [7] and MadGraph [9]. The cuts used for this analysis are summarised in tab. (4.3).

Lepton Cuts	$p_{T\ell} > 20 \text{ GeV},  \eta_\ell  < 2.4$ $71 \text{ GeV} \leq m^{\ell^+\ell^-} \leq 111 \text{ GeV}$
Jet Cuts (anti- $k_T$ , 0.5)	$p_{Tj} > 30 \text{ GeV},  \eta_j  < 2.4$ $\Delta R^{j\ell} > 0.5$

Table 4.3: Cuts applied to theory simulations in the CMS  $Z$ -plus-jets analysis results shown in Figs. (4.12)–(4.14)

As in the previous section, any jet which failed the final isolation cut was removed from the event, but the event itself is kept provided there are a sufficient number of other jets present. The main difference to these cuts and those of ATLAS in the previous section is that the jets are required to be more central;  $|\eta| < 2.4$  as opposed to  $|y| < 4.4$ . This allows less room for evolution in rapidity; however, HEJ predictions are still relevant in this scenario. Once again, the central values are given by  $\mu_F = \mu_R = H_T/2$  with theoretical uncertainty bands determined by varying these independently by factors of two around this value. HEJ events always contain a minimum of two jets and therefore here we only compare to the distributions for an event sample with at least two jets or above.

We begin in Fig. (4.12) by showing the inclusive jet rates for these cuts. The HEJ predictions give a good description, especially for the 2- and 3-jet inclusive rates in this narrower phase space. The uncertainty bands are larger for HEJ than for the Sherpa and Powheg predictions due to our LO matching prescription (those for Madgraph are not shown).

In Figs. (4.13)–(4.14), we show the transverse momentum distributions for the second and third jet respectively (the leading jet distribution was not given for inclusive dijet events). Beginning with the second jet in Fig. (4.13), we see that the HEJ predictions overshoot the data at large transverse momentum. In this region, the non-FKL matched components of the HEJ description become more important and these are not controlled by the high-energy resummation. The HEJ predictions are broadly similar to Powheg's  $Z$ -plus-one-jet NLO calculation matched with the Pythia parton shower. In contrast, Sherpa's prediction significantly undershoots the data at large transverse momentum. Here the Madgraph prediction gives the best description of the data.

Fig. (4.14) shows the transverse momentum distribution of the third jet in this data sample. Here, the ratio of the HEJ prediction to data shows a linear increase with transverse momentum (until the last bin where all the theory predictions show the same dip). Both the Sherpa and Powheg predictions show similar deviations for this variable while the Madgraph prediction again performs very well.

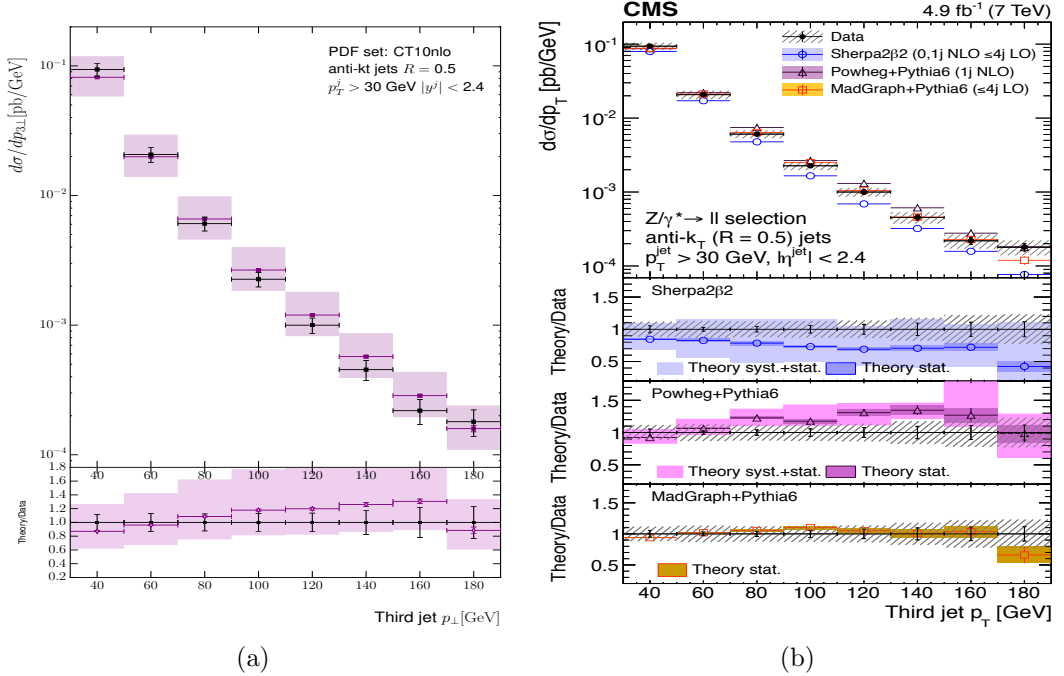


Figure 4.14: The transverse momentum distribution of the third hardest jet in inclusive dijet events in [52], compared to (a) the predictions from HEJ and (b) the predictions from other theory descriptions.

## 4.8 Conclusions

Conclusions of  $Z/\gamma^* + \text{jets}$ .

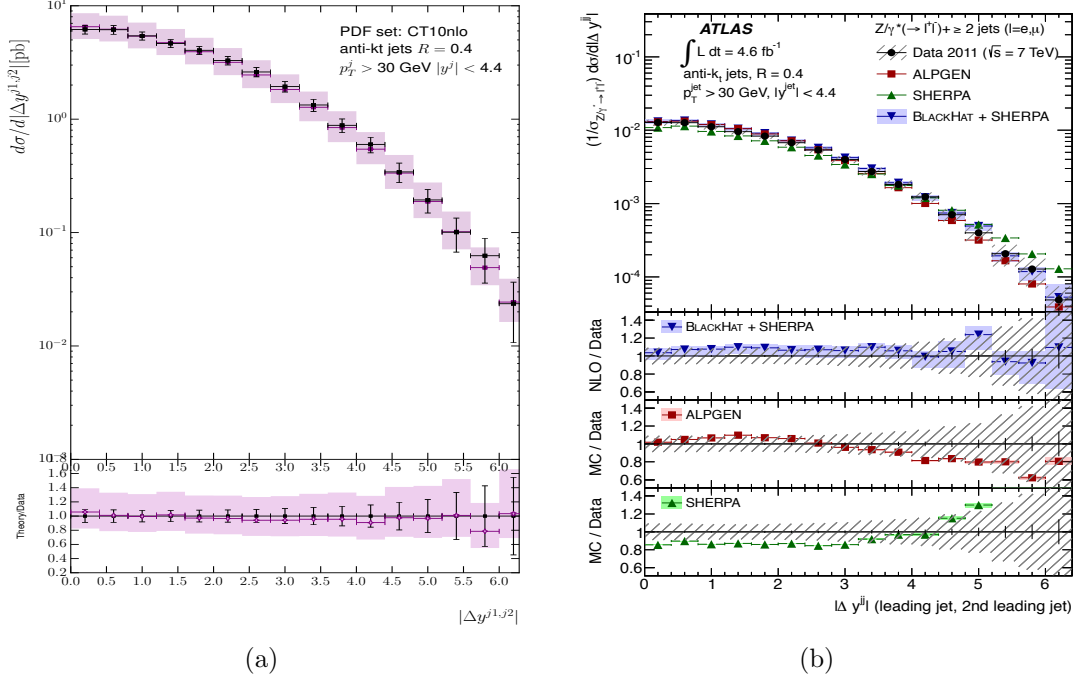


Figure 4.10: The comparison of (a) HEJ and (b) other theoretical descriptions and data [1] to the distribution of the absolute rapidity different between the two leading jets. HEJ and Blackhat+Sherpa give the best description.

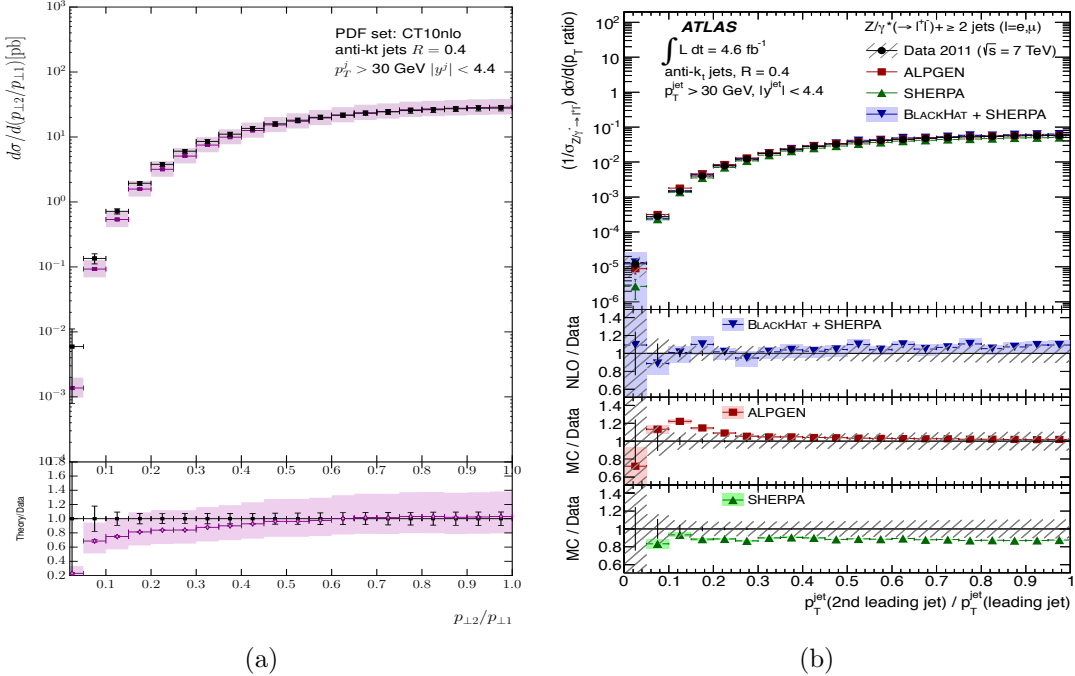


Figure 4.11: These plots show the differential cross section in the ratio of the leading and second leading jet in  $p_T$  from (a) HEJ and (b) other theory descriptions and data [1].

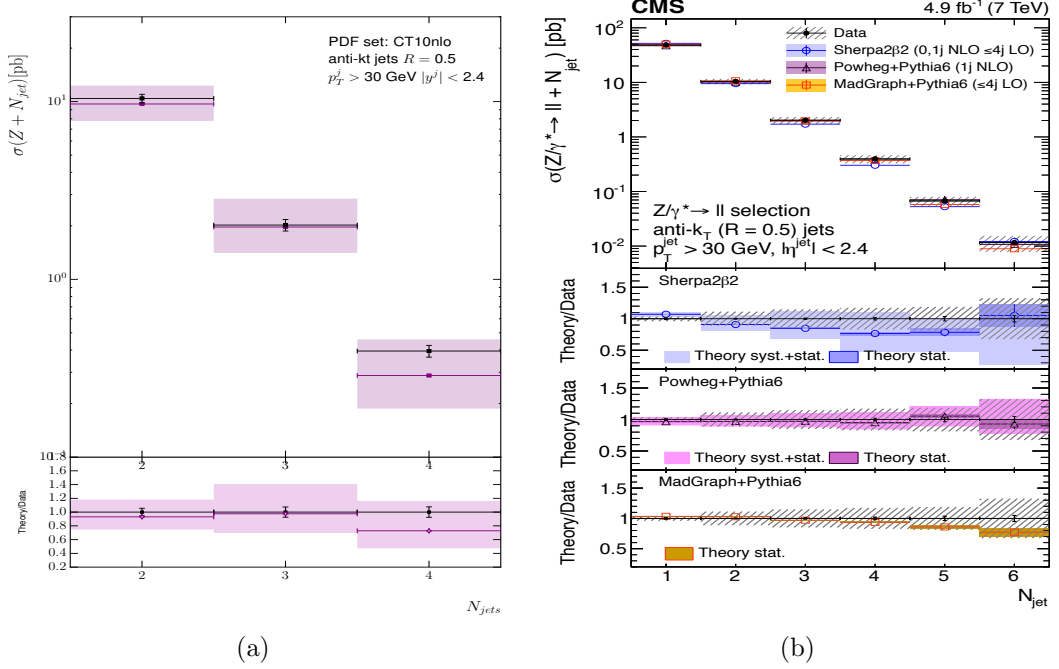


Figure 4.12: The inclusive jet rates as given by (a) the HEJ description and (b) by other theoretical descriptions, both plots compared to the CMS data in [52].

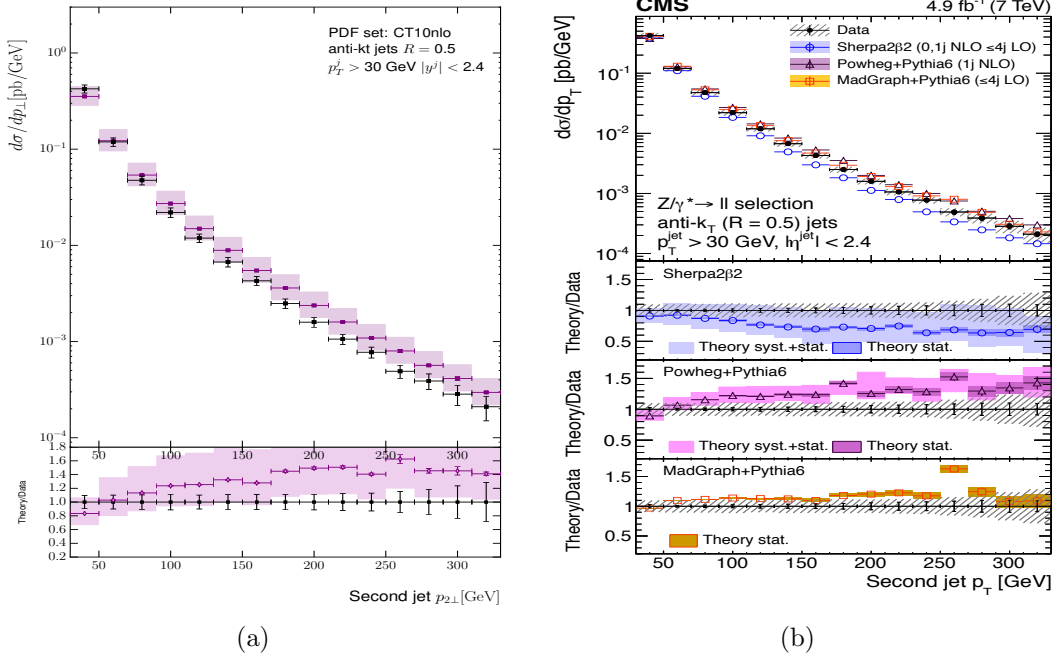


Figure 4.13: The transverse momentum distribution of the second hardest jet in inclusive dijet events in [52], compared to (a) the predictions from HEJ and (b) the predictions from other theory descriptions.



## Chapter 5

# Dijets and Gap Jets at ATLAS

Here we present the results of a complex experimental study of the effects of jet vetoes and azimuthal decorrelations in dijet events [2]. High Energy Jets is compared to both data and state-of-the-art fixed-order perturbative QCD predictions (supplemented with radiation by merging with a parton shower) from **POWHEG+** PYTHIA8 and **POWHEG+HERWIG** (both implemented through the **POWHEG BOX** package [58]).

The data compared to are 7 TeV proton-proton collisions as observed by the ATLAS experiment in two distinct data sets referred to as 2010 data and 2011 data. The experimental cuts applied to these data sets differs and both are outlined in table (5.1).

2010 Jets (anti- $k_T$ , 0.6)	$p_{Tj} > 20 \text{ GeV},  y_j  < 4.4$ $p_{T1} > 60.0 \text{ GeV}, p_{T2} > 50.0 \text{ GeV},$ $Q_0 = 20 \text{ GeV}$
2011 Jets (anti- $k_T$ , 0.6)	$p_{Tj} > 30 \text{ GeV},  y_j  < 2.4$ $p_{T1} > 60.0 \text{ GeV}, p_{T2} > 50.0 \text{ GeV}$ $Q_0 = 30 \text{ GeV}, \Delta y_{jj} > 1.0$

Table 5.1: Cuts applied to theory simulations in the ATLAS dijets analyses.  $Q_0$  is the gap jet veto scale. The results are shown in figs. (5.1)–(5.6).

This study focused on additional jet activity in dijet where the dijet system is constructed using the two leading jets in  $p_T$ . These two jets are required to be significantly harder than any additional jets with extra cuts on the leading and sub-leading jets of 50 GeV and 60 GeV respectively. After tagging the two leading jets in the event and considering all other jet radiation in the rapidity interval bounded by the dijets as a QCD correction. Within in the two data sets defined in table (5.1) a further subdivision was made. For both the 2010 and 2011 data a subset of events was defined by vetoing events with extra QCD radiation in the rapidity interval bounded by the

dijet system above some veto scale  $Q_0$ . It should also be noted that the 2011 data set required a minimum rapidity gap of 1.0 between all jets (for both cases with and without the gap jet veto) in order to encourage a rapidity span into which extra radiation may arise. The full breakdown of this analysis then is into four event categories; 2010 data with and without a veto applied to gap jets and the 2011 data with and without a veto applied to gap jets.

The predictions for these analyses generated by the High Energy Jets collaboration are given for both the partonic HEJ calculation (shown in green in this chapter) and the HEJ+ARIADNE calculation (shown in orange). HEJ+ARIADNE is a parton shower package based on the Lund colour cascade dipole model. Due to the steps in this interfaced package necessary to remove the double counting (which arises from HEJ and HEJ+ARIADNE both generating soft radiation) generating large data samples which can be used to give statistically significant predictions is *extremely* computationally demanding. In a standard partonic HEJ run we evaluate the matrix element for each event at 76 different scale choices (since we allow for four choices of ‘central’ scale and 19 combinations of the renormalisation scale,  $\mu_r$ , and factorisation scale,  $\mu_f$  based on each central choice). After we chose a central scale (this choice is done while blind to the data for fairness) one set of these 19 scales combinations form an ‘envelope’ of predictions for each bin in each plot - this spread is then represented by the green bands shown in the figs. (5.1)–(5.6). However, because of the structure of the matrix element evaluations within HEJ+ARIADNE we can only afford one scale choice per event and, as such, we cannot provide scale variation uncertainty bands with our showered numbers. To be clear this is not a limitation of the physics since it is entirely possible to evaluate each matrix element multiple times - it is a computational consideration.

<sup>1</sup> The orange bands shown with the HEJ+ARIADNE predictions throughout this chapter are the statistical bands (shown, as usual, at the 68% confidence level).

Observables were studied as a function of two properties of the dijets. The rapidity gap between the dijets,  $\Delta y$ , and the mean traverse momenta of the dijet system,  $\overline{p_T}$ . Naïvely for small  $\Delta y$  we expect to see very little gap jets since there is a limited region in which extra jets may be clustered before they are clustered in to the dijet system itself. Conversely, as we pull the dijets apart in rapidity we expect to see an increase in additional QCD radiation (since there is a larger phase space in which to radiate). Similarly for  $\overline{p_T}$ , we expect that events with harder dijet systems will have higher gap

---

<sup>1</sup> As seen in chapter (4), the renormalisation scale appears in a non-trivial way in the High Energy Jets matrix element. It is contained implicitly in the strong coupling constant which is contained within the virtual corrections exponential. As such we cannot simply generate predictions at a single scale and then reweight events at the post-analysis level. In principle, we *could* do this for our PDF evaluations though in practice this is very computationally cheap and therefore we chose not to.

---

activity simply because they have more energy available to radiate away into additional jets.

Throughout the remainder of this chapter the (a) sub-figures show data and predictions for the 2010 data set with respect to the rapidity span of the dijet system,  $\Delta y$ , while the (b) sub-figures show data and predictions from the 2011 data set with respect to the mean transverse momenta of the dijet system,  $\overline{p_T}$ .

We begin by discussing the gap fraction,  $f(Q_0)$ , defined as:

$$f(Q_0) = \frac{\sigma_{jj}(Q_0)}{\sigma_{jj}}, \quad (5.1)$$

where  $\sigma_{jj}(Q)$  is the total dijet cross section and  $\sigma_{jj}(Q_0)$  is the dijet cross section passing the veto on additional gap scales for a scale choice  $Q_0$ . Fig. (5.1) shows the gap fraction with a veto scale of 20 GeV in fig. (5.1a) and a veto scale of 30 GeV in fig. (5.1b). The behaviour observed is in line with our naïve guess discussed previously since the gap fraction decreases at both large  $\Delta y$  and large  $\overline{p_T}$ . We can see the best description of both data sets is given by **HEJ+ARIADNE** (excluding two very high  $\overline{p_T}$  bins where the predictions from **HEJ+ARIADNE** are visibly statistically limited). The partonic **HEJ** prediction overshoots both data sets meaning that we underestimate the jet activity in the gap region while the predictions from **POWHEG** plus parton showers overestimate the QCD radiation here. From fig. (5.1) it is clear that in this situation it is not sufficient to only describe the wide-angle logarithmically enhanced terms resummed within the High Energy Jets framework and that the soft and collinear logarithms added by interfacing to **HEJ+ARIADNE** play a very important rôle. It is visible from fig. (5.1) that the scale variations shown in *partonic HEJ* (since the **HEJ+ARIADNE** bands are statistical only) are quite significantly bigger than that shown by the other predictions. This is expected since we only include matching up to leading-order whereas **POWHEG** is formally NLO accurate; it is well observed that as we include higher order terms (in the fixed order sense) we gain a better control of the scale uncertainties.

Similarly, when we study the mean number of jets in the rapidity interval shown for in fig. (5.2) we see that **HEJ+ARIADNE** and **POWHEG+PYTHIA8** give the best description of the data. Once again the partonic **HEJ** prediction undershoots the data significantly when describing both of the dijet characteristics while **POWHEG+HERWIG** overestimates the jet activity.

We now turn to look at the azimuthal decorrelations of dijet systems. These are defined as  $\langle \cos(n(\pi - \Delta\phi)) \rangle$  with  $n = 1, 2, \dots$ . Here we only consider the first and

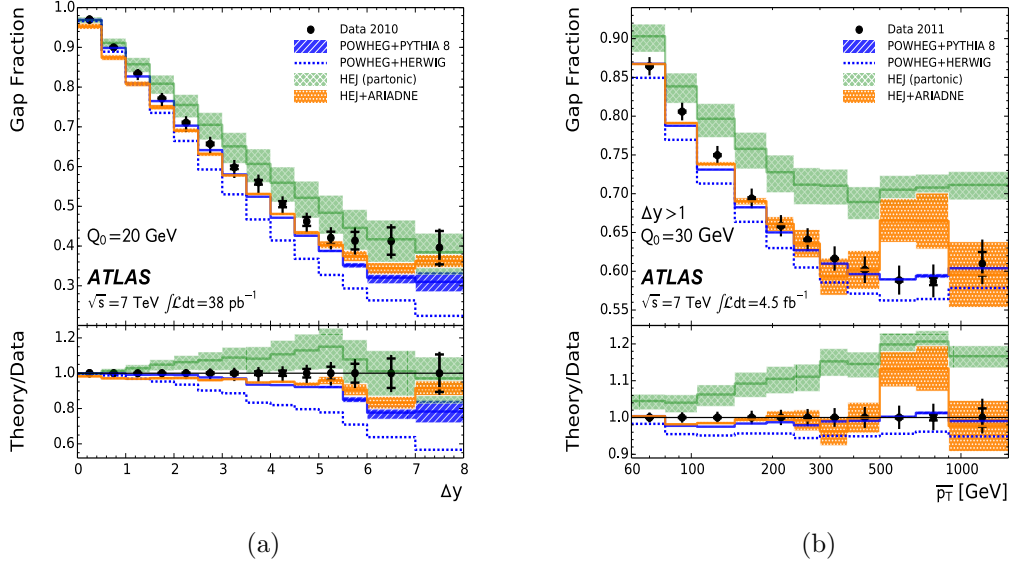


Figure 5.1: The gap fraction,  $f(Q_0)$ , as a function of (a) the rapidity gap,  $\Delta y$ , and (b) the average  $p_T$ ,  $\overline{p}_T$ , of the dijet system.

second ‘moments’; that is,  $n = 1, 2$ . We follow the notation of [2] and rewrite the second moment as  $\langle \cos(2\Delta\phi) \rangle$ . Clearly for a final state with two partons momentum conservation will enforce that the jets be in a back-to-back configuration i.e. they will have  $\Delta\phi = 0$  and both  $\langle \cos(\pi - \Delta\phi) \rangle$  and  $\langle \cos(2\Delta\phi) \rangle$  will simply be a flat line 1.0. As we allow these hard dijets to radiate the moments will depart from the straight line as the constraint softens and the extra radiation allows for  $\Delta\phi < \pi$ . These moments have long been seen as an excellent test of the difference between DGLAP QCD parton showers and BFKL-like resummations [35]. Indeed it is in these figures where we see the biggest difference between HEJ and the POWHEG plus parton shower results.

Fig. (5.3) shows the first azimuthal moment for the inclusive selection. We see that in the 2010 study HEJ+ARIADNE and both POWHEG descriptions slightly underestimate  $\langle \cos(\pi - \Delta\phi) \rangle$  while the partonic HEJ result slightly overestimates. However, the evolution of the first azimuthal moment with respect to  $\overline{p}_T$  shows a clear difference between the two formalisms. HEJ does not radiate sufficiently to predict the correct decorrelation at low mean transverse momentum (which is understood since it does not include the parton shower effects) while both POWHEG descriptions cause too much decorrelation at low  $\overline{p}_T$ . The best description of the data is given by HEJ+ARIADNE since it adds extra emissions to High Energy Jets which improves our description of the decorrelation.

Another variable thought to be a good test of DGLAP vs. BFKL physics is the ratio of

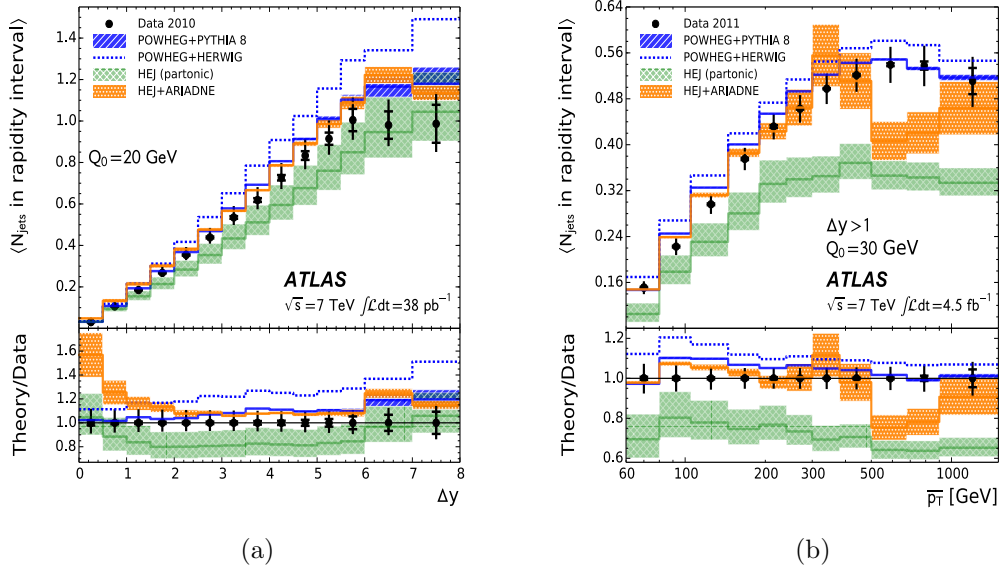


Figure 5.2: The average number of jets,  $\langle N_{\text{jets}} \text{ in the rapidity interval} \rangle$ , in the rapidity gap bounded by the dijet system, as a function of (a) the rapidity gap,  $\Delta y$ , and (b) the average  $p_T$ ,  $\bar{p}_T$ , of the dijet system.

the second moment to the first moment. This is shown in fig. (5.4). Once again we do see a sizeable difference in the predictions given by the two resummations. Similarly to fig. (5.3) we see that interfacing to the HEJ+ARIADNE package brings the partonic HEJ prediction in to a much better agreement of the data.

The two remaining figures are similar to figs. (5.3) and (5.4) but with the addition of the jet veto. Similarly to the inclusive case we see that the partonic HEJ predictions overestimates the correlation for the 2010 and the 2011 data sets while the NLO plus shower predictions, once again, understood the decorrelation. Given the statistical limited data available (especially for the 2010 gap jet vetoed data set) it is more difficult to draw clear conclusions here but certainly the inclusion of the HEJ+ARIADNE shower improves the High Energy Jets results.

Lastly we have the ratio of the second azimuthal moment to the first azimuthal moment for the events which pass the additional jet veto. HEJ+ARIADNE and POWHEG+PYTHIA8 come closest to describing the data however there is some disagreement; in particular no one gives a good description of the evolution of this ratio at low  $\bar{p}_T$ .

In summary, the best description of the data overall is given by HEJ+ARIADNE and POWHEG+PYTHIA8 while parton level HEJ overestimates (underestimate) the gap fraction (the mean number of jets in the rapidity gap bounded between the dijet system) and overshoots both the first azimuthal moment and the ratio of the second to the first

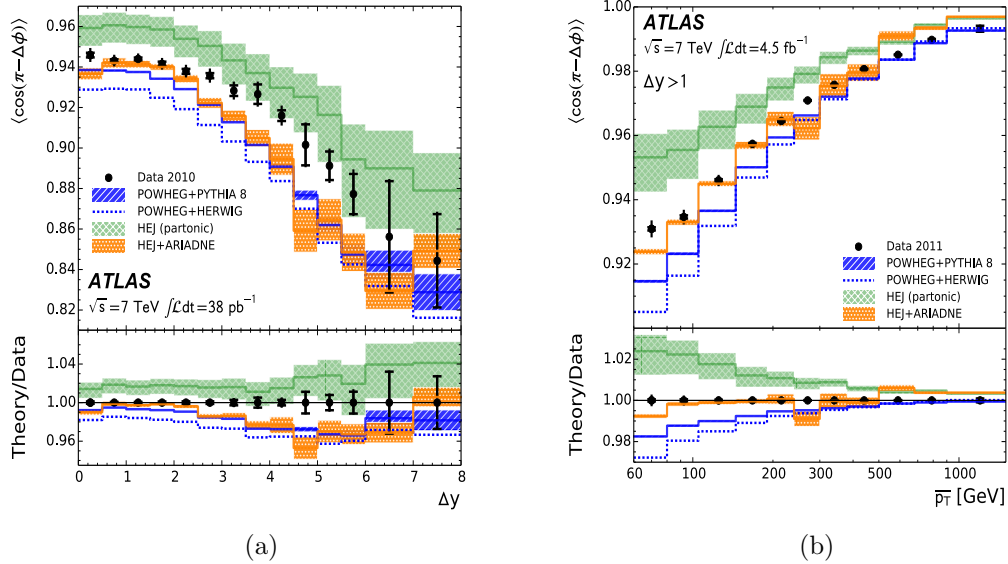


Figure 5.3: The first azimuthal angular moment,  $\langle \cos(\pi - \Delta\phi) \rangle$ , as a function of (a) the rapidity gap,  $\Delta y$  and (b) the average  $p_T$ ,  $\bar{p}_T$ , of the dijet system.

azimuthal moment. POWHEG+HERWIG describes the data poorly for the gap fraction, the mean number of gap jets and the azimuthal decorrelations. From this it is clear that while the logarithmically enhanced resummed in the High Energy Jets framework are important in regions of phase space where we have large rapidity gaps (such as the analyses described here) there are equally important contributions arising from the logarithms given to us by the interface with a parton shower.

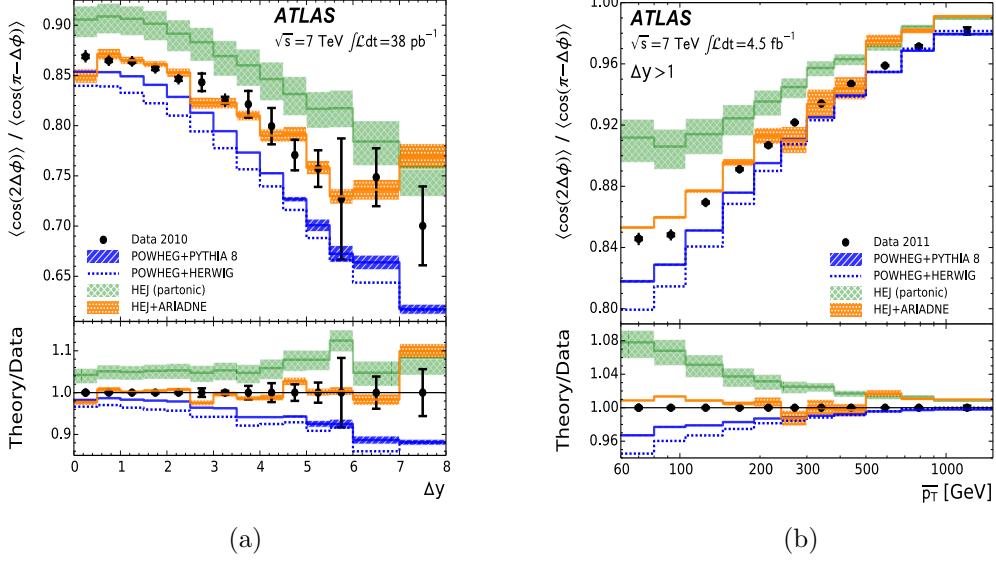


Figure 5.4: The ratio of the second azimuthal angular moment,  $\langle \cos(2\Delta\phi) \rangle$ , to the first azimuthal angular moment,  $\langle \cos(\pi - \Delta\phi) \rangle$ , as a function of (a) the rapidity gap,  $\Delta y$ , and (b) the average  $p_T$ ,  $\bar{p}_T$ , of the dijet system.

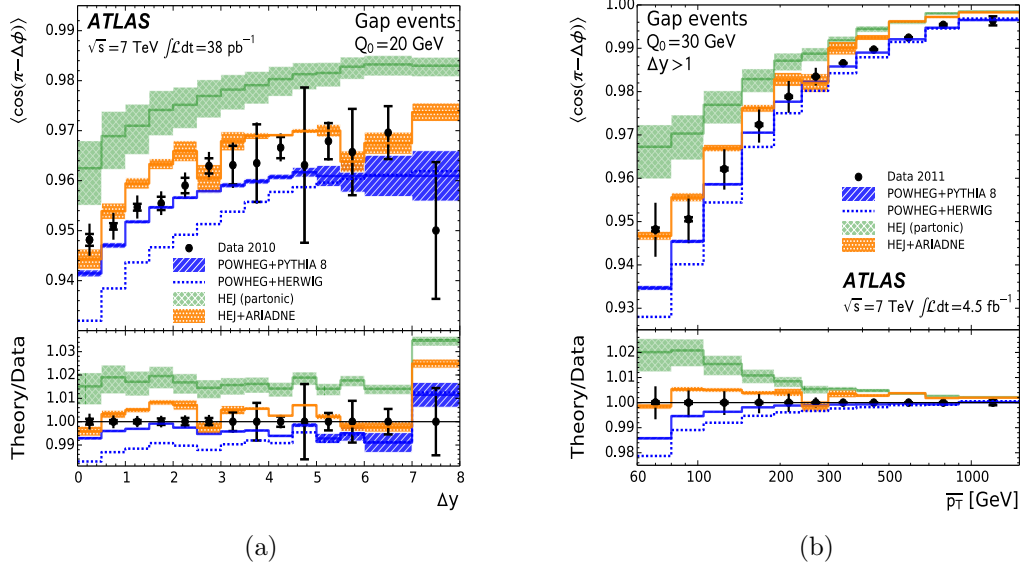


Figure 5.5: The first azimuthal angular moment,  $\langle \cos(\pi - \Delta\phi) \rangle$ , for events passing the veto on gap activity above  $Q_0 = 20$  GeV as a function of (a) the rapidity gap,  $\Delta y$ , and (b) the average  $p_T$ ,  $\bar{p}_T$ , of the dijet system.

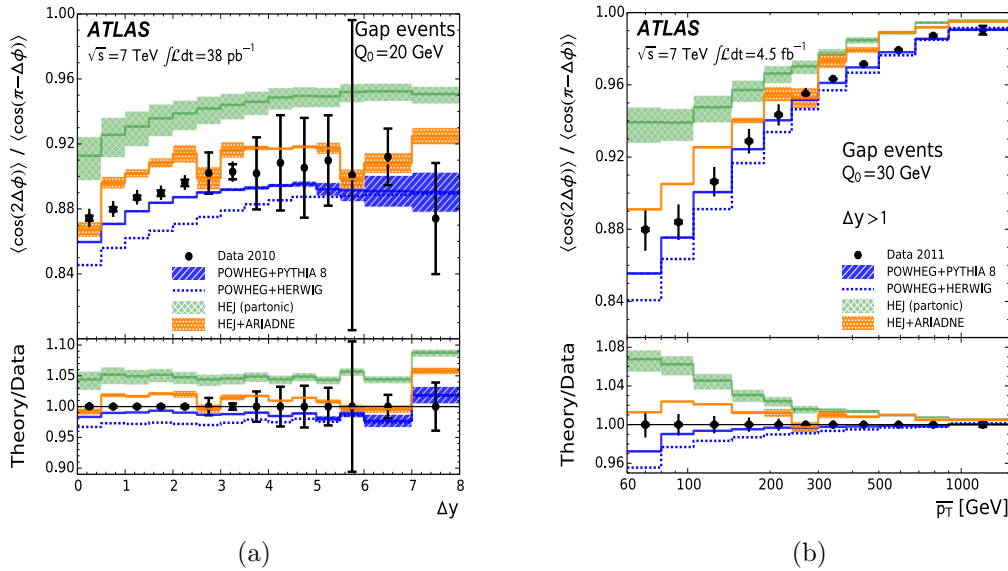


Figure 5.6: The ratio of the second azimuthal angular moment,  $\langle \cos(2\Delta\phi) \rangle$ , to the first azimuthal angular moment,  $\langle \cos(\pi - \Delta\phi) \rangle$ , as a function of (a) the rapidity gap,  $\Delta y$ , and (b) the average  $p_T$ ,  $\overline{p}_T$ , of the dijet system. A veto of  $Q_0 = 20\text{GeV}$ , for (a), and  $Q_0 = 30\text{GeV}$ , for (b), is applied on activity in the rapidity gap is applied.

# Chapter 6

## $Z/\gamma^*$ +Jets at 100TeV

Even though the Large Hadron Collider is still in its infancy there is an ever growing effort to discuss where we go next as a high energy collider physics community. A wide range of options have been put forward including the linear colliders Compact Linear Collider (CLIC) [6] and the International Linear Collider (ILC) [26]. While both of these machines are designed to be precision electron-positron linear colliders they have very different designs; CLIC would operate at around a centre-of-mass energy of 3 TeV and use cutting edge accelerating technology whereas the ILC would collide at 0.5 TeV (with a possible upgrade to 1 TeV).

However, there are other suggestions on the table. Of particular interest for this work is the prospect of a hadronic Future Circular Collider (FCC-hh). There are other possible initial states such as hadron-lepton or a lepton-lepton being discussed but for obvious reasons it is the FCC-hh which we will focus on here.

One particularly exciting scenario is that of a 100 TeV hadronic collider housed in an extended tunnel approximately 100 km in circumference at the CERN site in Geneva. Such a machine would make an excellent ‘discovery machine’ since it would cover a vast range in partonic centre-of-mass energies. The energies probed here would be orders of magnitude higher than ever seen at a hadronic collider and so this would be an invaluable test of high scale QCD. Similarly to physics at the current LHC the dominant background would be QCD in nature and so in order for us to be able to extract useful information about potential new physics we would need to be able to model this QCD background with incredible precision. Current state-of-the-art for many QCD is still limited to next-to-leading order in  $\alpha_s$  although progress is being made towards improving this to next-to-next-to-leading order in some key physics processes, for example Higgs production at NNLO is known [30]. However, as in the preceding

chapters we will instead investigate the effects of the higher-order logarithmically enhanced contributions to the perturbative series. As discussed in chapter 2 these terms are not all captured by NNLO (or any fixed-order scheme  $N^m\text{LO}$  for that matter).

The results of chapters 4 and 5 clearly show that these effects are important at a the 7 TeV for both dijets and  $Z/\gamma^* + \text{dijets}$  respectively. We therefore expect that a fixed-order *only* perturbative description of QCD at a 100 TeV FCC-hh would not be give a reasonable description of data since the phase space available to final state QCD radiation at such a collider we would expect to see a greater effect from the terms enhanced in the High Energy limit.

Here we present a study of  $Z/\gamma^* + \text{dijets}$  at a centre-of-mass energy of 100 TeV. The final state cuts are outlined in table (6.1). For each figure we show the equivalent result calculated at 7 TeV with a jet  $p_T$  cut of 30 GeV (which was found to be in excellent agreement with data) as well as the 100 TeV predictions for jet cuts of 30 GeV, 60 GeV and 100 GeV. The jet cut choice is an interesting problem since it the best variable for weeding out physics other than the hard perturbative scatter. For example, even at the 7 TeV LHC a QCD study with a jet cut of, say, 10 GeV would be as much a test of our theoretical understanding of perturbative physics as it would a test of our descriptions for parton showers, multiple parton interactions and underlying event. While this is a perfectly valid analysis to do it is *not* the best choice if our aim is to improve our understanding of perturbative QCD. The same argument applies for a 100 TeV collider only more so! As we go to increasingly higher centre-of-mass energies we may need to raise our jet cuts so as to ensure the data we hope to describe is as unpolluted as possible. Each figure also shows the ratio of the 100 TeV prediction to the 7 TeV prediction to emphasise any features which may otherwise be hard to see.

Lepton Cuts	$p_{T\ell} > 20 \text{ GeV},  \eta_\ell  < 2.5$ $\Delta R^{\ell^+\ell^-} > 0.2, 66 \text{ GeV} \leq m^{\ell^+\ell^-} \leq 116 \text{ GeV}$
Jet Cuts (anti- $k_T$ , 0.4)	$p_{Tj} > 30 \text{ GeV}, 60 \text{ GeV}, 100 \text{ GeV}$ $ y_j  < 4.4, \Delta R^{j\ell} > 0.5,$

Table 6.1: Cuts applied to theory simulations for the 100 TeV  $Z$ -plus-jets analysis results shown in Figs. (6.1)–(6.6c).

We begin by discussing what is by far the most uninteresting figure in this thesis. Fig. 6.1 shows the differential distribution with respect to the azimuthal separation of the two leading jets in  $p_T$ ,  $\Delta\phi_{j1,j2}$ . It is clear that although the cross-section of the 100 TeV result is significantly greater than that of the 7 TeV result the increase in cross-section is uniformly throughout the range of  $\Delta\phi_{j1,j2}$  - this is clear from the ratio. What makes the uninteresting fig. 6.1 interesting is that if QCD behaved exactly the

---

same at 100 TeV as it did at 7 TeV we would expect all of the plots in this chapter to have a ratio line which was a perfectly straight line which merely reflected the increase in cross-section. However, this turns out not to be the case.

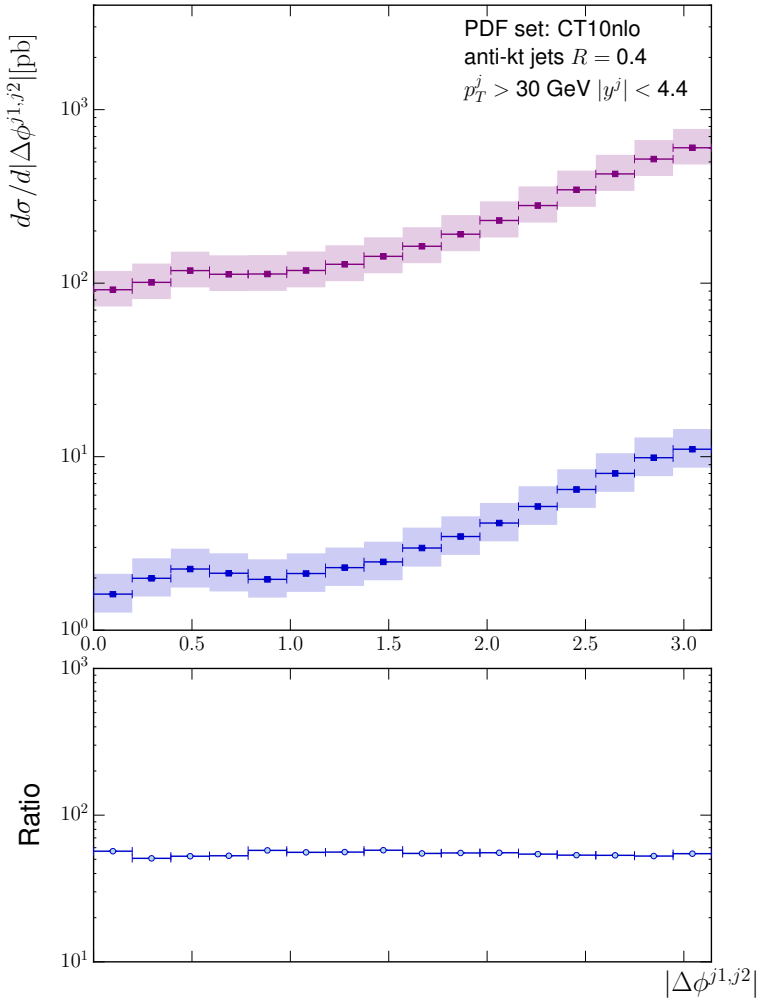


Figure 6.1: The differential cross-section for  $Z/\gamma^*$  plus inclusive dijets as a function of the azimuthal separation of the dijet system shown for centre-of-mass energies of 7TeV (blue) and 100TeV (pink).

Fig 6.2 shows the inclusive  $Z/\gamma^* + \text{dijets}$  cross-section as a function of the number of jets,  $N_{\text{jet}}$ . Once again we see that the total integrated cross-section grows as we go to higher energy but we also see that the relative contribution to the cross-section increases as we go to higher jet multiplicity. This is direct evidence that the convergence of the QCD perturbative expansion worsens as we go to higher energy. Clearly then resummation effects such as those described by High Energy Jets become more important at a prospective FCC-hh machine and will need to be included not only so that we have

understand the QCD background well enough to extract and study new physics but also in order for precision tests of QCD.

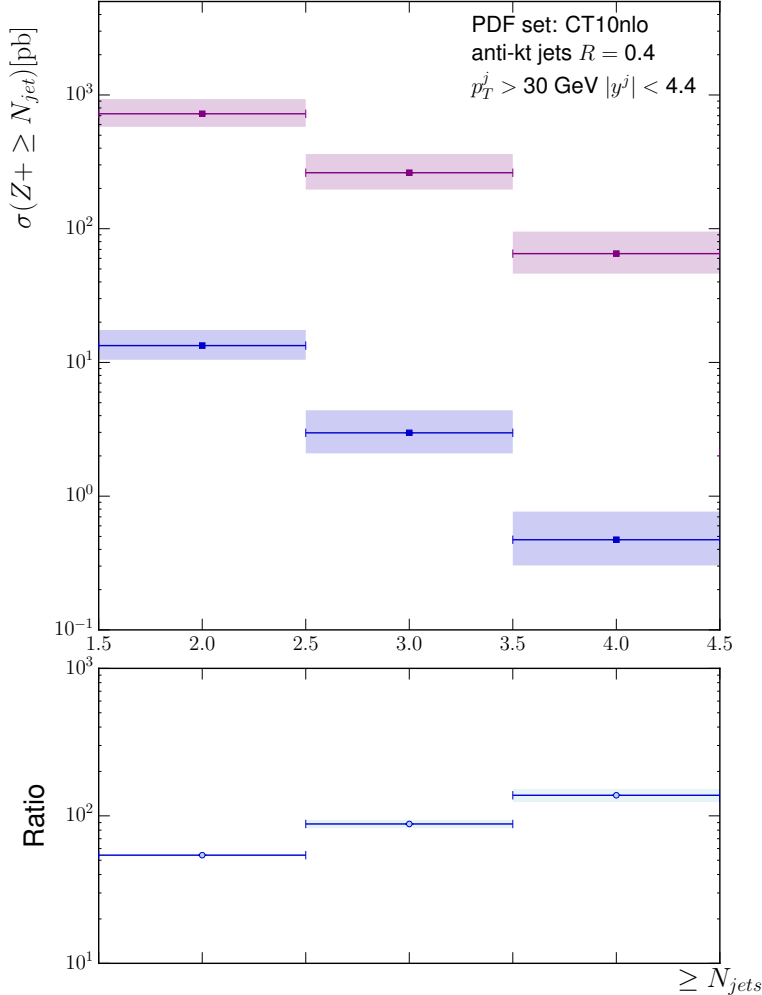


Figure 6.2: The cross-section for  $Z/\gamma^*$  plus inclusive dijets as a function of the number of jets,  $N_{\text{jet}}$ , shown for centre-of-mass energies of 7TeV (blue) and 100TeV (pink).

Fig 6.3 shows the differential distribution with respect to the absolute value of the rapidity span between the two leading jets in  $p_T$ ,  $\Delta y^{j1,j2}$ . We see that as we go to large rapidity gaps between the dijets the relative increase in the cross-section grows by almost a factor or 10. This is precisely

Fig. ((6.3)) notes:

- dy plot,
- O(10) increase in cross-section as we go to large rapidities,

- 
- More energy in initial state means we can get more jets further in to the outer regions of  $y$ -space,
  - The increase seen is *exactly* the large logs we capture at play

Fig. ((6.4)) notes:

- $dm_j j$  plot,
- $O(10)$  increase in cross-section as we go to large invariant masses,
- Invariant masses again correlate with the logs we resum (show this explicitly if you havent already),
- Similar to fig. ((6.3))

Fig. ((6.5a)-(6.5c)) notes:

- $pT$  distributions,
- Heavy tails...soooo?
- More energy in initial state means we can get more jets further in to the outer regions of  $y$ -space,
- What effect would a shower have on these distributions? Plenty of spare  $pT$  to radiate.

Fig. ((6.6a)-(6.6c)) notes:

- Not much more to say about these - mostly covered in  $dy$  plots,

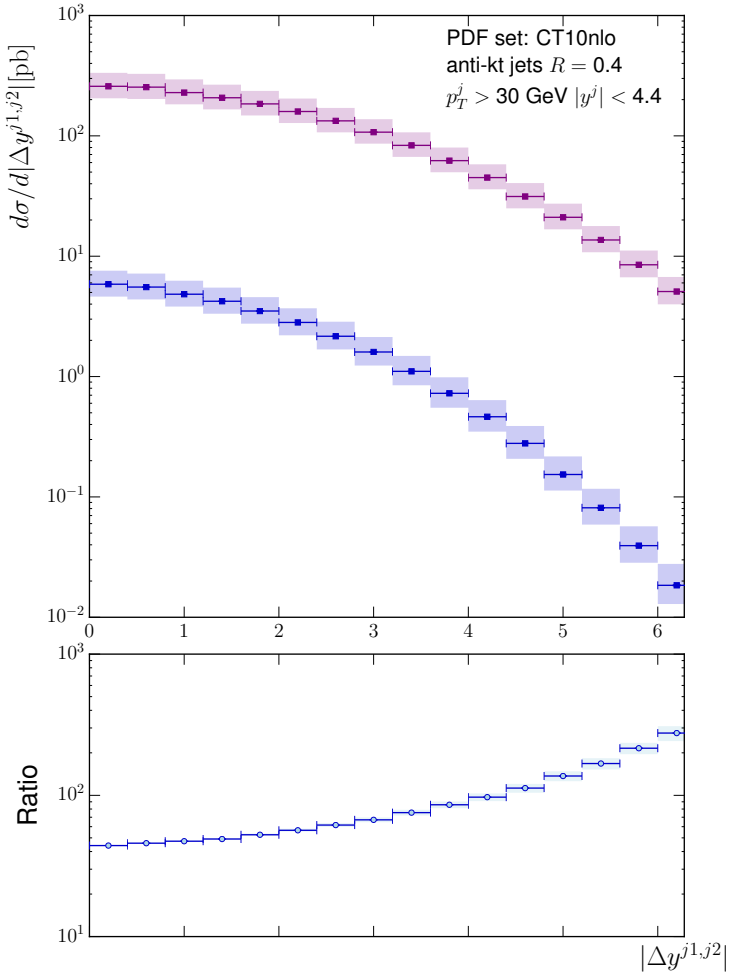


Figure 6.3: The differential cross-section for  $Z/\gamma^*$  plus inclusive dijets as a function of the absolute value of the rapidity gap between the dijets,  $\Delta y^{j1,j2}$  shown for centre-of-mass energies of 7TeV (blue) and 100TeV (pink).

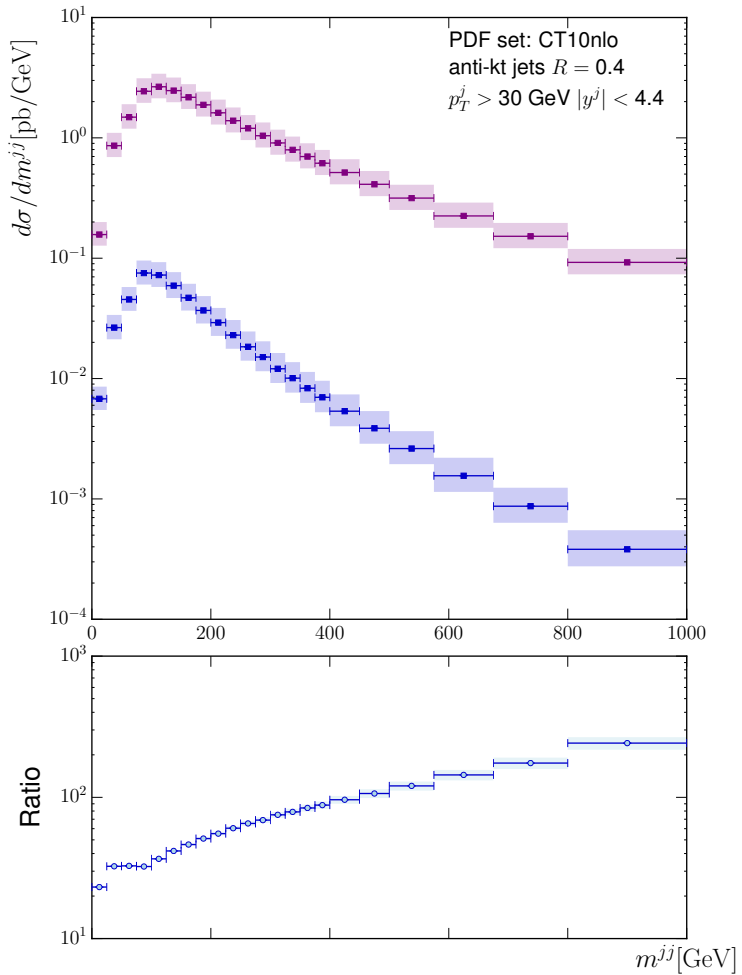


Figure 6.4: The differential cross-section for  $Z/\gamma^*$  plus inclusive dijets as a function of the invariant mass of the dijets,  $m^{jj}$ , shown for centre-of-mass energies of 7TeV (blue) and 100TeV (pink).

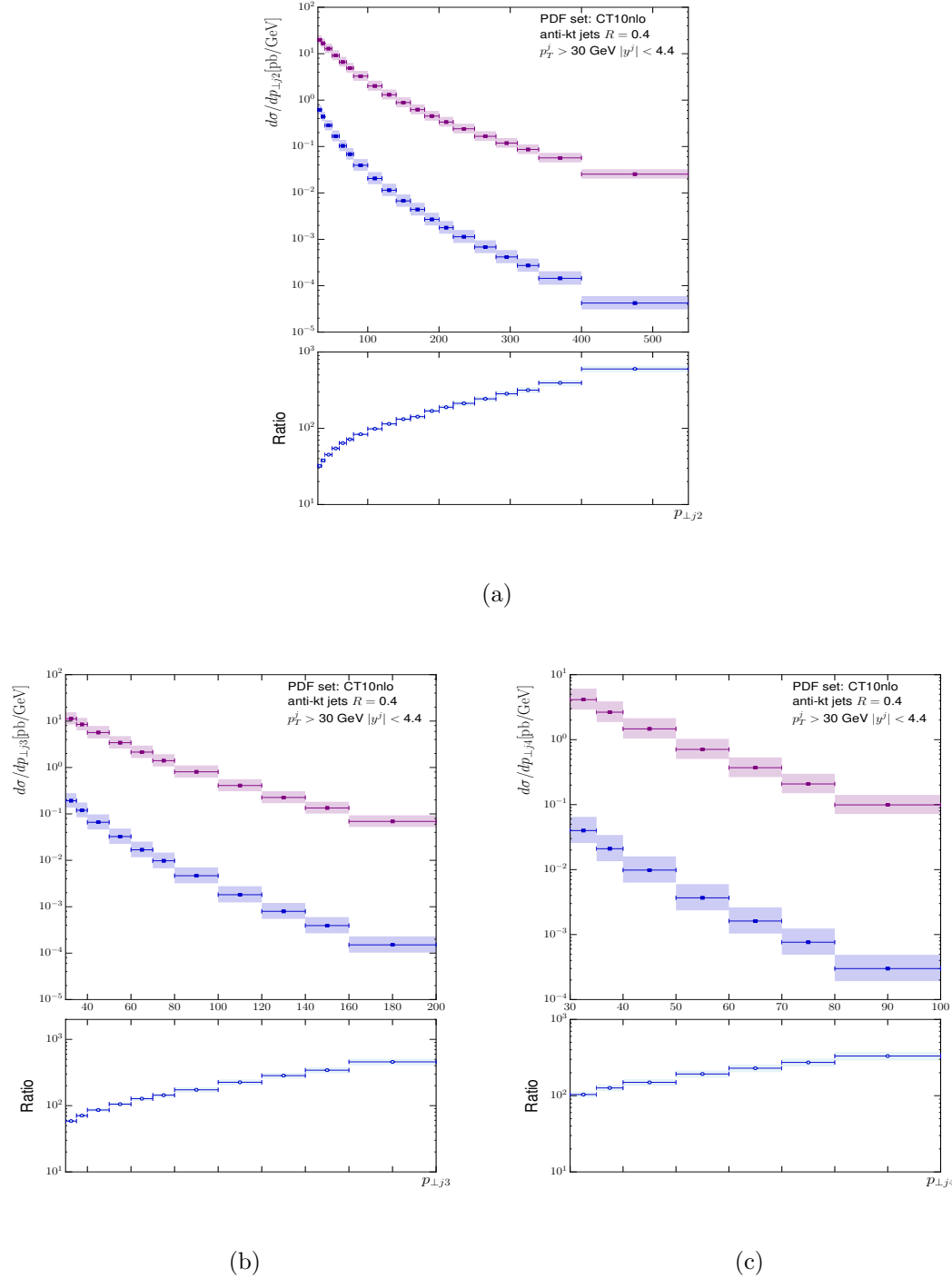
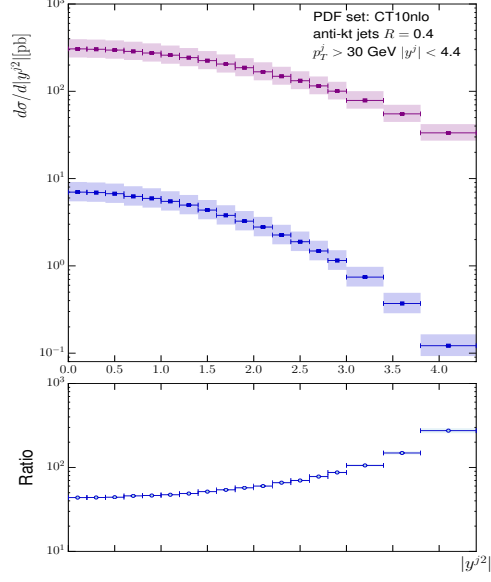
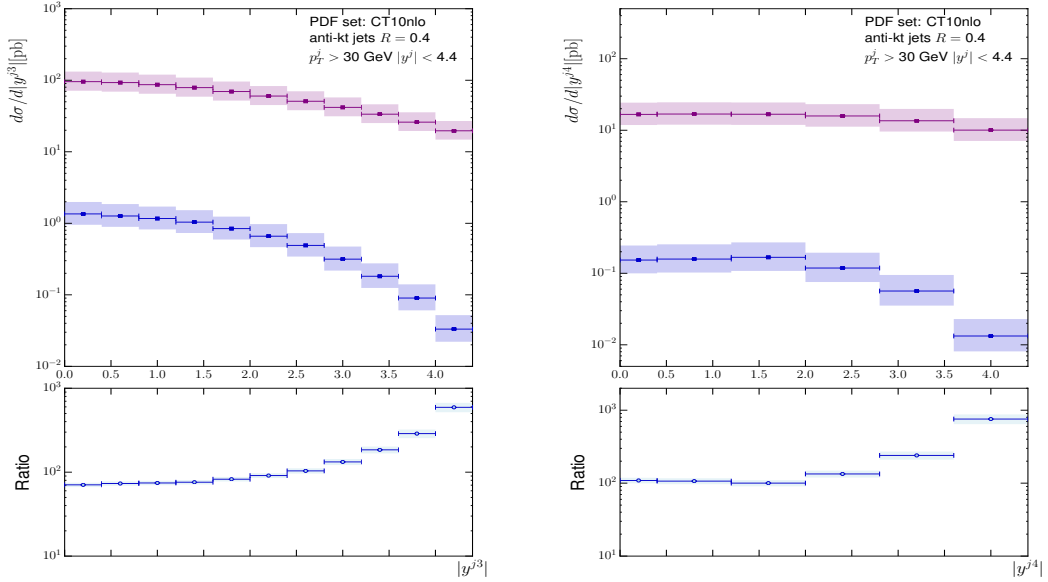


Figure 6.5: The differential cross-section for  $Z/\gamma^*$  plus inclusive dijets as a function of the transverse momentum of the first, second and third leading jets in  $p_T$  shown in fig. (6.5a), (6.5b) and (6.5c) respectively and for centre-of-mass energies of 7TeV (blue) and 100TeV (pink).



(a)



(b)

(c)

Figure 6.6: The differential cross-section for  $Z/\gamma^*$  plus inclusive dijets as a function of the absolute value of the rapidity of the first, second and third leading jets in rapidity shown in fig. (6.6a), (6.6b) and (6.6c) respectively and for centre-of-mass energies of 7TeV (blue) and 100TeV (pink).



## **Chapter 7**

# **Conclusions and Outlook**

Resummation is important.



# Bibliography

- [1] AAD, G., ET AL. Measurement of the production cross section of jets in association with a Z boson in pp collisions at  $\sqrt{s} = 7$  TeV with the ATLAS detector. *JHEP* **1307** (2013), 032.
- [2] AAD, G., ET AL. Measurements of jet vetoes and azimuthal decorrelations in dijet events produced in  $pp$  collisions at  $\sqrt{s} = 7$  TeV using the ATLAS detector. *Eur. Phys. J. C* **74**, 11 (2014), 3117.
- [3] AAD, G., ET AL. Measurements of the W production cross sections in association with jets with the ATLAS detector. *Eur. Phys. J. C* **75**, 2 (2015), 82.
- [4] AAD, G., ET AL. Search for high-mass diboson resonances with boson-tagged jets in proton-proton collisions at  $\sqrt{s} = 8$  TeV with the ATLAS detector. *JHEP* **12** (2015), 055.
- [5] ABAZOV, V. M., ET AL. Studies of W boson plus jets production in  $p\bar{p}$  collisions at  $\sqrt{s} = 1.96$  TeV. *Phys. Rev. D* **88**, 9 (2013), 092001.
- [6] ABRAMOWICZ, H., ET AL. Physics at the CLIC e+e- Linear Collider – Input to the Snowmass process 2013. In *Community Summer Study 2013: Snowmass on the Mississippi (CSS2013) Minneapolis, MN, USA, July 29-August 6, 2013* (2013).
- [7] ALIOLI, S., NASON, P., OLEARI, C., AND RE, E. Vector boson plus one jet production in POWHEG. *JHEP* **01** (2011), 095.
- [8] ALWALL, J., ET AL. Comparative study of various algorithms for the merging of parton showers and matrix elements in hadronic collisions. *Eur. Phys. J. C* **53** (2008), 473–500.
- [9] ALWALL, J., FREDERIX, R., FRIXIONE, S., HIRSCHI, V., MALTONI, F., MATTELAER, O., SHAO, H. S., STELZER, T., TORIELLI, P., AND ZARO, M. The automated computation of tree-level and next-to-leading order differential cross sections, and their matching to parton shower simulations. *JHEP* **07** (2014), 079.
- [10] ALWALL, J., HERQUET, M., MALTONI, F., MATTELAER, O., AND STELZER, T. MadGraph 5 : Going Beyond. *JHEP* **06** (2011), 128.
- [11] ANDERSEN, J. A. Qcd at high energy. <https://conference.ippp.dur.ac.uk/event/514/contribution/6/material/slides/0.pdf>, 2016. [Online; accessed 10-03-2016].
- [12] ANDERSEN, J. R., DEL DUCA, V., AND WHITE, C. D. Higgs Boson Production in Association with Multiple Hard Jets. *JHEP* **0902** (2009), 015.
- [13] ANDERSEN, J. R., HAPOLA, T., AND SMILLIE, J. M. W Plus Multiple Jets at the LHC with High Energy Jets. *JHEP* **1209** (2012), 047.
- [14] ANDERSEN, J. R., LONNBLAD, L., AND SMILLIE, J. M. A Parton Shower for High Energy Jets. *JHEP* **07** (2011), 110.

## BIBLIOGRAPHY

---

- [15] ANDERSEN, J. R., AND SMILLIE, J. M. Constructing All-Order Corrections to Multi-Jet Rates. *JHEP* **1001** (2010), 039.
- [16] ANDERSEN, J. R., AND SMILLIE, J. M. The Factorisation of the t-channel Pole in Quark-Gluon Scattering. *Phys. Rev. D* **81** (2010), 114021.
- [17] ANDERSEN, J. R., AND SMILLIE, J. M. Multiple Jets at the LHC with High Energy Jets. *JHEP* **1106** (2011), 010.
- [18] ANDERSEN, J. R., AND WHITE, C. D. A New Framework for Multijet Predictions and its application to Higgs Boson production at the LHC. *Phys. Rev. D* **78** (2008), 051501.
- [19] ANDERSSON, B., MOHANTY, S., AND SODERBERG, F. Recent developments in the Lund model. In *36th Annual Winter School on Nuclear and Particle Physics (PINP 2002) and 8th St. Petersburg School on Theoretical Physics St. Petersburg, Russia, February 25-March 3, 2002* (2002).
- [20] B. L. IOFFE, V. S. FADIN, L. N. L. *Quantum Chromodynamics: Perturbative and Nonperturbative Aspects*. Cambridge University Press.
- [21] BALITSKY, I., AND LIPATOV, L. The Pomeranchuk Singularity in Quantum Chromodynamics. *Sov.J.Nucl.Phys.* **28** (1978), 822–829.
- [22] BERGER, C. F., BERN, Z., DIXON, L. J., FEBRES CORDERO, F., FORDE, D., GLEISBERG, T., ITA, H., KOSOWER, D. A., AND MAITRE, D. Next-to-Leading Order QCD Predictions for  $Z, \gamma^* + 3$ -Jet Distributions at the Tevatron. *Phys. Rev. D* **82** (2010), 074002.
- [23] BERNINGER, J., ET AL. Review of Particle Physics (RPP). *Phys. Rev. D* **86** (2012), 010001.
- [24] BERN, Z., OZEREN, K., DIXON, L. J., HOECHE, S., FEBRES CORDERO, F., ITA, H., KOSOWER, D., AND MAITRE, D. High multiplicity processes at NLO with BlackHat and Sherpa. *PoS LL2012* (2012), 018.
- [25] BLECHMAN, A. E. Spin correlations in top production and decay  $e^+e^-$  colliders, 2001.
- [26] BRAU, J., OKADA, Y., WALKER, N., DABROWSKI, W., GAJEWSKI, J., IDZIK, M., KISIELEWSKA, D., KULIS, S., SUSZYCKI, L., SWIENTEK, K., ET AL. ILC Reference Design Report: ILC Global Design Effort and World Wide Study.
- [27] BUTTERWORTH, J. M., DAVISON, A. R., RUBIN, M., AND SALAM, G. P. Jet substructure as a new Higgs search channel at the LHC. *Phys. Rev. Lett.* **100** (2008), 242001.
- [28] CACCIARI, M., DREYER, F. A., KARLBERG, A., SALAM, G. P., AND ZANDERIGHI, G. Fully Differential Vector-Boson-Fusion Higgs Production at Next-to-Next-to-Leading Order. *Phys. Rev. Lett.* **115**, 8 (2015), 082002.
- [29] CACCIARI, M., SALAM, G. P., AND SOYEZ, G. The Anti-k(t) jet clustering algorithm. *JHEP* **0804** (2008), 063.
- [30] CATANI, S., AND GRAZZINI, M. HNNLO: A Monte Carlo program to compute Higgs boson production at hadron colliders. *PoS RADCOR2007* (2007), 046.
- [31] CHATRCHYAN, S., ET AL. Measurement of the ratio of the inclusive 3-jet cross section to the inclusive 2-jet cross section in pp collisions at  $\sqrt{s} = 7$  TeV and first determination of the strong coupling constant in the TeV range. *Eur. Phys. J. C* **73**, 10 (2013), 2604.
- [32] CORCELLA, G., KNOWLES, I. G., MARCHESEINI, G., MORETTI, S., ODAGIRI, K., RICHARDSON, P., SEYMOUR, M. H., AND WEBBER, B. R. HERWIG 6: An Event generator for hadron emission reactions with interfering gluons (including supersymmetric processes). *JHEP* **01** (2001), 010.

- [33] DEL DUCA, V. An introduction to the perturbative QCD pomeron and to jet physics at large rapidities, hep-ph/9503226.
- [34] DIXON, L. J. Calculating scattering amplitudes efficiently. In *QCD and beyond. Proceedings, Theoretical Advanced Study Institute in Elementary Particle Physics, TASI-95, Boulder, USA, June 4-30, 1995* (1996).
- [35] DUCLOUE, B., SZYMANOWSKI, L., AND WALLON, S. Mueller-Navelet jets at LHC: the first complete NLL BFKL study. *PoS QNP2012* (2012), 165.
- [36] ELVANG, H., AND TIN HUANG, Y. *Frontmatter*. Cambridge University Press, 2015. Cambridge Books Online.
- [37] FIELD, R. *Applications of Perturbative Quantum Chromodynamics*. Addison Wesley Longman Publishing Co., 1989.
- [38] FORSHAW, J. R., AND ROSS, D. A. *Quantum Chromodynamics and the Pomeron*. Cambridge University Press, 1997. Cambridge Books Online.
- [39] FREDERIX, R., FRIXIONE, S., PAPAEFSTATHIOU, A., PRESTEL, S., AND TORRIELLI, P. A study of multi-jet production in association with an electroweak vector boson.
- [40] FRIXIONE, S., NASON, P., AND OLEARI, C. Matching NLO QCD computations with Parton Shower simulations: the POWHEG method. *JHEP 11* (2007), 070.
- [41] FRIXIONE, S., STOECKLI, F., TORRIELLI, P., WEBBER, B. R., AND WHITE, C. D. The MCaNLO 4.0 Event Generator.
- [42] FRIXIONE, S., AND WEBBER, B. R. Matching NLO QCD computations and parton shower simulations. *JHEP 06* (2002), 029.
- [43] FROLOV, S., AND SLAVNOV, A. An invariant regularization of the standard model. *Physics Letters B 309*, 3 (1993), 344 – 350.
- [44] GEHRMANN, T., GRAZZINI, M., KALLWEIT, S., MAIERHFER, P., VON MANTEUFFEL, A., POZZORINI, S., RATHLEV, D., AND TANCREDI, L.  $W^+W^-$  Production at Hadron Colliders in Next to Next to Leading Order QCD. *Phys. Rev. Lett. 113*, 21 (2014), 212001.
- [45] GLEISBERG, T., HOECHE, S., KRAUSS, F., SCHONHERR, M., SCHUMANN, S., SIEGERT, F., AND WINTER, J. Event generation with SHERPA 1.1. *JHEP 02* (2009), 007.
- [46] GRAZZINI, M., KALLWEIT, S., AND RATHLEV, D. W and Z production at the LHC in NNLO QCD. *JHEP 07* (2015), 085.
- [47] GRIFFITHS, D. *Introduction to Elementary Particles*. Physics Textbook. Wiley, 2008.
- [48] HOECHE, S., KRAUSS, F., SCHONHERR, M., AND SIEGERT, F. QCD matrix elements + parton showers: The NLO case. *JHEP 04* (2013), 027.
- [49] HCHE, S., KUTTIMALAI, S., SCHUMANN, S., AND SIEGERT, F. Beyond Standard Model calculations with Sherpa. *Eur. Phys. J. C75*, 3 (2015), 135.
- [50] ITA, H., BERN, Z., DIXON, L. J., FEBRES CORDERO, F., KOSOWER, D. A., AND MAITRE, D. Precise Predictions for Z + 4 Jets at Hadron Colliders. *Phys. Rev. D85* (2012), 031501.
- [51] J. ANDERSEN, J. MEDLEY, J. Z/gamma\* plus Multiple Hard Jets in High Energy Collisions.
- [52] KHACHATRYAN, V., ET AL. Measurements of jet multiplicity and differential production cross sections of Z+ jets events in proton-proton collisions at  $\sqrt{s} = 7$  TeV. *Phys. Rev. D91*, 5 (2015), 052008.

## BIBLIOGRAPHY

---

- [53] KUIPERS, J., UEDA, T., VERMASEREN, J. A. M., AND VOLINGA, J. Form version 4.0. *CoRR abs/1203.6543* (2012).
- [54] KURAEV, E. A., LIPATOV, L. N., AND FADIN, V. S. Multi - Reggeon processes in the Yang-Mills theory. *Sov. Phys. JETP* **44** (1976), 443–450.
- [55] LONNBLAD, L. ARIADNE version 4: A Program for simulation of QCD cascades implementing the color dipole model. *Comput. Phys. Commun.* **71** (1992), 15–31.
- [56] MANGANO, M. L., MORETTI, M., PICCININI, F., PITTAU, R., AND POLOSA, A. D. ALPGEN, a generator for hard multiparton processes in hadronic collisions. *JHEP* **07** (2003), 001.
- [57] MUTA, T. *Foundations Of Quantum Chromodynamics: An Introduction to Perturbative Methods in Gauge Theories*. World Scientific lecture notes in physics. World Scientific Publishing Company Incorporated, 2010.
- [58] NASON, P. A new method for combining nlo qcd with shower monte carlo algorithms. *Journal of High Energy Physics* **2004**, 11 (2004), 040.
- [59] PAULI, W., AND VILLARS, F. On the invariant regularization in relativistic quantum theory. *Rev. Mod. Phys.* **21** (Jul 1949), 434–444.
- [60] R. K. ELLIS, W. J. STERLING, B. R. W. *QCD and Collider Physics*. Cambridge Monographs on Particle Physics, 2010.
- [61] SALAM, G. P., AND SOYEZ, G. A Practical Seedless Infrared-Safe Cone jet algorithm. *JHEP* **05** (2007), 086.
- [62] SJOSTRAND, T., EDEN, P., FRIBERG, C., LONNBLAD, L., MIU, G., MRENNA, S., AND NORRBIN, E. High-energy physics event generation with PYTHIA 6.1. *Comput. Phys. Commun.* **135** (2001), 238–259.
- [63] SJOSTRAND, T., MRENNA, S., AND SKANDS, P. Z. A Brief Introduction to PYTHIA 8.1. *Comput. Phys. Commun.* **178** (2008), 852–867.
- [64] STERMAN, G. F. Partons, factorization and resummation, TASI 95. In *QCD and beyond. Proceedings, Theoretical Advanced Study Institute in Elementary Particle Physics, TASI-95, Boulder, USA, June 4-30, 1995* (1995).
- [65] VERA, A. S. High energy scattering in quantum chromodynamics, [www.hep.man.ac.uk/u/forshaw/sabio.ps.gz](http://www.hep.man.ac.uk/u/forshaw/sabio.ps.gz), 2000.

# Publications

Author Name(s). Title of publication. In *Where Published*, Year.

Author Name(s). Title of publication. In *Where Published*, Year.